MRI Visualization and Mathematical Modeling of Local Drug Delivery

by

Morgan Giers

A Dissertation Presented in Partial Fulfillment
of the Requirements for the Degree
Doctor of Philosophy

Approved March 2013 by the
Graduate Supervisory Committee:

Michael Caplan, Chair
Stephen Massia
David Frakes
Alex McLaren
Brent Vernon

ARIZONA STATE UNIVERSITY

May 2013

ABSTRACT

Controlled release formulations for local, *in vivo* drug delivery are of growing interest to device manufacturers, research scientists, and clinicians; however, most research characterizing controlled release formulations occurs *in vitro* because the spatial and temporal distribution of drug delivery is difficult to measure *in vivo*. In this work, *in vivo* magnetic resonance imaging (MRI) of local drug delivery is performed to visualize and quantify the time resolved distribution of MRI contrast agents. I find it is possible to visualize contrast agent distributions in near real time from local delivery vehicles using MRI. Three dimensional T_1 maps are processed to produce *in vivo* concentration maps of contrast agent for individual animal models. The method for obtaining concentration maps is analyzed to estimate errors introduced at various steps in the process. The method is used to evaluate different controlled release vehicles, vehicle placement, and type of surgical wound in rabbits as a model for antimicrobial delivery to orthopaedic infection sites. I are able to see differences between all these factors; however, all images show that contrast agent remains fairly local to the wound site and do not distribute to tissues far from the implant in therapeutic concentrations. I also produce a mathematical model that investigates important mechanisms in the transport of antimicrobials in a wound environment. It is determined from both the images and the mathematical model that antimicrobial distribution in an orthopaedic wounds is dependent on both diffusive and convective mechanisms. Furthermore, I began development of MRI visible therapeutic agents to examine active drug distributions. I hypothesize that this work can be developed into a non-invasive, patient specific, clinical tool to evaluate the success of interventional procedures using local drug delivery vehicles.

DEDICATION

To my husband, Jason, who is my partner in all things, my greatest supporter and truest friend. Thank you for pretending to listen and for the late night coffee.

To my parents, who always encouraged me to reach for success in whatever I did.

ACKNOWLEDGMENTS

This work was a large interdisciplinary team undertaking and there are many people whose help was instrumental in its success. First, I would like to thank my advisor, Michael Caplan, for his dedication. His commitment as an educator and mentor is truly inspiring and his guidance has helped me achieve success. I would like to recognize the partnership and leadership of Dr. Alex McLaren and Ryan McLemore, which made this project possible. I acknowledge David Frakes and Jonathan Plasencia, whose input were influential in giving the image processing techniques a new level of professionalism. I am also grateful to Gregory Turner and Qingwei Liu, who were essential in the development of MRI protocols and acquiring images, and where considerate in answering all my questions through this learning process. Vikram Kodibagkar provided a critical review of the MRI procedure that certified I were on the right track. I am indebted to all the orthopaedic residents I have worked with: Chris Estes, Jeff Abilgaard, Ryan Miller, Ken Schmidt, Jason Patterson, Robert Waldrop, William Wood, Sam Harmsen, Ryan Odgers, and James Fraser. I am thankful for the undergraduate students Ethan Province, Chiao May Lee, Adam Roussas, Matt McDermand, Amanda Grzybowski, and Emerson Tucker who were always enthusiastic and patient.

I would like to thank all the other professionals who have supported my work, especially Kate Cronk and Dr. Nicholas Theodore. I am also appreciative of all the people who have offered me their advise, including Veronica Clavijo Jordan and Derek Overstreet.

I am extremely grateful to those who provided financial support to me or the project. Myself and the project were supported by the Arizona Biomedical Research Commission Grant #1116. My learning was supported by Ira A. Fulton Schools of Engineering, the School of Biological and Health Systems Engineering, The Balster-Evani Family Fund through Achievement Rewards for College Scientists, and the Graduate and Professional Student Association travel awards. Other critical participants in this project received funding from Banner Good Samaritan Medical Center and the Herbert Louis fund at Orthopaedic Research and Education Foundation.

TABLE OF CONTENTS

CHAPTER Page

1. INTRODUCTION 1

1.1 Introduction to Local Drug Delivery 1

1.2 Orthopaedic Infection 1

1.2.1 Scope of the Problem 2

1.2.2 Biofilm Development and Proliferation 2

1.2.3 Surgical Treatment of Orthopaedic Infection 4

1.2.4 *In Vitro* Characterization of Orthopaedic Bone Cement 4

1.2.5 *In Vivo* Characterization of Orthopaedic Bone Cement 1

1.3 MRI Visualization of Contrast Agents 7

1.2.1 Basic MRI Physics and How Contrast Agents Work 8

1.2.2 Research of MRI Parameters Effecting Calculation of Contrast Agent Concentration 9

1.2.3 Previous Experiments Calculating Concentration of Contrast Agents in MRI 10

1.4 Transport of Drugs Physiological Systems 11

1.5 Clinical Importance 13

2. Visualization of Local drug delivery 15

2.1 Introduction 15

2.2 Methods 16

2.2.1 Delivery Vehicle Fabrication 19

2.2.2 Surgical Procedure 20

CHAPTER Page

2.2.3 Image Acquisition 21

2.2.4 Euthanasia.....22

2.2.5 Interobserver Correlation 23

2.2.6 Statistics.....23

2.3 Results 24

2.3.1 Is *In Vivo* Distribution of Locally Delivered Gd-DTPA Visible on MRI? 24

2.3.2 Is *In Vivo* Distribution of locally Delivered Gd-DTPA Affected by the Anatomic Delivery Site?.....24

2.2.4 Is *In Vivo* Distribution of Locally Delivered Gd-DTPA Affected by the *In Vitro* Release Rate from the Delivery Vehicle?.25

2.4 Discussion 27

2.5 Conclusions.....30

3. SPATIOTEMPORTAL QUANTIFICATION OF LOCAL DRUG DELIVERY USING MRI..... 31

3.1 Introduction.....31

3.2 Methods.....34

3.2.1 Delivery Vehicle Fabrication.....34

3.2.2 Surgical Procedure 35

3.2.3 Image Acquisition 36

3.2.4 Image Processing.....37

3.2.5 Image Analysis 42

CHAPTER Page

3.2.6 Statistics 43

3.3 Results and Discussion 43

3.3.1 How Good are T_1 Maps? 43

2.3.2 What does Filtering do? 44

3.2.3 How Consistent is Segmentation? 45

3.2.4 How Reliable are the Concentration Values? 45

3.2.5 How does the Isotropic $T_{1,0}$ Method Compare to Other Methods? 52

3.2.6 What Practical Information can this Method Provide? 55

3.5 Conclusions 56

4. DISTRIBUTION PATTERNS OF LOCAL DRUG DELIVERY IN ORTHOPAEDIC WOUNDS USING MRI 58

4.1 Introduction 58

4.2 Methods 61

4.2.1 Delivery Vehicle Fabrication 61

4.2.2 Surgical Procedure 62

4.2.3 Image Acquisition 63

4.2.4 Euthanasia 63

4.2.5 Image Processing 63

4.2.6 Statistics 64

4.3 Results 65

4.3.1 Can It be Seen? 65

CHAPTER Page

4.3.2 Can Concentration be Measured? 66

4.2.3 Does Surgical Wound Environment Affect the Distribution of Locally Delivered Gd-DTPA (Antimicrobial Surrogate)? 66

4.4 Discussion 73

4.5 Conclusions 75

5. DEVELOPMENT AND CHARACTERIZATION OF MRI VISIBLE ANTIMICROBIALS 76

5.1 Introduction 76

5.2 Methods 77

5.2.1 Conjugate Preparation 77

5.2.2 High Pressure Liquid Chromatography 78

5.2.3 Mass Spectrometry 78

5.2.4 Xylenol Orange Assay 79

5.3 Results 79

5.3.1 Was the Conjugation of Antimicrobial to DOTA Successful? 79

5.3.2 Was the Chelation of Gadolinium Successful? 84

5.4 Discussion 85

5.5 Conclusions 86

6. MATHEMATICAL MODELING OF LOCAL DRUG DELIVERY IN ORTHOPAEDIC WOUNDS 87

6.1 Introduction 87

6.2 Methods and Model Development 89

CHAPTER Page

6.2.1 Governing Equation 90

6.2.2 Drug Diffusion (ADC) 91

6.2.3 Capillaries and Lymph 92

6.2.4 Flow from Edema 93

6.2.5 Peclet Number 93

6.2.6 Boundary Conditions 94

6.3 Results 94

6.3.1 Does the ADC Map Matter? 94

6.3.2 Is Convection or Diffusion Dominant? 95

6.2.3 What do Different Materials Look Like? 104

6.2.4 What do Different Wound Types Look Like? 105

6.4 Discussion 108

6.5 Conclusions 110

7. CONCLUSIONS AND FUTURE WORK 111

7.1 Spatiotemporal Distribution of Contrast Agents Delivered to Orthopaedic Wounds 111

7.2 Quantification of Differences Between Active Therapeutic Agent and Inert Molecule Distributions 113

7.3 Imaging an Active Antimicrobial Agent 118

7.4 Imaging Drug Distribution in the Presence of an Active Infection 119

7.5 Mathematical Modeling of Local Drug Delivery Vehicles 120

7.6 Conclusion 1 21

Page

REFERENCES 123

APPENDIX

A MATLAB CODE 137

B PROTOCOL FOR IMAGE PROCESSING USING MATLAB AND MIMICS 162

Chapter 1: INTRODUCTION

1.1 Introduction to Local Drug Delivery

Local drug delivery is increasing in popularity in both research and industry. Local drug delivery vehicles can create a high concentration of drug in a specific region, while maintaining much lower levels of therapeutic in other areas of the body [1,2]. This can focus treatment to an affected region, which is important in a variety of applications such as tumor treatment [3], pain management [4,5], tissue engineering [6], and infection management [7]. Local drug delivery vehicles come in a multitude of formulations and can be tailored for a specific function. Broadly local drug delivery vehicles can be categorized by their properties such as biodegradable or bioinert, fast or slow releasing, and bulk or surface releasing. Fast releasing materials include bioresorbable collagen and fibrin gels, which can release their entire load in 24 hours [8]. The slowest releasing vehicles are not penetrated by water, limiting drug release to pores in the vehicle. Pores can easily be created by porogens, which remain a solid during material synthesis, but then dissolve in the presence of certain solvents, leaving empty space. Polymethyl methacrylate (PMMA) is commonly used as a delivery vehicle for antimicrobials in orthopaedics and acts under such mechanisms. In antimicrobial loaded PMMA the pores are created by the antimicrobials themselves so release is a function of the amount of drug loaded [9]. When low amounts of antimicrobial are loaded in PMMA release might be as slow as 3-5% over 1 month[10].

1.2 Orthopaedic Infection

1.2.1 Scope of the Problem

Orthopaedic infections are infections of orthopaedic implants such as artificial joints and fracture fixation devices. These infections occur in about 1-2% of primary arthroplasties[11,12]. The rate is higher in traumatic wounds, such as in traumatic wounds of the spine where the rate of infection is 9.4% [13]. Once established these infections are difficult to cure with 10-23% of patients experiencing recurring infection [14,15]. There are approximately 112,000 cases of orthopaedic infections annually in the US [16]. Infections are devastating to the patient physically often requiring the patient to rely heavily on the assistance of caregivers for an extended period of time. Not only are infections physically painful, but they place a significant financial burden on patients as well. Each case of infection treatment costs $15,000 to $233,000 [16,17]. Darouiche *et al.* estimated in 2004 that 1.8 billion dollars were spent annually on orthopaedic infection in the US [16]. The annual cost is likely larger currently as more patients receive arthroplasties every year. The number of arthorplasties performed annually is projected to increase by several fold over the next 18 years [18].

1.2.2 Biofilm Development and Proliferation

Orthopedic infections are complex problems because they are the result of biofilm forming microbes, such as *Staphylococcus aureus*. The microbes attach to the surface of the implant and through quorum sensing begin to establish a communal microenvironment, biofilm, when enough bacteria are present [19]. Biofilms protect against the host response system by enveloping neutrophils with planktonic bacteria ejected

from the biofilm [20] and deactivating antimicrobial peptides [21]. Furthermore, biofilm residing microbes are much less susceptible to antimicrobials because of multiple mechanisms [22]. First, the biofilms cause a barrier to antimicrobial transport in some cases. Microbes, like positively charged gentamicin, can become bound to the negatively charged polysaccharide matrix, limiting their ability to penetrate thick biofilm [22-24]. In addition to the biofilm potentially limiting the transport of antimicrobials to the bacteria, the microbes themselves are resistant to antimicrobials [25,26]. The resistance, however, is not the product of traditional genetic mutations adopted by the microbes over time because bacteria from a dispersed biofilm recover their antimicrobial sensitivity quickly [22,27,28]. There are several possible methods that could cause bacteria to be less susceptible to microbes because of the microenvironment. The microenvironment in biofilm is very heterogeneous, supporting multiple variations of the bacteria within the same colony[19]. For instance, areas where there are very low transport of nutrients could lead to deregulation of the metabolisms of bacteria in those areas. These bacteria would then be less susceptible to antimicrobials because they are in a sessile state. Other factors, such as pH and osmotic pressure could play a role in bacterial differentiation and hence antimicrobial susceptibility as well. These factors lead to antimicrobial sensitivities 100-1000 times less in biofilm than in planktonic bacteria [25,26]. When insufficient concentrations of antimicrobial are delivered to planktonic bacteria they can even propagate the development of biofilms [29,30]. Since antimicrobial action is time and concentration dependent, high concentrations need to persist to be effective. For instance, biofilm methacillin-resistant *Staphylococcus aureus* takes more than 5 days of exposure to 2 mg/mL vancomycin to be eradicated [29]. The levels of antimicrobial required to kill

biofilm residing microbes cannot be achieved systemically without causing toxic effects. Local drug delivery is required to effectively treat biofilm infections such as those present in orthopaedic infections.

1.2.3 Surgical Treatment of Orthopaedic Infection

Most orthopaedic infections are treated by a two stage surgical revision [15,31-35]. In the first stage the biofilm and implant are removed and the surrounding tissue is debrided. The space is then filled with antimicrobial loaded bone cement. The bone cement is left for several weeks to treat any biofilm debris remaining in the tissue and planktonic bacteria in the muscle[15,33]. The implant cannot be replaced at this time as any bacteria still in the patient could reattach to that surface and cause a recurrent infection [36]. After the several week delay the second stage can be performed where the ABLC is removed and the implant is replaced. Surgeons aim to cover the entirety of the wound surface as well as penetrate into the surrounding muscle with antimicrobial in case the debridement wasn't complete or there were planktonic bacteria.

1.2.4 *In Vitro* Characterization of Orthopaedic Bone Cement

Antimicrobial loaded bone cement can be bought with low doses of antimicrobial from several manufacturers, including Simplex® (Stryker, Kalamazoo, MI), but many surgeons mix antimicrobials into cement at the time of surgery. Bone cement is bought as a package of polymethyl methacrylate (PMMA) powder that contains benzoyl peroxide and methyl methacrylate (MMA) liquid with N,N-dimethyl-p-toluidine [37]. When the MMA liquid is added to the powder the N,N-dimethyl-p-toluidine reacts with benzoyl

peroxide to create free radicals and initiate a free radical polymerization [37,38]. The MMA polymerizes with the PMMA powder and after several minutes forms a hard solid [37]. Before the mixture hardens a surgeon can form the dough into any shape or can use the dough to cement an implant in place. Antimicrobials can be added to the powder before the addition of the monomer. The antimicrobial powders do not dissolve in the monomer so after the cement is dry there is a solid matrix of PMMA with antimicrobial powder imbedded throughout. When aqueous fluid, such as that present in the body, contacts the antimicrobial, the powder will dissolve and the antimicrobial will elute from the cement leaving a pore in the cement where the powder used to be. Aqueous fluid can then invade that space and dissolve the next antimicrobial powder it contacts. The process continues until the fluid has penetrated all interconnected pores. There are many methods to modify the cement formulation to obtain high antimicrobial release, such as the inclusion of other inert porogen or fillers to increase the pore interconnectivity [9]. There is much data for *in vitro* research on antimicrobial loaded bone cement of varying compositions [9,39-50]. For instance, Klekamp *et. al.* studied the elution of several antimicrobials, vancomycin and tobramycin, from two different bone cements and looked at the compressive strength and fatigue life of the cements [47]. They found that antimicrobials maintain activity after elution from cement, both antimicrobials did elute, and although low doses of antimicrobial do not significantly affect compressive strength, it does shorten the fatigue life of the cement [47]. Lewis *et. al.* developed a method to determine the optimum mass percent of antibiotics to load in weight baring cement as a function of antimicrobial release and compressive strength [48]. Rasyid *et. al* studied adjusting the amount of MMA monomer to use in the powder to increase porosity and antimicrobial elution from

cements. Other groups have looked at the addition of various fillers or composite materials such as Schnieders *et al.* who used a poly (lactic-co-glycolic acid)/PMMA composite to increase antimicrobial release. McLaren *et al.* studied the homogeneity of hand mixed bone cement compared to commercial formulations and found there is no difference between the two. There are over a thousand other studies on various aspects of antimicrobial loaded bone cement since its invention in 1970[50]. *In vitro* experiments studying elution of antimicrobials from cement are usually performed in near infinite sink condition, where specimens with simple geometries are kept in relatively large volumes of well mixed aqueous fluid [46,47]. This experimental setup allows for calculation of various transport properties of the material such as flux, which is surface area and volume dependent. By performing these simple experiments researchers can easily compare delivery vehicles of various compositions. Furthermore, by using infinite sink conditions the greatest possible release can be calculated so the safety of the vehicle can be evaluated. These experiments, however, cannot describe how drugs will distribute in complex *in vivo* tissue.

For instance, bone is a barrier to antimicrobial transport. The effective diffusion coefficient water in bone ($D_{eff}=7.8\times10^{-11}$ m^2/s) [51] is much lower than in muscle ($D=1.38\times10^{-9}$ m^2/s) [52]. When antimicrobial loaded cement is in bone there will be an accumulation of antimicrobial between the bone and the cement. The accumulation will decrease the concentration gradient from between the cement and its environment, the driving factor for antimicrobial delivery, and delivery from the cement will decrease. Therefore, *in vitro* testing cannot predict *in vivo* concentration over time and location.

1.2.5 *In Vivo* Characterization of Orthopaedic Bone Cement

To gather information on the *in vivo* behavior there have been some research collecting fluid samples and biopsies [1,2,53-57]. In general concentrations are over 100 times higher near the implant than in the blood [1,53]. Biopsies from Adams *et* al showed effective concentrations were delivered up to 28 days after the surgery [2]. From that and other studies it is confirmed that therapeutic doses can be achieved at a location *in* vivo [1,2,53-56], however the biopsy based technique is limited in spatial resolution to the number of samples obtained. Furthermore, the biopsy method is time consuming. Several groups have studied *in vivo* patient outcomes to determine treatment efficacy [7,14,31,58-61]. Dunbar *et al* looked at the patient outcomes using antimicrobial loaded bone cement versus using systemic antimicrobials only [7]. Cierney *et al.* looked at how patient health effected their prognosis [58]. Walenkamp *et al* looked at the long term prognosis of patients receiving antimicrobial bone cement and assessed its relationship to healing [59]. Other groups have assessed safety of different amounts of loading [62]. These methods can help develop better procedures, but they cannot determine reasons for failure. Furthermore, these methods require a large number of replicates a long experimental time to be meaningful, so it is unknown if the method is effective until after several years.

1.3 MRI Visualization of Contrast Agents

In this work, to obtain the comprehensive spatial distribution of drugs eluting from local drug delivery vehicles in orthopaedic surgical wounds the distribution of contrast agents is imaged using magnetic resonance imaging (MRI).

1.3.1 Basic MRI Physics and How Contrast Agents Work

MRI visualizes the motion of water molecules. When protons are placed in a magnetic field their axis tend to align with the direction of the field [63]. Not only do they align with the field, they also process about the axis of the magnetic field at a rate that is proportional to the magnetic field strength, called the Larmor frequency [63]. A radio frequency (RF) electromagnetic pulse can be applied at the Larmor frequency, the resonant frequency of the protons, and cause the magnetic moments of the protons to align so they process together. The net magnetization of a group of protons causes an electromagnetic signal that can be detected by a transceiver coil [64]. If the RF pulse is applied at an angle from the main magnetic field it can cause the axis of the protons to tip toward the RF pulse while the pulse is being applied. The angle of the RF pulse is referred to as flip angle [64]. After the RF pulse is finished the magnetic moments of the processing proton spins begin to misalign or dephase. The time it takes for the magnetic moments to dephase is commonly referred to as spin-spin or transverse relaxation time and is referred to as T_2 time [63,65]. While the spins are dephasing the tilt of the axis are also changing to return back to the starting state of alignment with the main magnetic field. The time it takes for the axis to return to their starting state is referred to as spin-lattice or longitudinal relaxation time. The longitudinal relaxation time is referred to as the T_1 time [63,65].

The magnetic signal of the protons is detected by a transceiver coil in the transverse plane. The transceiver acquires signal at a certain time, called the echo time (TE), after the RF pulse was emitted . Multiple measurements must be made on a single slice to obtain all the spatial information. The time between successive measurements is

called the repetition time (TR) [64]. Different MRI sequences incorporate different flip angles, TR, and TE times to emphasis different relativities. T_1 weighted images are obtained using short TE and TR times.

MRI contrast agents exhibit paramagnetic or ferromagnetic properties, meaning they are able to effect the magnetic field surrounding them. When water molecules are near the contrast agents their spins are affected by the magnetic field of the molecule. When an RF pulse is applied molecules in contact with the contrast agent return to equilibrium faster than they would without the presence of that magnetic field. This decreases the observed T_1 and T_2 relaxation rates. Some of the molecules used as contrast agents, such as gadolinium, are toxic in their ionic forms requiring them to be bound by a chelator to reduce or eliminate the toxicity [66]. The effect of a contrast agent is dependent on several factors including the number of water molecules it can bind at a time (the hydration number) and the length of time water molecules are bound (the exchange rate) [67]. Contrast agents with high exchange rates and hydration numbers produce a greater effect on the MR signal [67]. The concentration of contrast agent in a certain region is proportional to the decrease in T_1 or T_2 time. The proportionality constant is called the relaxivity constant of the contrast agent.

1.3.2 Research of MRI Parameter Effecting Calculation of Contrast Agent Concentration

There have been many studies that have considered various aspects of the MRI contrast/concentration relationship based on *in vitro* tests. Stanisz *et al.* studied the relationship between contrast relaxivity and macromolecular content, finding that the relaxivity of a contrast agent can vary by over 200% when the macromolecular content in

a fluid is raised from 0 to 40wt% [68]. Noordin and colleagues found the influence of ionic proteins commonly found in synovial fluid on the relaxivity of Gd based contrast agents is minimal at measurable concentrations [69]. Rohrer *et al.* studied the relationship between relaxivity and magnetic field strength an found that the relaxivity of Gd-DTPA changed by 10% between 0.47 and 4.7 T magnets[70]. Fleckenstein *et al*. found that there was as great as 50% variability in normal muscle T_1 values based on the exercise state of the muscle [71]. Prantner shows in an *in vitro* study that without functionalization of MR chelates with transmembrane peptides, little contrast agent is intracellularized in mammalian cells [72]. If contrast agent is not intracellularized the effect of differences in intracellular environment on observed relaxivity is minimized. Donahue *et al.* [73] and Strich *et al.* [74] studied relaxivities of contrast agent in different tissues and found that the relaxation of Gd-DTPA in different tissues was not statistically different.

1.3.3 Previous Experiments Calculating Concentration of Contrast Agent in MRI

Magnetic resonance imaging (MRI) has been used to visualize distribution of drugs delivered locally in several clinically relevant applications. Drug delivery from catheters in convection enhanced delivery procedures for treatment of glioblastomas has been studied by multiple research groups [75-78]. Sarntinoranont and co-workers have studied delivery of gadolinium diethylenetriaminepentaacetic acid (Gd-DTPA) delivery to tumors [79], and they calculate concentration of the Gd-DTPA using a method validated in an agarose phantom [80]. Several other groups have calculated concentrations of contrast agent *in vitro* as well [73,81-84]. However, their methods of quantification are not validated *in vivo* to determine sources of error or to quantify the error likely in their *in vivo*

measurements. Sampson and co-workers also deliver MRI contrast agents to tumors, but no quantification of the agent's concentration is performed [76,77]. Krauze *et al.*[78] and Port *et al.* [85] imaged liposomal Gd-DTPA delivery, but neither quantified concentration. Fritz-Hansen *et al.* calculated bulk concentration of contrast in arterial blood, but was not concerned with spatial distribution [86]. Kim *et al*. quantified the distribution of drugs delivered from an ocular implant using MRI [87]; however, the function used by Kim *et al.* to convert MR intensity to concentration is similar in shape to a parabola and thus results in two valid concentrations for most MR intensity values – one concentration being high and the other being low concentration; thus, the user must infer which concentration is more likely based on proximity to the depot.

1.4 Transport of Drugs in Physiological Systems

The change in drug concentration over time is reliant upon 3 factors: the diffusion of the drug into or out of the system, the amount of drug leaving or entering the system due to bulk fluid flow and the generation or consumption of the drug within the system [88]. The diffusion of a drug is proportional to the concentration gradient. When there is a steep concentration gradient, such as when a drug delivery vehicle is placed in a fluid containing no drug, the diffusion occurs faster than when the concentration gradient is low, such as when the concentration outside of a delivery vehicle is near the concentration inside the delivery vehicle. When concentrations in one area are equal to concentrations in an adjacent area there will be no diffusive exchange of the molecule between those areas. Diffusion is also a function of a physical constant, the diffusion coefficient, that describes the inherent properties of the material a molecule is diffusing

through. In a dense material, such as bone, the diffusion coefficient of a molecule is lower than in a free liquid such as water. Diffusion coefficients are related, among other factors, to the size of the molecule diffusing. Large molecules will diffuse more slowly, have a lower diffusion coefficient, than smaller molecules. I hypothesize that the contrast agent Gd-DTPA is a fairly accurate model for antimicrobials because it has a similar size and hence diffusion coefficient ($D=4.0 \times 10^{-10}$ m^2/s) [89] to the antibiotics Gentamicin ($D= 2.1 \times 10^{-10}$ m^2/s)[23] and Vancomycin ($D= 3.6 \times 10^{-10}$ m^2/s) [90] in water.

Convection is the movement of molecules due to bulk fluid flow. In convection the size of the molecule does not matter in most cases. Small molecules will travel at the same speed as large molecules, unless the space the fluid is flowing through has pores near the size of the larger molecule. Then the large molecule will be hindered by filtration while the small molecule would be unaffected. In this work I will assume the size of all molecules is sufficiently small in comparison to the pores of the material that filtration effects can be ignored. For aqueous fluid the velocity at which fluid flows is proportional to the pressure drop across that length of fluid flow [88,91]. It is also a function of the permeability of the tissue [91,92]. One source and sink of fluid flow in the muscle is from capillaries [93]. When tissue is damaged leukocytes are recruited to the area and the capillaries dilate to facilitate their extravasation, which also allows edematic flow from the leaky capillary [94].

The consumption or generation of a molecule for transportation can occur because of reaction or because of a mechanism that binds or unbinds the molecule, rendering it unavailable to transport. Antimicrobials could be affected by this parameter if they get taken into bacterial cells, get taken into the vascular system, or bind to other molecules.

1.5 Clinical Importance

Orthopedic surgeons use ALBC to treat infection, but there is no standard guidelines for dose [31,95] or cement composition. The lack of standardization could be a result of the methods currently employed to characterize ALBC. Current *in vivo* research methods rely on multiple local biopsies and histology [1,2,53], which are not comprehensive and are time consuming. Achieving concentrations above the minimum inhibitory concentration in one small area being biopsied does not guarantee sufficient concentrations everywhere in the infected region. Furthermore, taking multiple painful biopsies is not practical for human subjects on a patient specific basis.

In this work the spatial distribution of drugs over time was visualized using MRI. The methods presented here give a comprehensive view of the behavior of contrast agents in an orthopaedic wound environment *in vivo*. Information provided by *in vivo* research studies and mathematical model could provide surgeons with general information on ways to improve local delivery depot dose, placement, and composition. Furthermore, this technique could be developed into a clinical tool to evaluate the success of interventional therapy on a patient specific basis. A patient could receive a vehicle containing therapeutic and contrast agent and be imaged within the first 24 hours after surgery to evaluate if there was reasonable coverage of the debrided space. If there is not contrast seen covering the debrided area intervention could be performed immediately. The imaging method could possibly reduce the amount of time for recovery because the patient would not have to show signs of recurrent infection before receiving additional intervention.

In this work a mathematical model of antimicrobial delivery to orthopaedic wounds is also developed. Adjusting parameters in the model could provide a quick, economical, and ethically responsible way to engineer better potential clinical solutions and guide future *in vivo* experiments.

Chapter 2: VISUALIZATION OF LOCAL DRUG DELIVERY USING MRI

2.1 Introduction

The incidence of infection in primary arthroplasties is 1-2% [11] and 10-23% in revision arthroplasties [14,15]. Infections of joint implants cause a financial and physical burden on the patient. Treatment often requires multiple surgeries. A major complicating factor in orthopedic infection is the development of biofilm. The minimum bactericidal concentration (MBC) for bacteria in biofilm is much higher (100-1000x minimum inhibitory concentration) than for planktonic bacteria[26,96]. Antimicrobials of these concentrations cannot be achieved systemically without severe toxicity. Clinically, acrylic bone cement and $CaSO_4$ are commonly used to deliver antimicrobials, although other vehicles, including collagen, have been investigated. These vehicles have a variety of release rates ranging from 100% over 24 hours for collagen [8] to 3-5% over 1 month for low-porosity bone cement [10]. The use of antimicrobial loaded bone cement (ALBC) results in high local concentration of antimicrobials and low systemic levels [1,2]. There is an extensive history of *in vitro* studies of antimicrobial delivery from ABLC [2,7,11,14,15,46,95,97,98]; however, little is known about the concentration and spatial distribution over time *in vivo*. Current *in vivo* methods often involve collection of the fluid surrounding an implant and serum at various times to obtain a time resolved elution curve [1,2]. Sometimes tissue segments near the implant are sampled at conclusion of the experiment to show some spatial distribution of the drug [2]. The major limitation of previous methods is they are time consuming and spatial distribution is limited to the number of biopsies. An ideal method for studying ALBC would give the spatial

distribution of antimicrobial concentrations as a function of time. This information could assist surgeons in optimizing the dose of antimicrobials and porogen in ALBC, mixing methods, surgical placement, and treatment durations, potentially leading to improved efficacy for prophylaxis and treatment of periprosthetic infections.

The most practical method for acquiring information on spatial distribution of antimicrobials as a function of time is through imaging. Drug distribution over time has been studied before using imaging, most prevalently in glioma research. Several groups have studied delivery of contrast agents to the brain [75,76]. The imaging research has led to some successful modeling techniques for optimum catheter placement during neurosurgery [77]. Other groups have shown it possible to determine actual concentrations of contrast agents from MRI images [73,81-84].

This research was conducted as a collaboration between Morgan Giers, Chris Estes, Alex McLaren, Michael Caplan and Ryan McLemore. These data are published in the journal Clinical Orthopaedics and Related Research [99]. Specific contributions of each team member are stated in the corresponding sections in the methods; however it should be additionally noted that all team members participated in analyzing and interpreting the data.

The research questions for this study are: is *in vivo* distribution of locally delivered Gd-DTPA visible on MRI? Is *in vivo* distribution of locally delivered Gd-DTPA affected by the anatomic delivery site? Is *in vivo* distribution of locally delivered Gd-DTPA affected by the *in vitro* release rate from the delivery vehicle?

2.2 Methods

Twenty-four local delivery depots were imaged in nine rabbits using three delivery sites (intraoseous canal, quadriceps, hamstrings). The left legs received an intraoseous rod of a control formulation or loaded with Gd-DTPA in intermediate-porosity or high-porosity (all in triplicate). The right legs received an intramuscular rod of a control formulation or loaded with Gd-DTPA in intermediate-porosity or high-porosity (all in triplicate); six of the nine rabbits also received a collagen injection either with or without Gd-DTPA (each in triplicate). Gd-DTPA distribution was imaged in rabbits after local delivery. Images were assessed for area of contrast distribution as visible on MRI. Images were also analyzed for area during an interobserver reliability study of a subset of images by blinded reviewers (Fig 2.1).

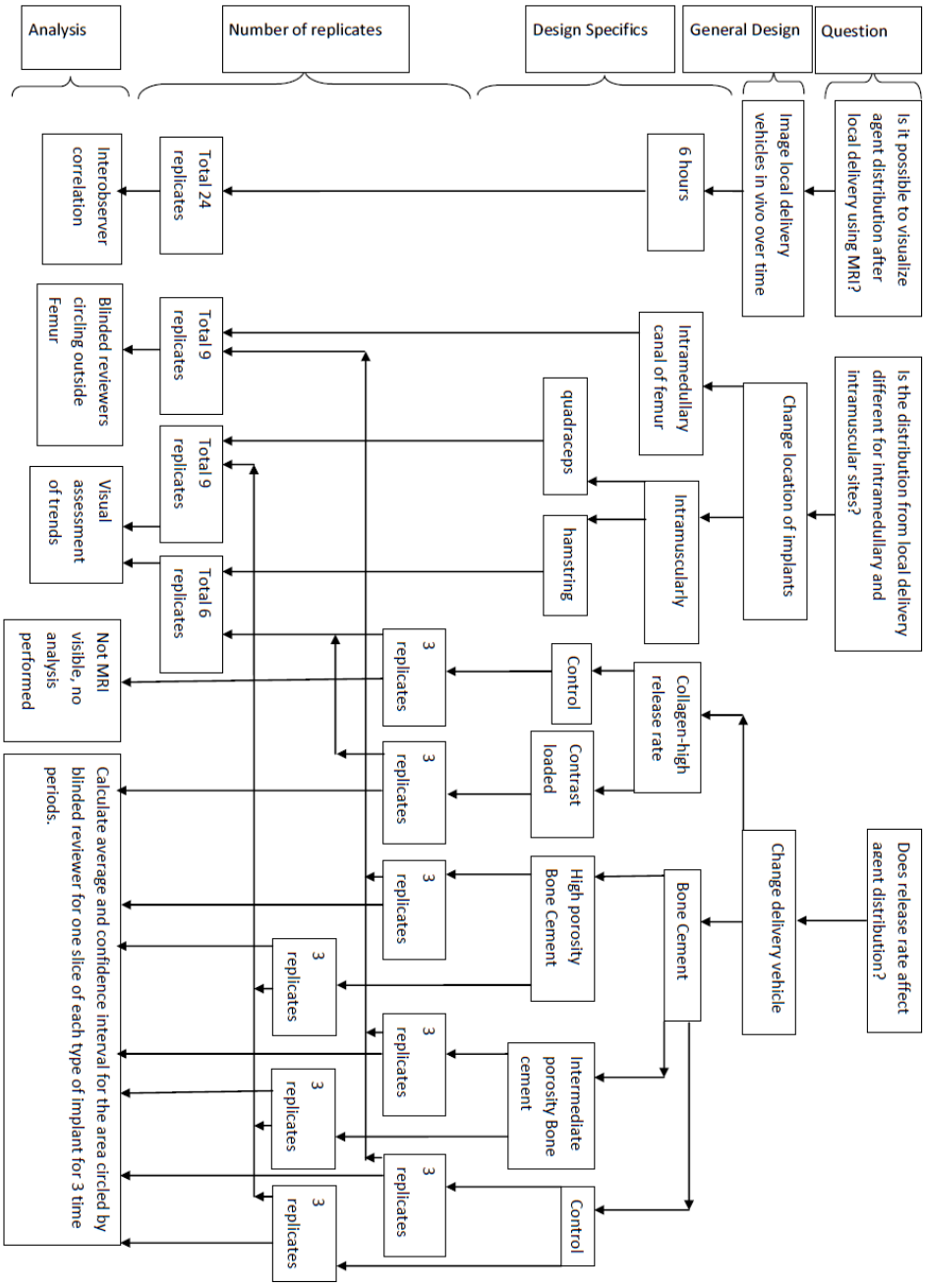

Figure 2.1: A diagram of the experimental setup is shown.

2.2.1 Delivery Vehicle Fabrication

Diethylenetriaminepentaacetic acid gadolinium (III) hydrate (Gd-DTPA) (Sigma-Aldrich, St Louis, MO, USA), a water soluble organic chelator loaded with gadolinium,

was used as a surrogate for gentamicin sulfate, a hydrophilic antimicrobial commonly used in depot delivery to treat orthopaedic infection. These two compounds have similar molecular size and solubility and therefore are expected to have similar transport properties (Table 2.1) [23,89].

Two types of delivery vehicles were used, collagen and polymethyl methacrylate bone cement (PMMA). To prepare the collagen vehicle, Gd-DTPA (Magnavist, Sigma-Aldrich, St Louis, MO, USA) in 150 mM phosphate buffered saline was mixed with 17 wt% porcine collagen (Sigma-Aldrich). The solution was heated to 60^{o} C to dissolve the collagen and produce a 100 mM Gd-DTPA gel.

Five types of PMMA delivery vehicles were formulated by Morgan Giers and Ryan McLemore. All PMMA orthopaedic bone cement was from Stryker (Simplex P bone cement; Stryker, Kalamazoo, MI, USA). All xylitol (Xlear, Orem, UT, USA) used was sieved using ASTM E-11 sieves to include only 250-425 μm particle sizes. The implant types are as follows:

(1) The control vehicles for both the intraoseous rods and intramuscular rods were made using the manufacturer's instructions (67wt% PMMA and 33wt% MMA).

(2) The high dose intraoseous delivery vehicle implants were made with 1.4wt% Gd-DTPA, 12.9wt% xylitol, a particulate porogen used to increase release rate and amount, and 85.7wt% PMMA and polymerized MMA.

(3) The intermediate dose intraoseous delivery vehicle implants were made with 1.4wt% Gd-DTPA, 6.2% xylitol and 92.4wt% PMMA and polymerized MMA.

(4) The high dose intramuscular delivery vehicle implants were made with 2.9wt% Gd-DTPA, 11.4wt% xylitol, and 85.7wt% PMMA and polymerized MMA.

(5) The intermediate dose intramuscular delivery vehicle implants were made with 2.9wt% Gd-DTPA, 4.7wt% xylitol, and 92.4wt% PMMA and polymerized MMA.

Doses were selected to be analogous with prophylactic doses of antimicrobial used in antibiotic loaded bone cement (ALBC) for fixation. Cement was formed into 9 cm long by 4 mm in diameter rods using 14 Fr. red rubber catheters (Covidien, Mansfield, MA, USA).

Table 2.1: Comparison of transport properties of antimicrobial and contrast agent.

Physical property	Gentamicin	Gd-DTPA
Molecular weight	478 g/mol	547 g/mol
Diffusion coefficient	2.1×10^{-6} cm^2/sec	4.0×10^{-6} cm^2/sec
Released from cement?	Yes	Yes

2.2.2 Surgical Procedure

Vehicles were implanted by orthopaedic surgeons Alex McLaren and Chris Estes either intramuscularly in the thigh or in the intraoseous canal of 9 female New Zealand White Rabbits, each 2.5 kg. Animals were sedated with ketamine (35 mg/kg), xylazine (5 mg/kg), and butrophanol (0.1 mg/kg) prior to surgery, and anesthesia was maintained on

2% isoflurane. Anesthesia was given and monitored by veterinary staff of Barrow Neurological Institute. A water blanket was used to maintain the rabbit's temperature at 37^{o}C.

Two types of rod placements were utilized: an intraoseous rod in the femur (IOR) and an intramuscular rod (IMR). To place a IOR in the left leg a 0.62 Kirschner wire was introduced into the femoral canal in a retrograde fashion through an entry point in the intercondylar notch. The Kirschner wire was removed and the canal was dilated to 4 mm using drill bits. A (PMMA) rod with composition 1-3 was then placed in the canal.

The right leg received an IMR, a PMMA rod with composition 1 or 4-5 placed intramuscularly in the quadriceps through a 5mm incision made 1-2cm proximal to the patella. Finally, an intramuscular injection of collagen (0.2mL) was placed in the hamstrings using a 20 G needle.

2.2.3 Image Acquisition

Imaging protocol was developed and performed by Qingwei Lui and Gregory Turner on a 7T MRI (Bruker Biospin; Billerica, MA, USA) using a rabbit coil. A fat-suppressed T_1 weighted RARE (rapid acquisition with relaxation enhancement) scan was used with repetition times (TR)= 1463,2000,3000,5000 ms (TE=9 ms). The region of interest included 42 equally spaced planes aligned along the long axis of the femur, stretching from the knee to the pelvis. Resolution was 0.3 mm x 0.3mm x 2.0 mm. A control image was taken of each animal prior to surgery. Total scan time was approximately 14 minutes per series. Each series of RARE images were used to construct a T_1 map through Bruker® software solving the Bloch Equation for T_1 given various

intensities at various TR (Fig 2.2) [63]. Animals were imaged for 6 hours at 15 minute intervals, and each set of RARE images were used to construct a T_1 map. T_1 maps were compared over both time and space for each subject to determine release profiles of gadolinium from local delivery devices.

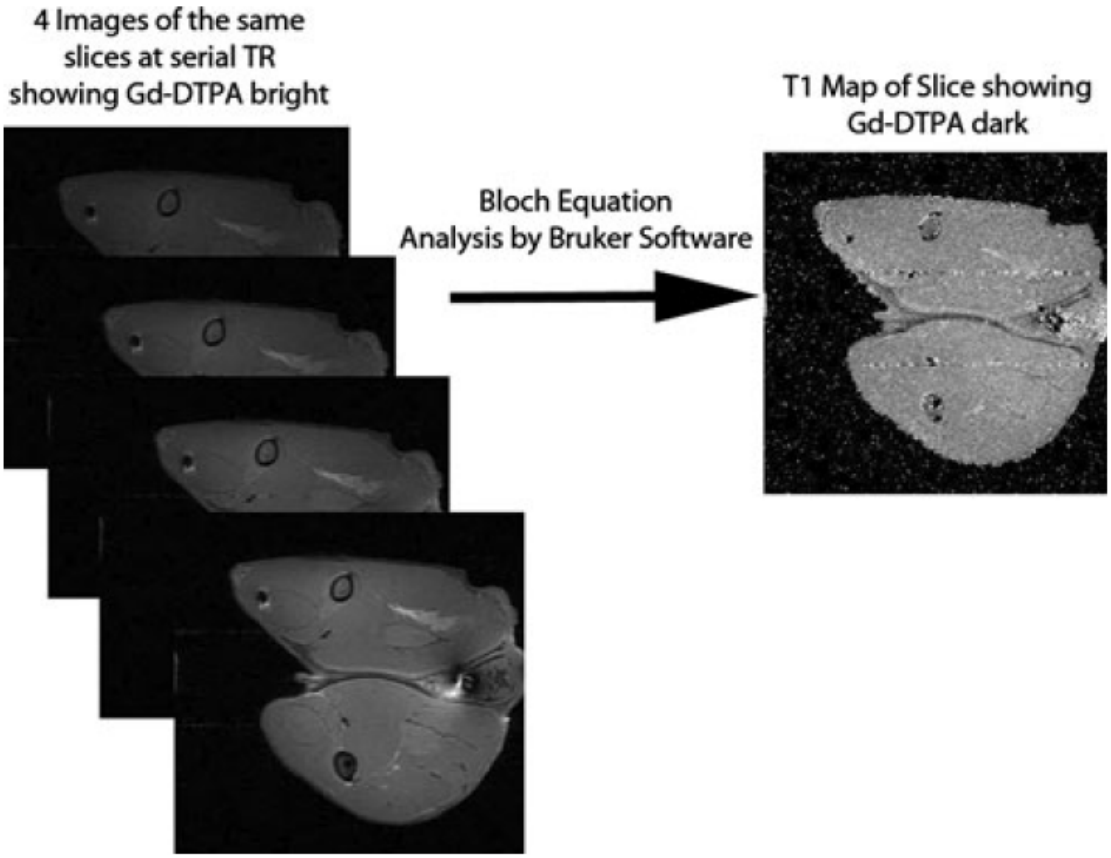

Figure 2.2: Multiple RARE scans of the same slice are assembled into a single T_1 map.

2.2.4 Euthanasia

Animals were euthanized at the close of experimentation. All procedures were approved by the Institutional Animal Care and Use Committee. National Institutes of Health guidelines for the care and use of laboratory animals were observed (Publication 85-23, revised 1985).

2.2.5 Interobserver Correlation

To determine interobserver reliability, three blinded observers (Jeffery Albigaard, James Fraser, Ryan Miller) were asked to review a subset of the images generated in this experiment. The observers were junior orthopaedic residents who were familiar with MRI but not familiar with the images generated in this project. Chris Estes trained all three observers by describing the project and demonstrating the technique to outline the area of visualized contrast on three sample images. The observers were then asked to outline the perimeter of the area where they visualized Gd-DTPA on 41 images prepared by Morgan Giers using MATLAB (Mathworks, Natick, MA, USA). The 41 images included three representative images from both PMMA and from collagen across the 6-hour period plus controls reviewed in random order. Interobserver reliability was determined by calculating interclass correlation coefficient (ICC) between all pairs of observers [100-102]. Bland-Altman plots were constructed and it was determined the interobserver reliability did not vary based on the average area.

2.2.6 Statistics

The effect of different in vitro release rates of the vehicle on distribution of Gd-DTPA was compared using quantitative data from the interobserver analysis by comparing distribution area over several time points. As a result of the inability to distinguish Gd-DTPA in collagen from Gd-DTPA in tissue, distribution area in this study is not an ideal metric for comparison of vehicles. The rate of change of area was calculated and normalized to the first postinjection image for each vehicle to determine if

distribution of delivered Gd-DTPA was affected by delivery vehicle. The rates of change between vehicles were compared using regression ($\alpha = 0.05$). Statistical analysis was performed by Morgan Giers and Ryan McLemore using Minitab 15 (Minitab Inc., State College, PA, USA) to construct Bland-Altman plots and check normality of data, MATLAB 7.9 (Mathworks) to calculate interobserver reliability coefficients, and Excel (Microsoft, Redmond, WA, USA) to perform t-Tests. All data used in t-Tests were confirmed to have a normal distribution through examination of the histogram of residuals and the normal probability plot.

2.3 Results

2.3.1 Is *In Vivo* Distribution of Locally Delivered Gd-DTPA Visible on MRI?

Contrast agent shortens the T_1 values and appears dark on the T_1 map. The control rods, containing no Gd-DTPA, show no shortening effect outside of the rod, indicating drug release is not seen. Control collagen is indistinguishable from the surrounding muscle on the T_1 maps. Gd-DTPA is visible spreading radially from all vehicles containing contrast. The visible area of the implant or implant and contrast as assessed during the interobserver correlation study was 27.5 ± 21.5 mm^2 for the rods with Gd-DTPA and 10.5 ± 11.2 mm^2 for rods without contrast ($p<0.001$).

All combinations of pairs of blinded observers produced an average ICC of 0.95 (range, 0.92–0.96).

2.3.2 Is *In Vivo* Distribution of Locally Delivered Gd-DTPA Affected by the Anatomic Delivery Site?

The spatial distribution differs between the two different rod placements, IMR and IOR. The contrast from the IOR remained inside the canal (Fig 2.3). The contrast from the IMR penetrated muscle until it approached an intermuscular tissue plane, where it then spread along the plane (Fig 2.4). Contrast was not observed to penetrate adjacent muscles.

2.3.3 Is *In Vivo* Distribution of Locally Delivered Gd-DTPA Affected by the *In Vitro* Release Rate from the Delivery Vehicle?

There is a visible difference between the distribution rates of the collagen compared to the bone cement. The area of the contrast from collagen decreased between 1 hour and 4 hours (p=0.007) (Fig 2.5), while the area of contrast from the PMMA rods did not change significantly over this time frame (p=0.417). The difference between the low and high dose bone cement formulations in the intraoseous canal is not apparent.

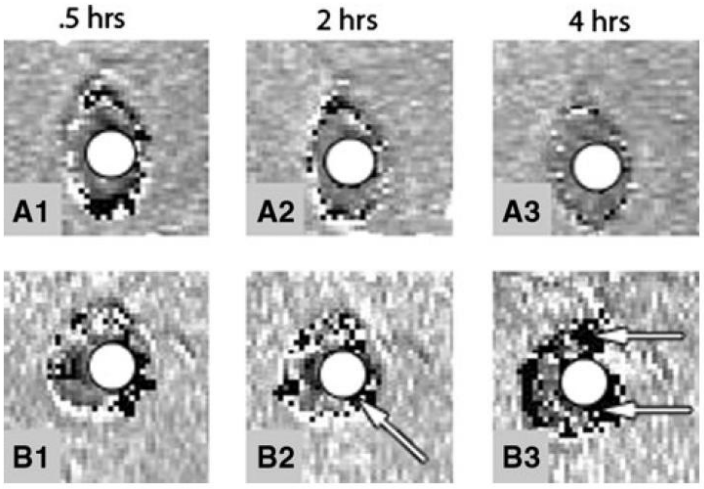

Figure 2.3: Intraoseous Gd-DTPA PMMA rods. (a) Control, no Gd-DTPA; and (b) intermediate dose Gd-DTPA is shown. Images are cross-sections perpendicular to the femur. The location of the implant is shown with a circle. The areas of low signal (white arrows) indicate drug release. (b1-3) show an increasing area of Gd-DTPA progressing with time. Images are from a similar location in the midthigh for both the (a) control and the (b) intermediate dose Gd-DTPA. The image series (a1–3) and (b1–3) are the same slice for the respective delivery site and animal at progressive time intervals to show change over time.

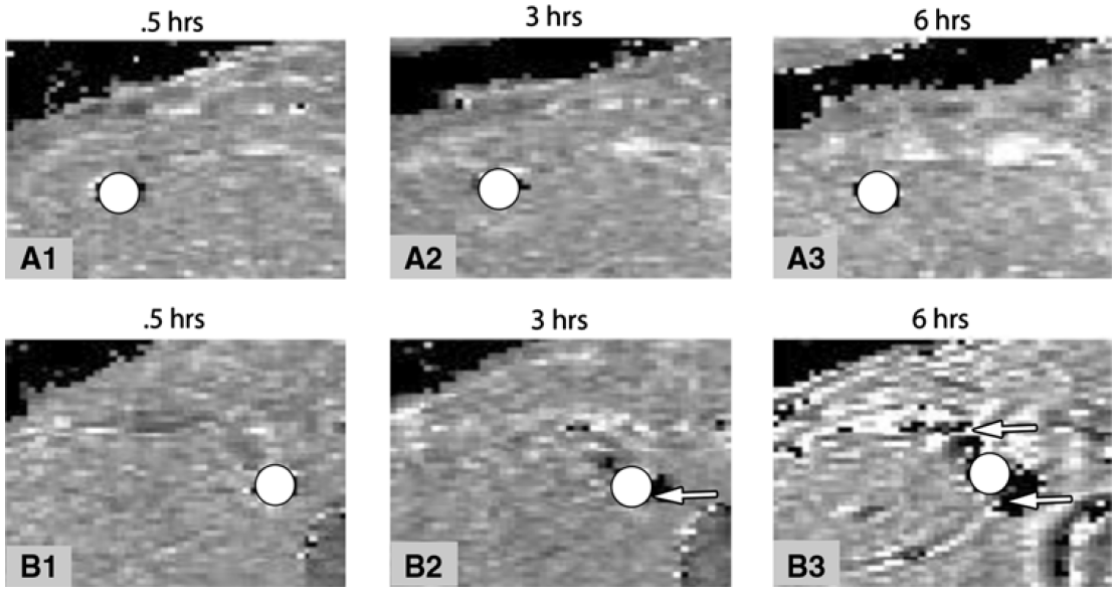

Figure 2.4: Intramuscular PMMA Gd-DTPA with (a) control, no Gd-DTPA and (b) high dose Gd-DTPA is shown. Images are cross-sections perpendicular to the femur. The location of the implant is shown with a white circle. Low signal adjacent to the rod (white arrows) indicates drug release. It is possible that the bright signal surrounding the contrast is related to progressive edema secondary to the trauma of inserting the rod. (b1-3) show

increasing area of Gd-DTPA progression with time. Images are from a similar location in the midthigh for both the (a) control and the (b) high dose Gd-DTPA. The image series (a1–3) and (b1–3) are the same slice for the respective delivery site and animal at progressive time intervals to show change over time.

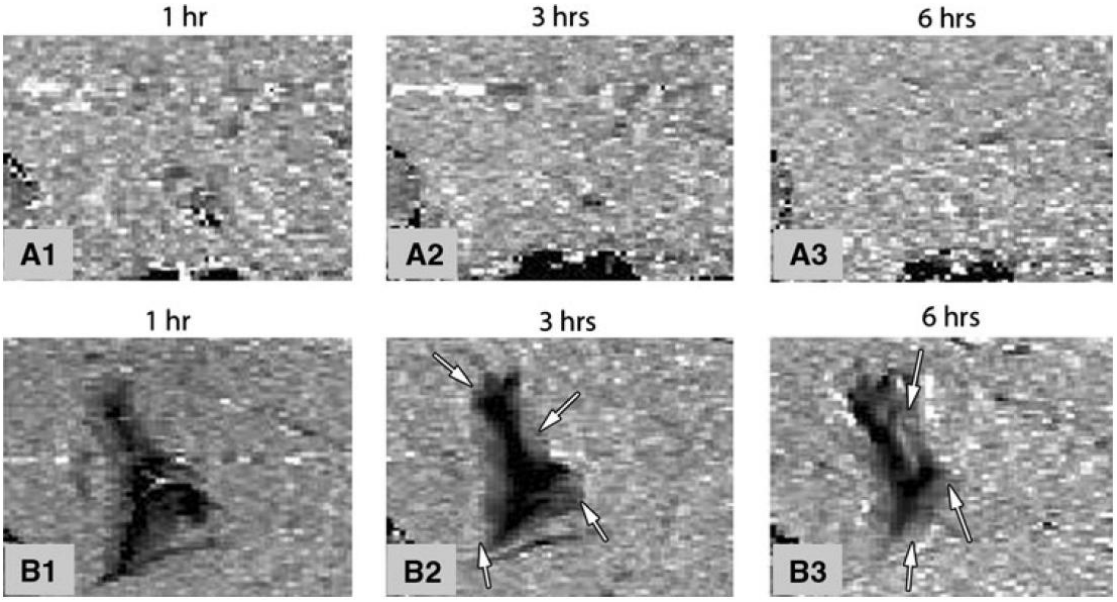

Figure 2.5: Images of collagen Gd-DTPA injections over 6 hours are shown. (a) No contrast and (b) 100mM Gd-DTPA. Images are cross-sections perpendicular to the femur from a similar location in the midthigh for both the (a) control and the (b) 100 mM Gd-DTPA. The image series (a1-3) and (b1-3) are the same slice for the respective delivery site and animal at progressive time intervals to show change over time. Arrows indicate released Gd-DTPA. (b1-3) show decreasing area of Gd-DTPA progression with time.

2.4 Discussion

This study was performed to answer the questions: is *in vivo* distribution of locally delivered Gd-DTPA visible on MRI? Is *in vivo* distribution of locally delivered Gd-DTPA affected by the anatomic delivery site? Is *in vivo* distribution of locally delivered Gd-DTPA affected by the *in vitro* release rate from the delivery vehicle? All of these questions have been satisfied with an answer.

Table 2.2: Relevant Literature

Study	Use of MRI	Depot material	Depot placement
Adams *et al.*[2]	Not used	bone cement Cefazolin, ciprofloxacin, clindamycin	Canine tibia
Astary *et al.*[75]	Effectiveness of brain injection	Local drug infusion Gd-DTPA-albumin	Rat hippocampus
Owen *et al.*[103]	Not used	bone cement Tetracycline	Rabbit femur
Nelson *et al.*[104]	Not used	fatty acid dimer-sevacic acid bead Gentamicin	Rabbit radius

There are several limitations of this study. First, this study was performed over a 6 hour period, a short timeframe compared to the expected duration of delivery from ABLC. The short timeframe could affect the ability to see statistically significant changes in drug distribution over time from delivery vehicles with slow release rates, such as the ABLC; however, since collagen has a faster release rate a 6 hour duration is sufficient to see changes in its distribution. In the future Morgan Giers, Chris Estes, Alex McLaren, Michael Caplan and Ryan McLemore plan to extend the timeframe of this study, but for the purposes of this pilot data 6 hours allowed us to draw meaningful conclusions about scan parameters and qualitative information about distribution patterns. Second,

conclusion were drawn by looking at T_1 values, but concentrations of contrast in the tissue were not calculated. There is literature available where concentrations of contrast agent were able to be calculated from T_1 values, but these occur mostly *in vitro.* There are several challenges associated with *in vivo* calculation of contrast concentration. Contrast concentration calculation is normally performed using a pre-contrast and post contrast per pixel T_1 value, but since the rabbit must be removed from the coil to perform the surgery it is difficult to properly align these two images. I continue to develop techniques to resolve this image processing challenge. Third, Gd-DTPA is only a surrogate for an antimicrobial and has no actual antimicrobial properties. Gd-DTPA was chosen for its similar transport properties to gentamicin, but also for the several logistical simplicities including: availability as an FDA approved drug, low cost, and available literature. Complex chemistry must be performed to transfigure any antimicrobial into an MRI visible molecule. Such chemistry is currently being performed by this group. Fourth, although Alex McLaren and Chris Estes attempted to keep the surgical procedures consistent, slight differences in the surgery and anatomy of the animal could be responsible for some of the distribution behavior. Although animal to animal variance can reduce statistical significance, it also is a more realistic model of the clinical use of *in vivo* drug delivery. Fifth, local drug delivery is volumetric and should be analyzed for the entire implant, where here only a subset of the images were analyzed. Finally, this study was performed in healthy tissue. The transport properties in that local environment could be effected by the presence of biofilm from an infection.

The data gathered show definitive trends. The control showed no change with time, as expected. The only difference before and after implantation was the presence of

the implant, which appears dark as it has no water. The dark spots visible around depot devices in all other images of Gd-DTPA containing implants are dynamic over time and show that it is possible to view drug delivery using MRI. Furthermore, the high correlation of the areas circled by non-expert blinded reviewers show regions of contrast can be consistently and reliably identified. From published data on MRI contrast sensitivity visible contrast is estimated to have concentrations larger than 100 μg/mL [84]. From the estimated sensitivity this data would appear fairly consistent with tissue delivery studies of antimicrobials performed by Adams *et al.* [2], Nelson *et al.* [104], and Owen *et al.* [103] The data from this group (Morgan Giers, Chris Estes, Alex McLaren, Michael Caplan and Ryan McLemore) showing dynamic changes over time make it consistent with the studies by Raghavan *et al.* and Astary *et al.* who studied MRI contrast infusion in the brain over time [75,76].

There were differences between the behavior of the cement rods in the two different locations. The contrast delivered to the intraoseous canals remained there, and the contrast delivered to the muscle showed a preference for moving along tissue planes. These results have not previously been reported by other groups.

Distribution is effected by delivery vehicle release rate. Collagen releases most of its load in 24 hours [8], but bone cement release can last 28 days or more [2]. In elution studies PMMA and collagen show similar release profiles where there is an initial burst release followed by a period of decline. In a four hour timeframe a change over time for the ABLC release was not seen, but a change in distribution area for the collagen vehicle was seen. The difference in rate of change in area for the two different vehicles indicated

that this method can provide information on distribution as a function of vehicle release rate.

2.5 Conclusions

In conclusion, MRI can be used to view antimicrobial surrogate distribution from orthopedic implants. Furthermore, spatial and time dependent distribution can be determined. There was a difference seen between depot material and placement. This imaging process could serve as a noninvasive and efficient method for studying drug delivery from depot devices.

Chapter 3: SPATIOTEMPORTAL QUANTIFICATION OF LOCAL DRUG DELIVERY USING MRI

3.1 Introduction

Controlled release formulations for local drug delivery are of growing interest to device manufacturers, research scientists, and clinicians. There are many current and potential applications for controlled release devices, including cancer treatment [3], pain management [4,5], tissue engineering [6], and infection treatment [7]. For decades orthopaedic infection management has relied on the use of antimicrobials delivered from bone cement at the infection site [14]. There are an estimated 112,000 total orthopaedic infections of arthroplasties and fracture-fixation devices per year [16], and this number is expected to increase as the projected number of arthroplasties will likely increase by several fold over the next 18 years [18]. Approximately $1.8 billion is spent annually on increased medical costs due to orthopaedic infection of total joint arthroplasties in the US [16]. Orthopaedic implant infections result from common human skin microbes, such as *Staphylococcus epidermidis* and *Staphylococcus aureus*, and are often complicated by biofilm formation. Biofilm residing microbes are not only protected by transport limiting polysaccharide matrix, but are more resistant to antimicrobials [22]. Antimicrobial concentration of 100-1000 times the usual minimum inhibitory concentration (MIC) used to treat planktonic microbes are required to treat infections with biofilm effectively [25,26]. Intravenous delivery to achieve these antimicrobial levels will cause serious systemic toxicity for most of the antimicrobials used to treat implant infections. Local drug delivery at the site

of orthopaedic infection is used to achieve effective concentration of antimicrobial without systemic toxicity.

Even though antimicrobial loaded bone cement (ALBC) is intended for *in vivo* use, most release studies of antimicrobials from ALBC have been performed *in vitro*. For instance, researchers commonly characterize drug elution profiles from controlled release formulations by placing samples of known geometry under near infinite sink conditions, such as a large volume of frequently exchanged fluid [46,47]. While release studies give valuable information necessary for directly comparing different controlled release formulations, it does not represent how or where the drugs will distribute when the device is implanted. Infinite sink conditions produce the greatest possible release of drug which represents the potential release capability not the actual elution profiles likely to be achieved *in vivo*, where mass transport resistances from the surrounding tissue are likely to decrease the rate of release. *In vivo* studies have been performed [1,2,53,58], but none provide comprehensive information on the spatial and temporal distribution of drug delivery. *In vivo* tests frequently focus on efficacy, such as infection control [58], but do not provide detail regarding how the antimicrobial is distributed because this is difficult, expensive, and time consuming to measure. *In vivo* animal experiments that do consider spatial distribution of antimicrobial commonly utilize tissue biopsies near implants and collect fluids, such as seroma, blood, and urine [1,2,53]. These techniques are time consuming to analyze, not comprehensive (e.g., resolution is low due to limited number of samples), and of limited clinical applicability to humans due to their invasiveness and requirements for multiple sampling.

Magnetic resonance imaging (MRI) has been used to visualize distribution of drugs delivered locally in several clinically relevant applications. Drug delivery from catheters in convection enhanced delivery procedures for treatment of glioblastomas has been studied by multiple research groups [75-78]. Sarntinoranont and co-workers have studied delivery of gadolinium diethylenetriaminepentaacetic acid (Gd-DTPA) to tumors [79], and they calculate concentration of the Gd-DTPA using a method validated in an agarose phantom [80]. Several other groups have calculated concentrations of contrast agent *in vitro* as well [73,81-84]. However, their methods of quantification are not validated *in vivo* to determine sources of error or to quantify the error likely in their *in vivo* measurements. Sampson and co-workers also deliver MRI contrast agents to tumors, but no quantification of the agent's concentration is performed [76,77]. Krauze *et al.*[78] and Port *et al.* [85] imaged liposomal Gd-DTPA delivery, but neither quantified concentration. Kim *et al*. quantified the distribution of drugs delivered from an ocular implant using MRI [87]; however, the function used by Kim *et al.* to convert MR intensity to concentration is similar in shape to a parabola and thus results in two valid concentrations for most MR intensity values – one concentration being high and the other being low concentration; thus, the user must infer which concentration is more likely based on proximity to the depot.

In this work, *in vivo* MR imaging of local delivery of Gd-DTPA from polymethyl methacrylate (PMMA) bone cement was converted to Gd-DTPA concentration to provide time-resolved maps of Gd-DTPA concentration. The contrast agent, Gd-DTPA, was chosen because of its similar solubility and diffusion coefficient (4.0×10^{-6} cm^2/sec) [89] to the antimicrobials Vancomycin (3.64×10^{-6} cm^2/sec)[90] and Gentamicin (2.08×10^{-6} cm^2/sec)

[23], which are common choices to treat infected orthopaedic implants. This chapter presents a detailed protocol for performing this method on an animal model. Further, sources of error are discussed and quantified when possible. Finally, methods of image volume registration are demonstrated and compared to the method proposed here (average value of pre-contrast T_1 applied to all voxels).

This research was conducted as a collaboration between Morgan Giers, Alex McLaren, Jonathan Plasencia, David Frakes, Ryan McLemore, and Michael Caplan. These data are accepted for publication in the journal Computational and Mathematical Methods in Medicine [105]. Specific contributions of each team member are stated in the corresponding sections in the methods; however it should be additionally noted that all team members participated in analyzing and interpreting the data.

3.2 Methods

3.2.1 Delivery Vehicle Fabrication

Delivery vehicles were prepared by Morgan Giers and Ryan McLemore. PMMA bone cement was formed using Simplex P® bone cement (Stryker, Kalamazoo, MI, USA). Control implants, with no contrast agent, were made according to the manufacturer's instructions. Experimental implants were made identically with the addition of either (a) an additional 2.1vol% (2.9wt%) Gd-DTPA, an MRI contrast agent, 8.8vol% (11.4wt%) xylitol, a particulate porogen used to increase release rate and amount, and 89.1vol% (85.7wt%) PMMA and polymerized MMA or (b) an additional 1.1vol% (1.4wt%) Gd-DTPA, 9.9vol% (12.9wt%) xylitol, and 89vol% (85.7wt%)

PMMA and polymerized MMA. Implants of all compositions were formed into 3 mm diameter x 7 cm long rods using a red rubber catheter (Covidien, Mansfield, MA,USA) as mold.

3.2.2 Surgical Procedure

All procedures were compliant with the National institute of Health guidelines for the care and use of laboratory animals and approved by the Institutional Animal Care and Use Committee. All studies were performed using New Zealand White rabbits.

In the first set of procedures, cylindrical shaped implants were placed by Alex McLaren and Chris Estes in either muscle, intramuscular rod (IMR) or the intramedullary canal of the femur, intraoseous rod (IOR). The right quadriceps of each animal received an IMR of either the experimental (2.1vol% Gd-DTPA,8.8vol% xylitol, 89.1vol% PMMA and polymerized MMA) (n=3) or control (no Gd-DTPA, no xylitol)(n=3) cement composition. The left femur of each animal received an IOR of either the experimental (1.1vol% Gd-DTPA, 9.9% xylitol, 89vol% PMMA and polymerized MMA) (n=3) or control (n=3) composition. These procedures are described in previous work by these authors [99].

In a second set of procedures (performed by Alex McLaren and Kenneth Schmidt), either a partial thickness of muscle (PTM) or a full thickness of muscle and bone (FTMB) was removed and replaced with bone cement. For the FTMB wound, muscle tissue was removed and a femoral window was created. The femur and muscle received cement containing Gd-DTPA. Only the skin was closed over the wound using suture. In the PTM model, muscle was removed, the dead space was filled with cement

containing contrast. The muscle, fascia lata, and skin were closed with suture. These procedures are described more thoroughly in other work by these authors [106].

3.2.5 Image Acquisition

A series of T_1-weighted rapid acquisition with relaxation enhancement (RARE) scans were taken by Gregory Turner and Qingwei Lui at repetition times (T_R) of 1463, 2000, 3000, and 5000 ms (RARE=2 and no averages) on a Bruker Biospin® 7-T MRI (Bruker Biospin, Billerica, MA, USA) every 15 minutes for 4-6 hours (Fig 3.1a). A 15-cm quadrature transceiver coil was used. Flip angle of the RF pulse was calibrated by the Bruker software before each scan. The images did not have ghosting artifacts, indicating the calibration was successful. The images were taken with coronal slices from knee to hip, 42 slices total (field of view=12 cm), with a voxel size of 0.3mm x 0.3mm x 2mm, where the slice thickness was 2 mm, and a matrix size of 256x256x42. The temporal resolution was 14 minutes. The series of T_1-weighted images at different T_R was used by the Bruker software to construct a longitudinal relaxation time, T_1, map based on the solution to the Bloch equation:

$$S(T_R) = S_0(1 - e^{-\frac{T_R}{T_1}}) \qquad \text{(eq3.1a)}$$

$$S_0 = k\,\rho\, e^{-\frac{T_E}{T_2}}$$

(eq3.1b)

where S was the signal intensity, T_R was repetition time (time between RF pulses), T_1 was the longitudinal relaxation time, and S_0 was defined in equation 3.1b where k was the proportionality constant based on instrument factors, ρ was the spin density, T_E was the

echo time, and T_2 was the transverse relaxation time [63]. The estimated error of the T_1 map construction process was calculated by taking the residuals of the curve fitting process for 1 pixel. In a T_1-weighted image, contrast, and fat appeared bright; whereas, cement and bone appeared dark as seen in figure 3.1a. In the T_1 map, fat appeared bright; whereas, contrast, bone, and cement appeared dark as seen in figure 3.1b.

3.2.5 Image Processing

All image processing was performed by Morgan Giers (with the exception of the registrations discussed later in this section) with significant input from David Frakes, Michael Caplan, and Ryan McLemore. The T_1 maps were imported into MATLAB® (Mathworks, Natick, MA, USA). In MATLAB the images were treated with a noise reducing filter. The filter acts only within an image slice and changes a pixel to the median value based on the pixel and its 4 nearest neighbors' original values. The 4 nearest neighbors are the pixels directly above, below and to either side of the central pixel. The filter is applied uniformly to all pixels in the image slices, without regard for location in the image. The filtering results are shown in figure 3.1c. Subsequently, a binary mask of the leg area was made by morphologically opening the filtered T_1-weighted image slice, applying a binary threshold, filling holes, and removing groupings of pixels less than 100, the morphologically closing the image slice. The binary mask of the leg area was used to mask noise from outside of the legs in the T_1 map (Fig 3.1c). A histogram of the cleaned image was then calculated. The histogram was made symmetric by replicating the portion of the histogram with T_1 values greater than the peak value. The symmetry of the histogram removed pixels containing contrast, cement, and air

outside of the legs and create a Gaussian distribution. Then the average value and standard deviation from the symmetric histogram was calculated. After the average histogram value was obtained both the T_1-weighted and T_1 map image slices were exported from MATLAB as a series of TIFF files. The TIFF images were imported into Mimics® (Materialise, Leuven, Belgium), where the T_1 map was thresholded to a value of one standard deviation below the average value of the symmetrical histogram. The threshold level was determined to align with segmentations performed by a group of experts. All pixels within the muscle tissue of the leg were segmented from the thresholded region. Then, all the pixels connected to the implant in the muscle tissue region were segmented. This segmentation gave a region of all the pixels connected to the implant within the muscle of the leg, which included the cement implant and contrast agent After muscle implants and contrast were segmented several steps were performed to segment contrast within the intramedullary canal of the femur. Both the intramedullary canals of the femur from the same rabbit were segmented from the T_1-weighted image volume using a semiautomatic gradient flow detection algorithm, which is similar to the method shown by Karasev *et al.*[107]. Only the fat and marrow within the intramedullary canal was included in the segmented region, excluding the cortex of the femur. The mask of the segmented region from the femur without contrast was imported back into MATLAB, where a symmetric histogram was created for the intramedullary space. The histogram was made symmetric to remove pixels from outside the masked region, which were given a value of 0. The average and standard deviation of the symmetric histogram was calculated. In Mimics the masked intramedullary space of the femur containing an implant and contrast agent was thresholded to one standard deviation below the average

value of the histogram of the intramedullary canal containing no contrast from the same rabbit. All pixels connected to the cement implant within this thresholded region were segmented. Additionally, the exterior of the cortex of the femur was segmented using a semiautomatic gradient flow detection algorithm in Mimics and manual correction. The femurs were then processed with a 3D object smoothing function and included as an anatomical reference in 3D images. The legs were also segmented for an anatomical reference using thresholding, manual correction, and 3D object smoothing. The segmented femur, legs, and contrast were plotted together as 3D objects using Mimics as shown in figure 3.1h. The segmented regions of contrast and cement were exported as a series of mask images in a bitmap format. The bitmaps were imported back into MATLAB where they were transformed into a binary image mask. The binary image mask was multiplied by the T_1 map to give a map in only the area of contrast (Fig 3.1d). The contrast region was transformed into a concentration map (Fig 3.1e & 3.1f) using:

$$\frac{1}{T_1} = \frac{1}{T_{1,0}} + r_1 C \qquad \text{(eq3.2)}^{68,80,81}$$

where $T_{1,0}$ is a pre-contrast T_1 map value and T_1 is the post-contrast T_1 map value. For equation 3.2 the average symmetrical histogram values per tissue (muscle or intramedullary canal) within a single rabbit was used for $T_{1,0}$. The value 0.0038 $mM^{-1}s^{-1}$ was used as the value for r_1[70]. The relaxivity value was chosen because it is near many reported values for relativity measurements for Gd-DTPA in tissues at 3-7T. Rohrer *et al.* obtained this relaxivity value for Gd-DTPA relaxation in serum at 4.7T [70]. The concentration map was superimposed onto a T_1-weighted image to provide the anatomical details as shown in figure 3.1g.

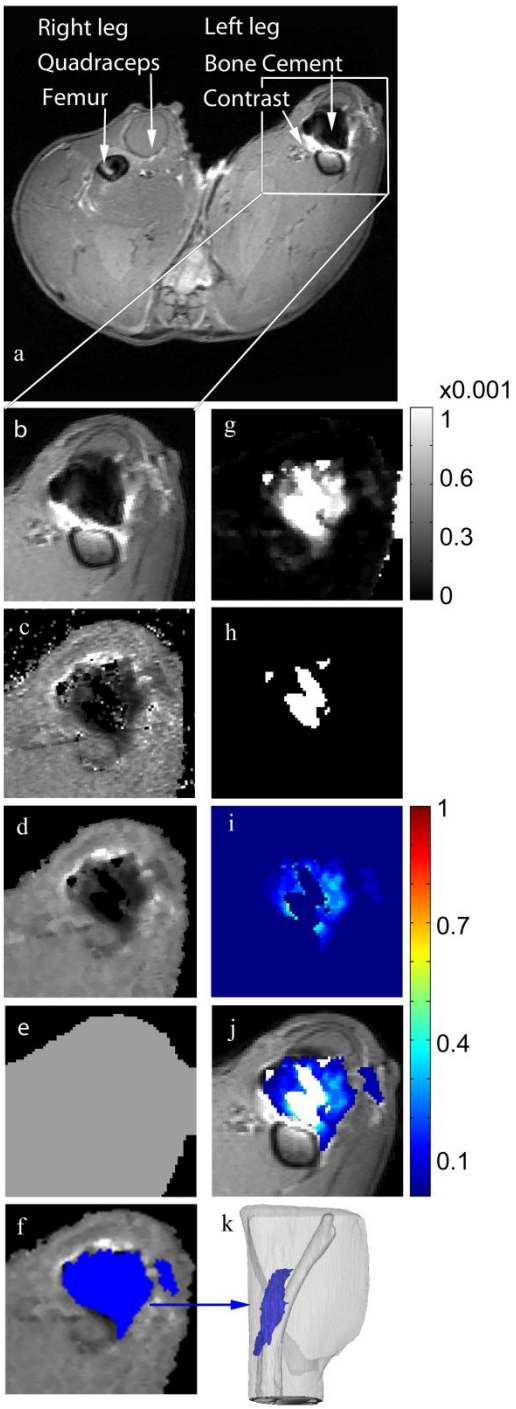

Figure 3.1: (a) T_1-weighted image, (b) ROI of T_1-weighted image (c) Original T_1 Map, (d) Filtered and masked T_1 map, (e) $T_{1,0}$ calculated from the average of the symmetric histogram of (d), (f) segmented region of contrast, (g) $1/T_1$-$1/T_{1,0}$ or 1/(d)-1/(e), (h)region

where T_1=na, (i) concentration map where the scale is in mM, (j) concentration map superimposed onto T_1-weighted image, (k) 3D reconstruction from Mimics.

To avoid spatially registering a pre-contrast and post-contrast image volume, the assumption of isotropy of the $T_{1,0}$ value within a certain tissue type was made. To evaluate if a single value for different animals could be used, histograms of 5 pre-contrast rabbits (rabbit #1,8,9,15,18 in the series) were composed. The average value of these histograms was used as the $T_{1,0}$ value for all images. The standard deviation of the compiled 5 histograms was also calculated. Concentrations were plotted for different T_1 values using the mean $T_{1,0}$ value with error bars, $T_{1,0}$ one standard deviation greater than and less than the mean $T_{1,0}$. The standard deviation was chosen instead of a 95% confidence interval because the standard deviation was greater than the confidence interval and would show greater potential error. To evaluate if one value could be used for multiple tissue types, histograms were calculated for the femur and the muscle separately.

Next the isotropic $T_{1,0}$ technique was compared/contrasted with using T_1 values from an image in which no contrast is present. This requires that the image volumes with no contrast be spatially registered to the image volumes with contrast present. Such a registration was completed for one image set. First a 3D rigid body affine registration was performed by Jonathan Plasencia in which matching points on the femur in pre-contrast and post contrast images were chosen by Morgan Giers. A transformation matrix was created by Jonathan Plasencia and optimized using singular value decomposition similar to a method outlined by Eggert *et al.* [108]. The pre-contrast image volume was

transformed using a 3D linear interpolation algorithm, which used Delaunay triangulation to handle the scattered data points. Then a 3D deformation registration was performed by Jonathan Plasencia using points picked by Morgan Giers from the affine registered pre-contrast image and post contrast image. A transformation map was generated by Jonathan Plasencia by calculating the difference between current and desired point location for the points chosen, then interpolating all the surrounding pixel values using linear interpolation. The image volume was transformed using the same linear interpolation algorithm as in the affine registration.

The T_1 to concentration conversion equation (Eq 3.2) is only valid for a certain concentration range. Outside that concentration range there is nonlinearity in the actual concentration to T_1 relationship that is not captured by the equation. The difference was quantified by scanning of a series of vials containing known concentrations of contrast in 2wt% agarose, converting the average T_1 value for each vial into a concentration. and comparing the calculated concentration to the actual concentration.

3.2.5 Image Analysis

Volumes of segmented contrast, including the cement implant, were calculated by Morgan Giers. These were adjusted by subtracting the volume of cement implanted, as calculated from the weight of the implant (see details of the surgical insertion). The volumes of the region where T_1=na, which includes the cement implant and a region of extremely high concentrations of contrast (>50mM), was calculated. Total mass of contrast agent was calculated by summing all concentrations from pixels with a real T_1 value and multiplying by voxel volume (0.18 μL).

3.2.6 Statistics

Volumes and total mass were analyzed by Morgan Giers for significance by two way ANOVA (wound types and presence of contrast agent: experimental IMR, experimental IOR, control IMR, and control IOR) using Minitab® (Minitab Inc., State College, Pa, USA). All data used in ANOVA were confirmed to have a normal distribution through examination of the histogram of residuals and the normal probability plot. *Post hoc* t-Tests were performed when $p<0.05$ by ANOVA.

3.3 Results and Discussion

3.3.1 How Good are T_1 Maps?

Equation 3.1 was used to calculate T_1 from the intensity values from a set of T_1-weighted images taken at different relaxation times (T_R). The fitting is performed pixel-by-pixel using equation 3.1. There is noise in the T_1-weighted images; thus there is noise in the T_1 value obtained. The noise in the T_1 values depends on the signal to noise ratio (SNR) of the image acquisition method used. $\ln(S_0/(S_0-S))$ is plotted vs. T_R for a single pixel in the muscle of specimen 4 (Fig 3.2); the inverse of the slope is the T_1 value, and an estimate of the error can be determined from the residuals (Fig 3.2). For the pixel in figure 2, the T_1 value is 2500 ms, and the residuals squared are 0.96, indicating a good fit is achieved. Noise is visible as graininess in the T_1 map image (Fig 3.1b). Including more values of T_R decreases the error and improves the calculation, but requires longer image acquisition time. The time required for the scan is also a function of the T_R values chosen,

number of slices, and resolution desired. For the 4 T_R values used here (1463, 2000, 3000, and 5000 ms), 42 slices and 0.3mm x 0.3mm resolution, a scan takes 14 minutes. Certain applications, such as imaging a beating heart, require a fast measurement time. In those cases, a 14 minute scan is unacceptable so a single T_1-weighted image can be used in such cases [81,83,86]. These methods typically result in greater error, but the error can be offset by acquiring a greater number of replicates.

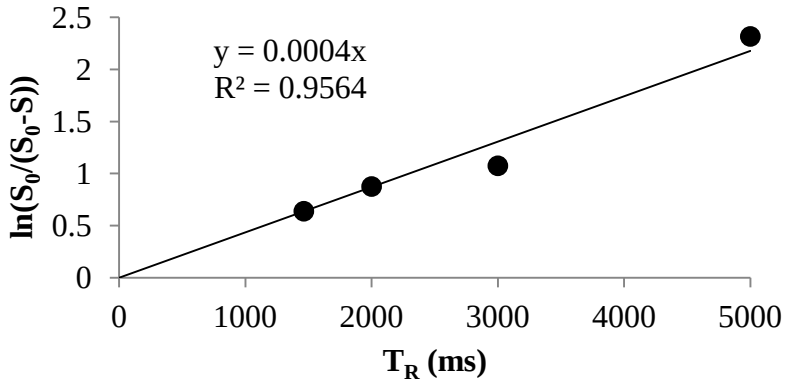

Figure3. 2: A plot of signal intensity from the T_1 weighted images at different T_R, for one pixel, used to determine T_1 value.

3.3.2 What does Filtering do?

Next, the T_1 map is filtered to decrease noise (Fig3.1c). Filtering increases confidence that voxels included as containing contrast are not a product of noise, but filtering also reduces the ability to detect small features in the image slice In order for a voxel to be included as having contrast, at least two neighboring pixels must also have contrast. Subsequently a single voxel that contains contrast will be excluded from the image and that pixel will then be changed to the median value of the surrounding pixels. Other sharp features such as tissue planes can be replaced or thinned with the surrounding

muscle tissue values, blurring the image. The higher the order of the filter, number of neighbors included, the more severe the effects of the filter. At the order used here, 5th order, much of the noise appears to be removed, but features such as tissue planes can still be seen.

3.3.3 How Consistent is Segmentation?

Next, the pixels containing contrast agent are identified (Fig 3.1e,f). Identification of contrast requires segmenting the contrast within certain tissue types. In order to see the main body of distribution the regions not connected to the main body are excluded. By only including regions that are connected within a single tissue type the regions of contrast are very reproducible. Even without restricting to a single tissue type in previous work by these authors, blinded reviewers chose areas of contrast from image slices thresholded at 1400 ms, and there was good agreement among reviewers (interclass correlation coefficient=0.92-0.96), indicating reproducible results [99]. In the present work the method was made even more robust by thresholding at a level based on the longitudinal relaxation times within a single tissue, and including all connected voxels within that threshold.

3.3.4 How Reliable are the Concentration Values?

Concentrations were calculated by applying equation 3.2 to each pixel containing contrast agent. Pixels with a T_1 value of na were not assigned a concentration. The equation relates T_1 with contrast concentration, but it is only accurate within a range of concentrations. At low concentrations, which produce T_1 values close to native tissue, the

likely error between the calculated and actual concentrations is fairly large (Fig 3.3); however, the error is skewed so that the actual concentration is not likely to be much greater than the calculated value, but the actual concentration may be substantially less than the calculated value. At high concentrations, approaching the signal intensity saturation limit, an artifact occurs that yields T_1 = na in the pixel of interest but can also effect the intensity of pixels nearby resulting in an incorrect image (Fig 3.4). The range of concentration between these high (saturation leading to artifact) and low (resulting in no contrast) values should be considered when choosing the amount of contrast agent to load into the drug delivery vehicle. The concentration of Gd-DTPA loaded into the ALBC in this study (67 mM) is great enough to allow for an artifact to occur. Most images are unaffected because the Gd-DTPA in the ALBC is not near water and, once it is released into the volume surrounding the ALBC, it quickly becomes diluted to less than the concentration causing artifacts; however, in some images, high concentrations near the femur cause spatial morphing indicating an artifact. The magnitude of the artifact was estimated by comparing the volume of pixels where T_1=na between control and experimental implants. Regions where T_1=na where regions where the T_1 values were fitted by the software, but were calculated as too small to be reliable based on the shortest T_R values which were several hundred milliseconds long. The region where T_1=na includes the volume of the cement implant, which is not hydrated enough to be visible to on the MRI, and the volume of artifact surrounding the implant. There will be no artifact resulting for contrast agent in the control images. If there was a significant amount of artifact or super-threshold gadolinium near the implant in the images with contrast the volume of pixels where T_1=na would be higher than in the control images. From the

ANOVA there is no statistically significant differences between the control and experimental (p=0.86), indicating that artifacts present are not large enough to significantly affect the experiment. The possibility of artifacts must be balanced against the necessity for visualization of contrast agent further away from the implant when choosing the Gd-DTPA loading amount.

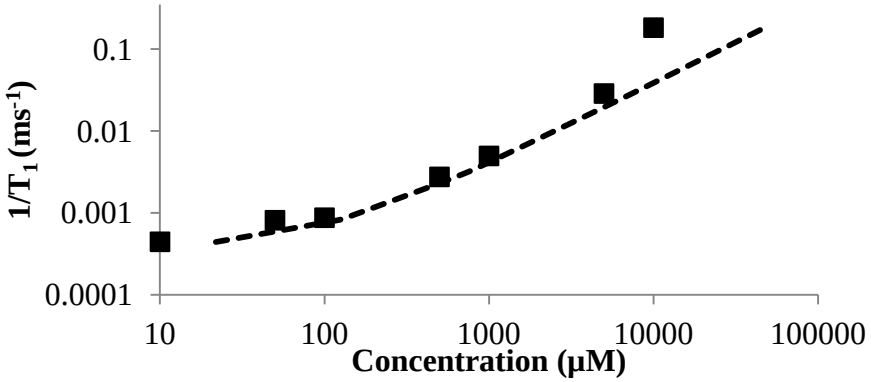

Figure 3.3: T_1 maps were acquired for a series of different concentrations of Gd-DTPA prepared in agarose gel. The plot shows the difference between actual concentration (squares) and concentration calculated using equation 3.2 (dashed line) .

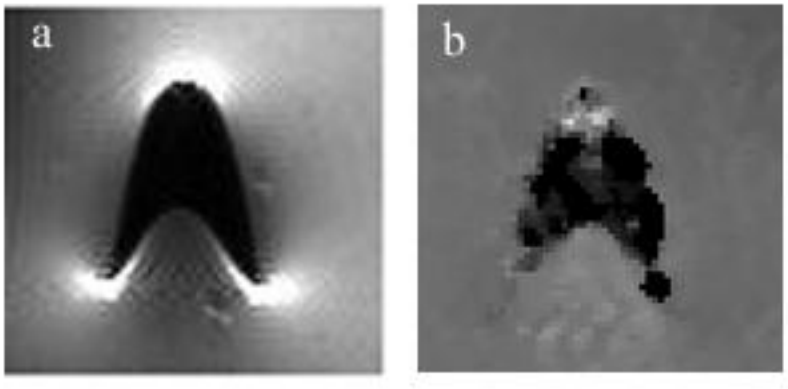

Figure 3.4: (a) T_1-weighted image and (b) T_1 map of a vial of 100 mM Gd-DTPA which creates an artifact. The dark portion of the images should be round, and the dark portion of the T_1-weighted image should be bright.

The histograms of five pre-contrast image volumes were analyzed to find the mean T_1 value of tissue containing no contrast agent (2817±852 ms) (Fig 3.5) to evaluate if a single value could be used across multiple animals. The mean (2817±852 ms) provided similar information to the histogram peak values (largest count number in the histogram) for the 5 rabbits shown (2815±132 ms). Animal to animal variability can be assessed by comparing a single histogram's mean and standard deviation (2905±834 ms) to the mean from the compounded 5 rabbit histogram (2817±852 ms), whose deviation overlaps considerably. Despite the fact that $T_{1,0}$ values can vary with metabolic activity, the animal to animal variability is small relative to the spread of the histogram. Thus error from animal to animal variability is less than error due to differences within a single animal. This indicates that there is minimal error introduced by using the 2817 ms value for all animals rather than using a value determined for each animal. So while less error is introduced by using a different value evaluated for each animal, if it is not possible to

accurately evaluate a precontrast value a value from a different animal or an average value from multiple animals could be used.

To quantify error likely resulting from using an isotropic value of $T_{1,0}$ rather than a registered pre-contrast image volume to provide a pixel-by-pixel value of $T_{1,0}$, Michael Caplan and Morgan Giers applied equation 3.2 to T_1 values between 0 and 1965 using $T_{1,0}$ = 2817 ms (mean), 3669 ms (+1 standard deviation), and 1965 ms (-1 standard deviation) (Fig 3.6). This provides a reasonable estimate of the effect that large variability in observed T1 would have on the calculation of concentration. Equation 3.2 applied to T_1=1650 ms results in a concentration of 66 ±22/40 μM (where the first error number is the difference calculated using $T_{1,0}$=3669 ms and the second number is the difference calculated using $T_{1,0}$=1965 ms). As can be seen in figure 3.6, error becomes less as T_1 decreases (actual concentration increases). Note that the error is unequal above and below the concentration. For T_1=1965ms, using $T_{1,0}$=3669 ms calculates a concentration value 54% greater than that calculated using $T_{1,0}$=2817 ms; whereas, using $T_{1,0}$=1965 ms calculates a concentration of 0 μM. (100% error). The error is always greater for lower concentrations. At low values of T_1 (high concentrations), the error is minimal. For example, T_1=51.5 ms results in a concentration of 5000 ± 20/40 μM (0.4%/0.8%).

The uneven error results in concentrations that are more likely to be overestimated rather than underestimated. Hence, pixels included as having contrast are likely not overestimating the concentration, but may not actually contain contrast. The concentration calculation error will be greater in some areas than in others. For example, the femur has a broader histographic distribution than the total image, as shown in figure

3.7, so in the femur, error will be greater than the previous estimate. The muscle is more isotropic than the total image so the error for calculations performed in muscle will be slightly less than the previous estimate. Therefore, using an isotropic $T_{1,0}$ value can give accurate order of magnitude information, but specific values, especially low concentration values, should be considered with caution. One potential clinical application of visualizing drug distribution is co-delivering Gd-DTPA with antimicrobials to determine if the infection is being treated effectively. For this application, the minimum effective concentration of antimicrobial is near the lower limit of detection of the isotropic $T_{1,0}$ technique (20-200 μM). At that lower limit, if a pixel shows as containing contrast ($T_1 \leq 2200$ms), it may or not contain effective concentration of antimicrobial; however, if a pixel does not show as containing contrast ($T_1 > 2200$ms), then it likely contains less than an effective concentration of antimicrobial. Therefore, it is unlikely that a patient would receive an additional intervention unnecessarily, but a patient requiring additional intervention could be evaluated to require no additional intervention allowing a risk that the infection could recur.

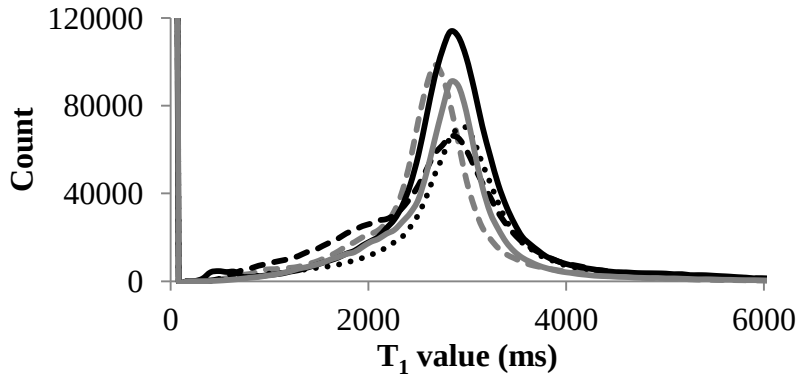

Figure 3.5: Histograms of 5 pre-contrast rabbit T_1 maps: rabbit 1 (dashed grey line), rabbit 2 (solid grey line), rabbit 3 (dotted black line), rabbit 4 (dashed black line), rabbit 5 (solid black line).

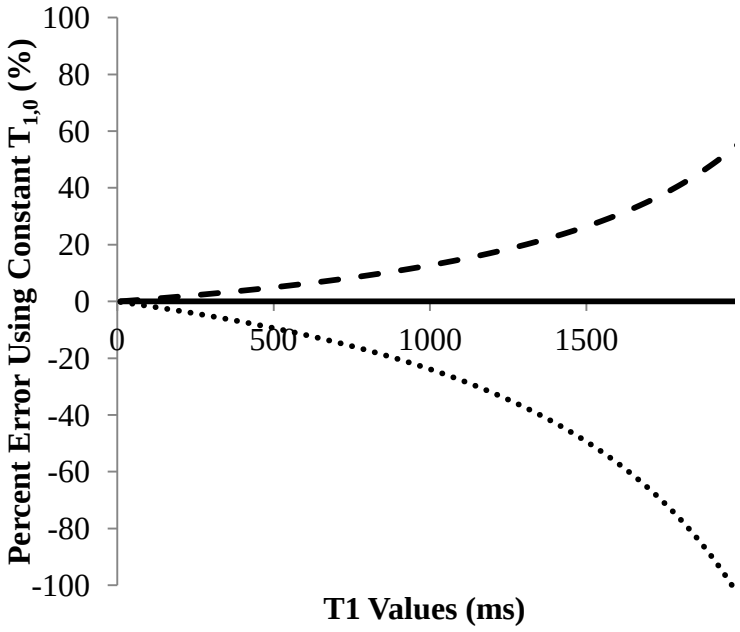

Figure 3.6: Estimation of percent difference from concentrations calculated with an isotropic $T_{1,0}$=2817 ms (mean, solid line), 3669 ms (upper limit, dashed line), and 1965 ms (lower limit, dotted line).

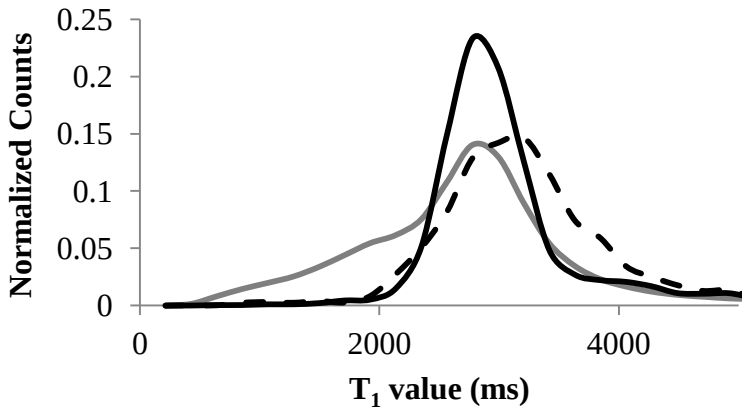

Figure 3.7: Histograms of the total image (solid grey line), the muscle tissue (solid black line), and the bone (dashed black line) in a pre-contrast T_1 map.

3.3.5 How does the Isotropic $T_{1,0}$ Method Compare to Other Methods?

Next this group compare and contrast results when a single isotropic value of $T_{1,0}$ is used (as described above) versus when $T_{1,0}$ values are taken from image volumes of the tissue prior to addition of contrast agent. Images of a pre-contrast and post contrast FTMB procedure are shown in figure 3.8. Figure 3.8a (left) shows a pre-contrast image that has not been altered, figure 3.8b (left) shows the same image but registered to the post-contrast image using an affine registration (rigid body registration); figure 3.8c (left) shows the same image but registered to the post-contrast image using a deformation registration; and, finally, figure 3.8d (left) shows the isotropic $T_{1,0}$ method in which a single value of $T_{1,0}$ is applied to all of the pixels in the region of interest. It is apparent in figure 3.8a-c (right) that the edges of the legs do not perfectly overlap (large red region in concentration map) in the unregistered, affine registered, or deformation registered images; but the isotropic $T_{1,0}$ concentration map (Fig 3.8d, right) does not have significant patches of red surrounding the leg indicating that this is not a problem for the

isotropic $T_{1,0}$ method. The rigid body transformation (Fig 3.8b) was performed by choosing points on the femur, which is a rigid anatomical feature. While the transformation worked well for the femur, the surrounding soft tissue is not registered using an affine technique. The registration with deformation was applied to register the soft tissue (Fig 3.8c); however, several factors made the registration with deformation method less capable of describing the transform well. It was difficult to identify landmarks to register by in the muscle tissue and especially the fat marrow tissue. Furthermore, choosing the number of corresponding points necessary to obtain a better transform in 3D would be impractically time consuming (250 points takes ~4 hours). Even though the registration with deformation was not perfect, it seems to perform better than the isotropic $T_{1,0}$ method for some anatomic features having $T_{1,0}$ values different from the tissue mean. For example, in Figure 8d (right), fairly thick features appearing to have non-zero contrast agent concentration appear. These features also appear in the registered concentration maps (Fig 8b, right, and 8c, right), but the features are generally fewer and thinner. This indicates that, for anatomical locations such as the brain, which is less isotropic than the muscle, registration may be more necessary and practical. The brain is simpler to register because of lack of deformation and multiple landmarks to register by. There are many groups working on performing and automating registration techniques that could be useful if registration were required [65,109-113]. Regardless of the strengths and weaknesses of each method, within the region likely containing contrast agent (bottom left corner of the leg), all four methods seem to perform well, and no major differences are noted among the methods. There are slight differences in the concentrations calculated in the isotropic $T_{1,0}$ method near the edge of the leg; however,

these differences are not likely to affect conclusions drawn from these data since animal-to-animal variability is likely greater than error due to the value of $T_{1,0}$ used. It should be noted that even though the registration and isotropic $T_{1,0}$ methods give similar results for this application, the isotropic $T_{1,0}$ method is far less time consuming and has the practical benefit of not requiring a pre-contrast image (which requires that the animal be scanned, removed from the scanner, and then implanted with the local drug delivery vehicle). For applications where the pre-contrast and post contrast image could be obtained without removing the subject from the MRI, such as when the contrast or delivery vehicle is injected, the pre-contrast image could easily be used for $T_{1,0}$ without needing to perform a registration. Therefore, the practicality of a method for a specific anatomical region and the expected performance of a method for that anatomical region should be considered when choosing whether to use a registration technique or an isotropic $T_{1,0}$ method.

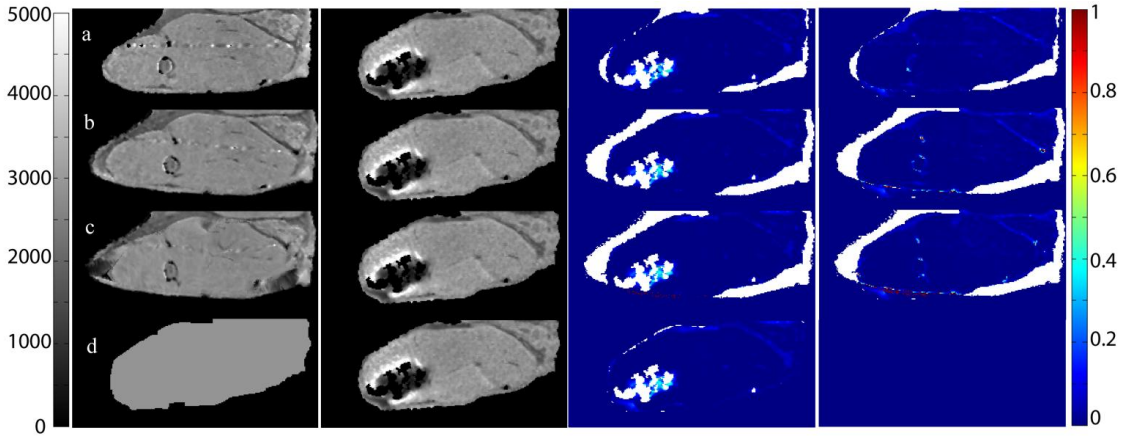

Figure 3.8: (a) The unregistered images, (b) affine registered images (performed by Jonathan Plasencia), (c) registration with deformation (performed by Jonathan Plasencia), (d) constant $T_{1,0}$, where the left image is $T_{1,0}$, middle left image is T_1, and middle right image is the concentration map resulting from those $T_{1,0}$ and T_1 images, where white is

where the calculated region of cement is, and the right image is the difference between a-c and d.

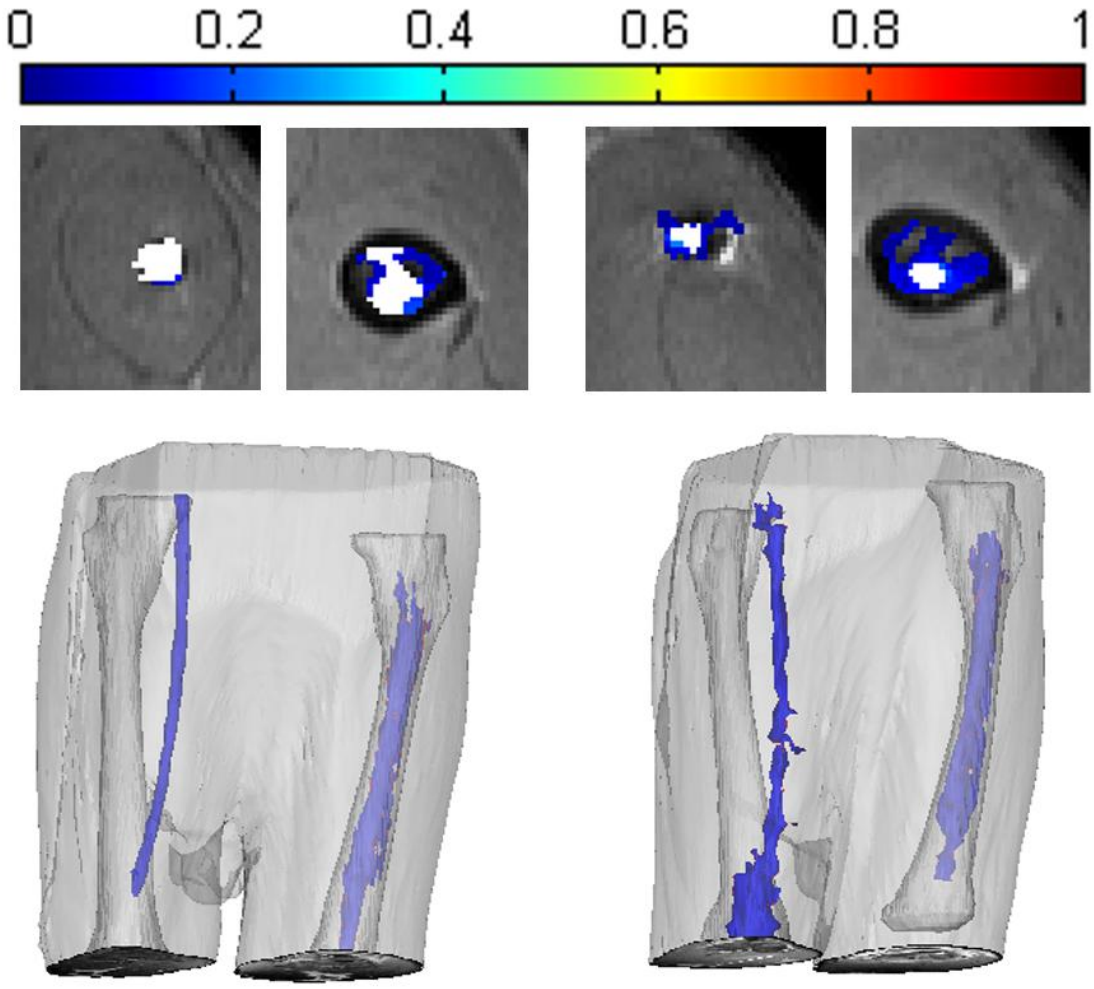

Figure 3.9: A comparison of concentration maps and 3D Mimics reconstructions of an IMR and IOR without (left) and with (right) contrast agent mixed into the ALBC.

3.3.6 What Practical Information can this Method Provide?

Figure 3.9 show concentration maps and 3D reconstructions for an IMR and IOR of the control and experimental cement composition. Visual examination of the sagittal

concentration maps from the data set show contrast above and below the IMR. The isotropic $T_{1,0}$ contrast concentration calculation method calculates a significant difference in volume of distribution between control and experimental animals with an IMR ($p<0.0001$) (Fig 3.9); however, calculated no significant difference between control and experimental IOR ($p\approx0.5$). When the same implants were compared with total mass of contrast agent observed as the metric, again the IMR showed significance ($p\approx0.004$) and the IOR showed no significance ($p\approx0.8$). One limiting factor for calculating contrast concentration within the intramedullary space is the multiple tissue types present in the surrounding area. In this work concentration calculations were restricted to only the intramedullary space, but contrast could easily be present in the bone surrounding the intramedullary space as well as proximally and distally. By excluding these other regions the contrast calculations are restricted to a uniform volume, making the difference in volume of distribution very difficult to calculate. The results could possibly be improved if all the tissue types in that leg (muscle, several types of bone, and intramedullary space) were accounted for but this is difficult and time consuming to accomplish.

2.4 Conclusions

This chapter demonstrates a simple to use method for imaging local drug delivery and calculating its local concentration with good spatial and temporal resolution. This method has broad applications in the field of drug delivery, but here is shown applied to delivery from ALBC for the treatment and prevention of infection in orthopaedic applications. This group identify and quantify sources of error in this method and suggest ways to minimize these errors. Specifically, this group discuss how to generate images

with T_1 values in the range that will yield accurate concentrations and avoid artifacts from excessive concentration of contrast agent, the strengths and weaknesses of several methods of generating $T_{1,0}$ values for use in converting from T1 to concentration, and methods for using these data to statistically compare contrast agent distributions between wound models.

Chapter 4. DISTRIBUTION PATTERNS OF LOCAL DRUG DELIVERY IN ORTHOPAEDIC WOUNDS USING MRI

4.1 Introduction

Orthopaedic infection is a serious problem affecting many patients' physical and financial wellbeing. Infections of orthopaedic implants, and surrounding bone and joints, can result in increased pain, loss of function and productivity. Approximately 1-2 % of primary arthroplasties result in a surgical site infection [11,12]. In trauma cases the rate of infection is 9.4% [13]. There is an estimated 112,000 total orthopaedic infections per year [16], a figure expected to increase as the projected number of arthroplasties increase by several fold over the next 18 years [18]. Each infection results in a $15,000-250,000 increase in healthcare cost [16,17]. It was estimated a total of $1.8 billion was spent on increased medical costs due to orthopaedic infection of total joint arthroplasties in the US in 2004 [16], and is likely more every year.

Orthopedic infection is a complex problem because they are the result of biofilm forming microbes, such as *Staphylococcus aureus*. Not only do biofilms cause a barrier to antimicrobial transport, microbes in established biofilms are less susceptible to antimicrobials [22]. Therefore, antimicrobial concentrations 100-1000x minimum inhibitory concentration (MIC) are required to kill organisms in biofilm [25,26]. Since antimicrobial action is time and concentration dependent, these high concentrations need to persist to be effective. For instance, biofilm methacillin-resistant *Staphylococcus aureus* takes more than 5 days of exposure to 2 mg/mL Vancomycin to be eradicated [29].

Clinically, orthopedic infections are often caused by implanted devices, but can involve the surrounding bone and joints. Therefore, removal of the implant followed by a 2 stage plan resection of dead and dysvascular tissue is necessary. Dead space is managed by filling the volume with antimicrobial loaded bone cement (ABLC). The ABLC is intended to treat any biofilm fragments left during debridement as well as any planktonic bacteria in the surrounding muscle substance. Since microbes thrive on implant surfaces the treatment of infection requires a period of delay during local antimicrobial delivery, before reconstruction and re-implantation can occur. Treatment often fails because of longer operations or incomplete debridement performed by less practiced surgeons. To be effective, locally delivered antimicrobials should cover the entire volume of the surgical wound, where biofilm debris might be present after the surgery, as well as penetrate into the surrounding muscle to manage any incomplete resection.

There is a long history of *in vitro* research focused on elution kinetics of antimicrobial loaded bone cement of varying compositions [9,46-49]. These experiments are usually performed in near infinite sink condition, where standardized specimens are kept in relatively large volumes of well mixed aqueous fluid at 37 $^{\circ}$C [46,47]. Since elution of drugs from biomaterials is surface area and volume dependent, having known shapes and external conditions allows researchers to calculate transport properties of the material. Elution studies give valuable information for comparing different vehicles in similar environments, but is less useful for predicting *in vivo* behavior. *In vivo* there are complex environments that effect not only where antimicrobials distribute to, but how they are delivered. For instance, bone is a barrier to antimicrobial transport. The effective diffusion coefficient in bone ($D_{eff}=7.8\times10^{-7}$ cm^2/s) [51] is much lower than in muscle

($D=1.38x10^{-5}$ cm^2/s) [52]. When antimicrobial loaded cement is in bone there will be an accumulation of antimicrobial between the bone and the cement. The accumulation will decrease the driving factor for antimicrobial delivery from the cement and delivery from the cement will decrease. Therefore, *in vitro* testing cannot predict *in vivo* concentration over time and location.

To gather information on the *in vivo* behavior there have been some research collecting fluid samples and biopsies [1,2,53]. While these methods give more information about how antimicrobials deliver from cement *in vivo*, they can only capture the concentration of antimicrobial in the sample location at the timepoint the sample was taken. Cierney *et al.* studied *in vivo* patient outcomes to determine treatment efficacy, but clinical outcomes do not provide information on the mechanism behind treatment success [58].

Medical imaging has been used to visualize drug distribution *in vivo* in real time. Magnetic resonance imaging (MRI) has been used to study the distribution of contrast agents locally delivered from catheters to glioblastomas [75,76]. The distribution of contrast agent from an ocular implant has been reported [87]. Previous work by McLaren, Caplan, and co-workers found locally delivered Gd-DTPA could be seen on MRI and was affected by delivery vehicle type and location [99]. In that experiment a common, clinically used, MRI contrast agent gadolinium diethylenetriaminepentaacetate (Gd-DTPA) was used as a surrogate for antimicrobials.

Gd-DTPA is a fairly accurate model for antimicrobials because it has a similar solubility and diffusion coefficient ($D=4.0 \times 10^{-6}$ cm^2/s) [89] to the antibiotics Gentamicin ($D= 2.1 \times 10^{-6}$ cm^2/s)[23] and Vancomycin ($D= 3.6 \times 10^{-6}$ cm^2/s) [90]. Gd-DTPA affects the

motion of water molecules, causing their longitudinal relaxation to decrease. Like all MRI contrast agents Gd-DTPA is only visible in areas that are hydrated. Areas of low hydration, such as inside bone and bone cement will not show Gd-DTPA.

In this chapter Gd-DTPA distribution is imaged distributing from bone cement into orthopaedic wound models. The research questions for this study are: is distribution of contrast agent following local delivery detectable on MRI? Can contrast concentration be quantified on MRI? Does surgical wound environment affect distribution of contrast following local delivery?

This research was conducted as a collaboration between Morgan Giers, Alex McLaren, Kenneth Schmidt, Michael Caplan, and Ryan McLemore.. Specific contributions of each team member are stated in the corresponding sections in the methods; however it should be additionally noted that Morgan Giers, Alex McLaren, Michael Caplan, and Ryan McLemore participated in analyzing and interpreting the data.

4.2 Methods:

4.2.1 Delivery Vehicle Fabrication

Local delivery depots were created by Morgan Giers, Ryan McLemore, and Alex McLaren using Simplex P® (Stryker, Kalamazoo, MI, USA) PMMA bone cement. The control vehicles were made using the manufacturer's instructions (67wt% PMMA and 33wt% MMA) and included no contrast agent or porogen. The experimental implants were made using 57wt% PMMA, 29wt% MMA, 3wt% Gd-DTPA, and 11wt% 250-425 μm diameter xylitol as a porogen. 1 cm x 3 mm diameter rods were fabricated prior to

implantation using a red rubber catheter as a mold (Covidien, Mansfield, MA,USA). The delivery vehicles that were used to fill wound dead space were fabricated intra-operatively.

4.2.2 Surgical Procedure

Two different wound models were created by Alex McLaren and Kenneth Schmidt using female New Zealand White rabbits. For the full thickness muscle and bone removal wound (FTMB), a full thickness of muscle and part of the cortex of the femur was removed. Specifically, a 4 cm incision was made in the ventral thigh of the animal. A 1 cm x 1cm portion of muscle was removed all the way to the bone, 1.1±0.3 g of tissue, with a lexelle ronjeur. Then, a 1cm x 4 mm window was made in the cortex of the femur using a drill with a 6 mm acorn burr. Two cement rods, 4 mm in diameter and 4.5 cm long, molded with a slight curve to mimic the curvature of the femur, were inserted in either direction from the window into the intramedullary canal. An additional 1.5 ml of cement was used to fill the inside of the femur exposed from the window as well as the void space of the removed muscle. The portion of cement used to fill the void space of the removed muscle was formed into a rectangular shape. The muscle and fascia lata were left open and only the skin was closed. 10 rabbit legs total were given FTMB wounds, with 6 legs receiving experimental delivery vehicles and 4 receiving control vehicles. For the partial muscle removal wound (PTM), a partial thickness of muscle was removed and the femur was left intact. In the second model only the deep half the thickness of the muscle was removed and there was no bone removal. The mass of the muscle removed was 0.6±0.1 g. In the PTM model 1 ml of cement was used to fill the

removed muscle space. The muscle was closed over the implant, as well as the superficial layers. 8 rabbit legs total were given PTM wounds, with 6 legs receiving experimental delivery vehicles and 2 receiving control vehicles.

4.2.3 Image Acquisition

All images were taken by Qingwei Lui with a Bruker Biospin® 7-T MRI (Bruker Biospin, Billerica, MA, USA). T_1 weighted, rapid acquisition with relaxation enhancement (RARE), images were collected of the upper legs, knee to hip, of the rabbits. Each of these T_1 weighted images consisted of 42 fat-suppressed coronal slices, 2mm thick, with voxel sizes of 0.3 mm x 0.3 mm x 2 mm. A series of these T_1 weighted MRI images at different repetition times (TRs) (1463, 2000, 3000, and 5000 ms) were obtained 5.5 hours after implantation of the cement. T_1 maps were obtained from the T_1 weighted image series by fitting them to the Bloch equation [63], using Bruker software.

4.2.4 Euthanasia

At the conclusion of imaging, animals were euthanized with 120 mg/kg Beuthanasia D solution. All procedures were compliant with the National institute of Health guidelines for the care and use of laboratory animals and approved by the Institutional Animal Care and Use Committee (IACUC).

4.2.5 Image Processing

All image processing was performed by Morgan Giers with significant input from David Frakes, Ryan McLemore, and Michael Caplan. Filtering and masking of MRI

images was done using MATLAB (The Mathworks, Inc., Natick, MA, USA). The T_1 maps were filtered with a 5th order median filter to reduce the noise. The filter changes a pixel to the median value of a group of pixels including itself and the 4 pixels surrounding it. The T_1 maps were also masked with a binary mask of the T_1 weighted image, which was less noisy than the T_1 map, to remove all noise from outside the leg area.

The segmentation of the region of contrast was completed using Mimics (Materialise, Leuven, Belgium). The cleaned T_1 map was thresholded at a T_1 value of 2200 ms. The area of contrast, as determined by an observer, was then selected from the thresholded image. Small areas of contrast, less than 100 pixels, not connected to the main body of the contrast were excluded. The segmented area containing drug was used to construct a 3 dimensional representation of the drug distribution. The femur and legs were segmented in Mimics using the T_1 weighted image to provide anatomical references. The rectus femoris muscle was segmented in Mimics using a built in user guided gradient edge detection algorithm. The mask was smoothed using a 0.8 smoothing factor with 2 iterations. The smoothed mask was corrected manually.

The segmented areas were then imported back into MATLAB to construct concentration maps. The area of contrast was transformed into approximate contrast concentrations using the equation $\frac{1}{T_1} = \frac{1}{T_{1,0}} + r_1 C$ [80,114], where T_1 was the T_1 map value, $T_{1,0}$ was the pre-contrast T_1 value, r_1 was the relaxivity constant, and C was the concentration. The $T_{1,0}$ value used was the mean histogram value from 5 pre-contrast images. The area where the T_1 value was na was made red, the greatest value in the concentration map. The area where T_1=na included bone cement and the region where the

signal was saturated by high concentrations of drug. The concentration map and saturated region were superimposed on the T_1 weighted image.

4.2.6 Statistics

Volume of distribution was calculated for the extrafemoral space by Morgan Giers, included all contrast agent and cement implant outside the femur. Only the extrafemoral space was calculated because the volume of cement was equal between wound types outside of the femur. General linear form ANOVAs were performed in Minitab (Minitab Inc., State College, PA) for all volumes vs. wound model type and side to compare control to experimental implants. General linear form ANOVAs were performed by Ryan McLemore and Morgan Giers for experimental implant volumes vs. model type and side to compare the two experimental implants. All data used in ANOVA were confirmed to have a normal distribution through examination of the histogram of residuals and the normal probability plot. Post-HOC t-tests were used for any significant findings from the ANOVA. The accuracy of the ANOVA's were verified using the R^2 values.

4.3 Results

4.3.1 Can It be Seen?

The unmodified T_1 weighted MRI images are high resolution images with little noise (Fig 4.1a). Small anatomical features including the skin are clearly visible. Bone cement appears dark, and is visible as a region extending from the femur to the skin of the top leg (Fig 4.1a). Contrast is visible as bright pixels surrounding the cement region.

The unmodified T_1 maps, which give the T_1 relaxation times as calculated from several T_1 weighted images, are high resolution images with a large amount of noise (Fig 4.1b). Both contrast and bone cement are visible as a dark region. The filtered and masked T_1 maps have less noise in the legs and practically no noise outside the legs (Fig 4.1c). The level of 2200 ms was chosen for the thresholded image because it included all visible contrast as determined by a group of experts. To remove artifacts the contrast was segmented from the thresholded image (Fig 4.1d). To accomplish the segmentation all contrast in the muscle and femur was segmented. Then, all pixels connected to the implant within that region were segmented. The concentration calculation produces a map where the majority of concentration values are in the 14-100 μg/mL range (Fig 4.1e). When the segmented region includes a T_1 value of na is plotted red (Fig 4.1f). The red region includes both cement and artifact where contrast concentrations are too high to distinguish from cement. The 3d reconstruction shows a rough edged volume containing contrast and cement (F4.ig 1g). The 3d reconstruction shows distinctive patterns, such as contrast distributing under the skin.

There is a statistically significant difference in volume of distribution between images with contrast (2674 ± 1140 mm^3) and images without contrast (956 ± 813 mm^3) ($p<0.001$), indicating contrast is agent is readily visible.

4.3.2 Can Concentration be Measured?

Concentration maps show profiles consistent with known transport phenomena. It is expected that concentrations should be highest near the implant and lower farther from the implant (Fig 4.2). This concentration profile is seen consistently in all non control

images. Two discrete regions are analyzed at 5.5 hours (Fig 4.3). Region 1 (furthest from the femur) has a measured concentration of 34±39 µg/mL. Region 2 has a measured concentration of 133±63 µg/mL. These two concentrations are statistically different ($p<0.001$, t-test).

4.3.3 Does Surgical Wound Environment Affect the Distribution of Locally Delivered Gd-DTPA (Antimicrobial Surrogate) ?

Some commonalities are apparent in distribution pattern between the two surgical wound types. In both surgical models some penetration into muscle tissue is visible, but there is considerable preference to movement along intramuscular septa and connective tissue. There was an also observed difference in the distribution pattern of agent between the two types of wounds (Fig4.4-4.5). When muscle and fascia were left open in the FTMB wound, drug is observed throughout the damaged muscle layer, and can be observed to distribute under the skin (Fig 4.2 d-f, Fig 4.5). The volumes of the distributions between the PTM (1940 $mm^3 \pm$ 771 mm^3) and FTMB (2422 $mm^3 \pm$ 981 mm^3) wounds however where not statistically different ($p=0.3$)

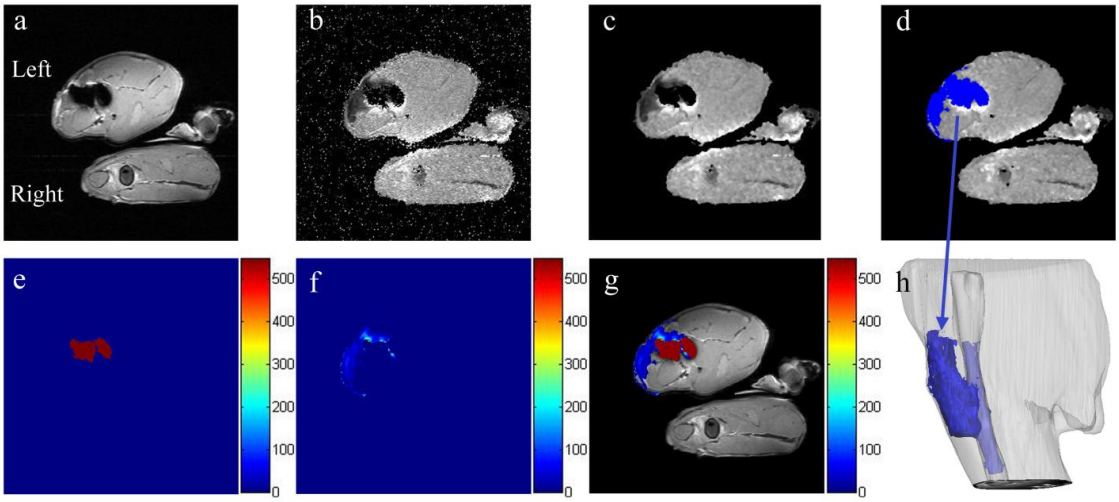

Figure 4.10: Schematic of how concentration maps are made. (a) T_1 weighted image (b) T_1 map (c) filtered and masked T_1 map (d) segmentation (e) concentration map (f) region where the T_1 value equals 0 (g) superimposed concentration map and T_1 equal to zero region on a T_1 weighted image (h) 3D reconstruction of the segmented region.

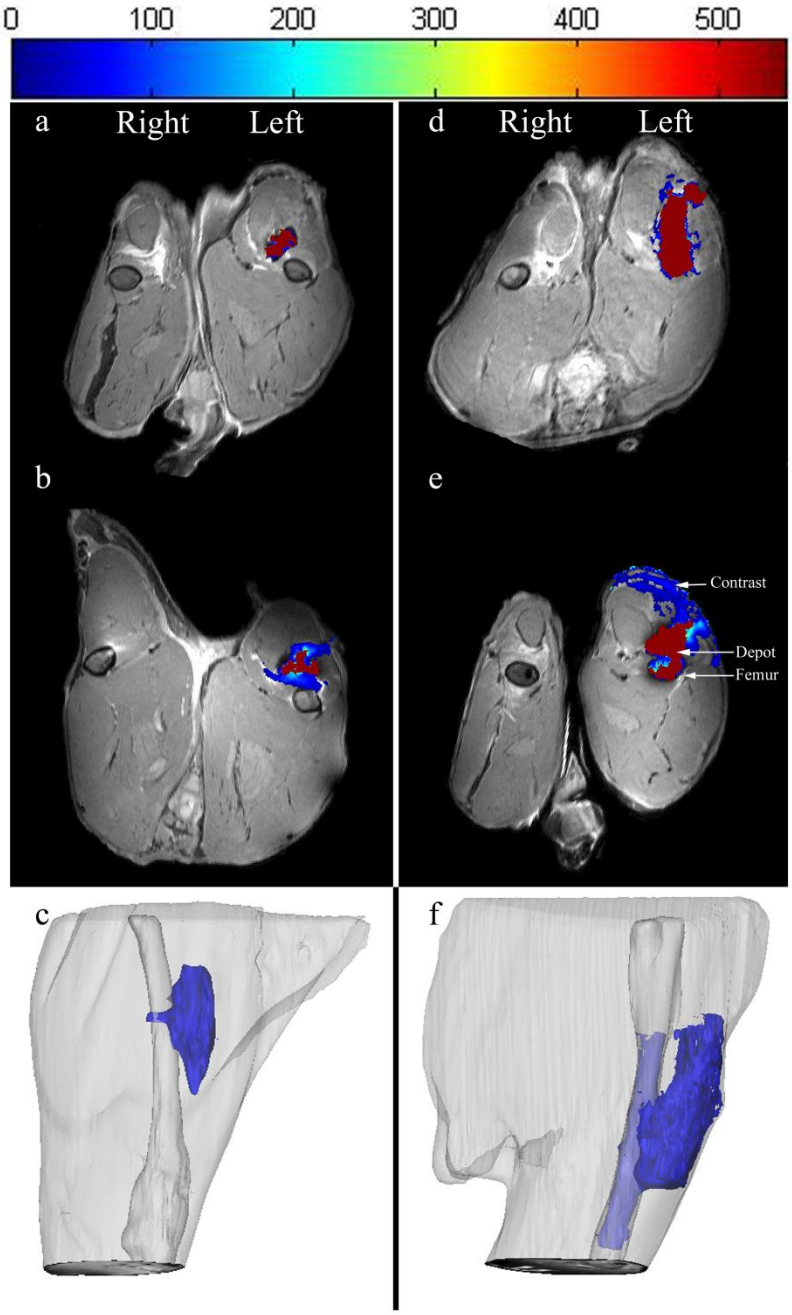

Figure 4.2: (a) and (b) are coronal concentration maps from PTM wounds at 5.5 hours, (c) is a Mimics® 3D reconstruction of (b). (a) is a control depot and (b) is a Gd-DTPA depot . (d) and (e) are coronal concentration maps from FTMB wounds at 5.5 hours, (f) is a Mimics® 3D reconstruction of (e). d) is a control depot and (e) is a Gd-DTPA depot . The color gradient bar at the top represents the Gd-DTPA concentration. Dark blue is low concentration, red is high concentration or signal saturation.

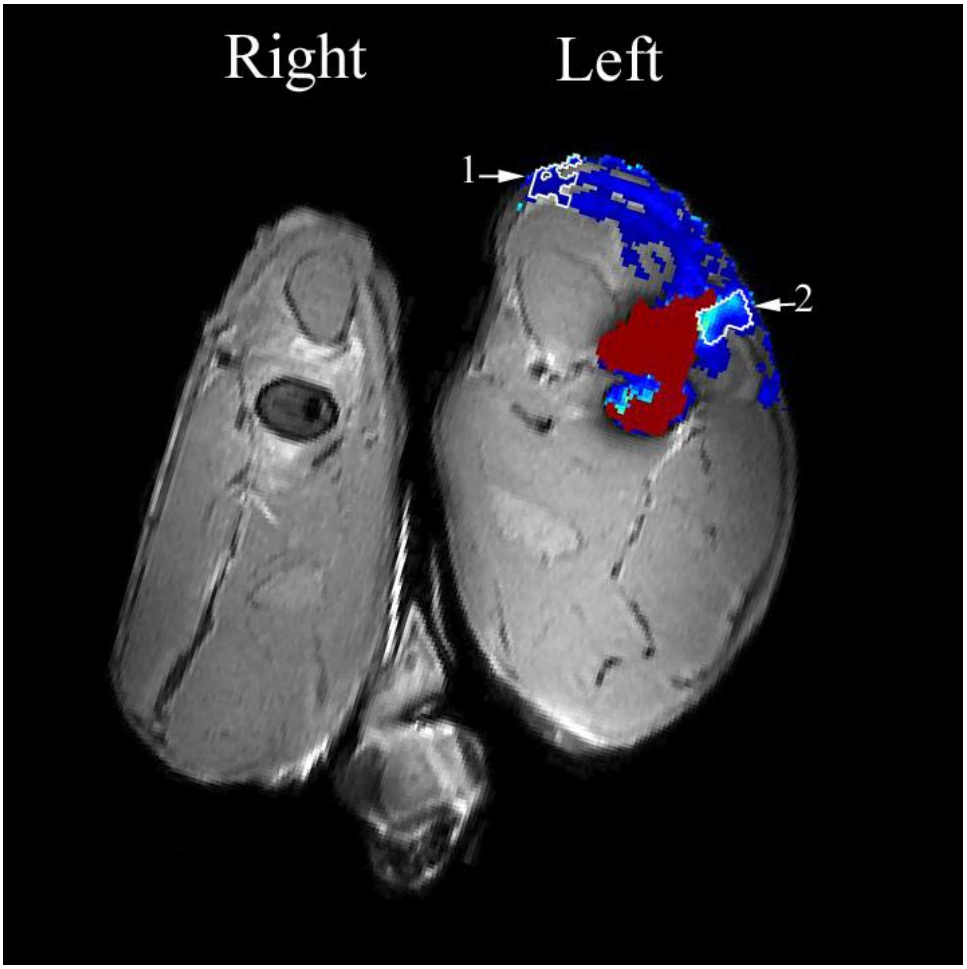

Figure 4.3: Region selection from a single slice FTMB model at 5.5 hours. Selected slice is diaphyseal, near the middle of the femur. Selected regions are indicated with white outlines. Region 1 has a measured concentration of 34±39 μg/mL. Region 2 has a measured concentration of 133±63 μg/mL.

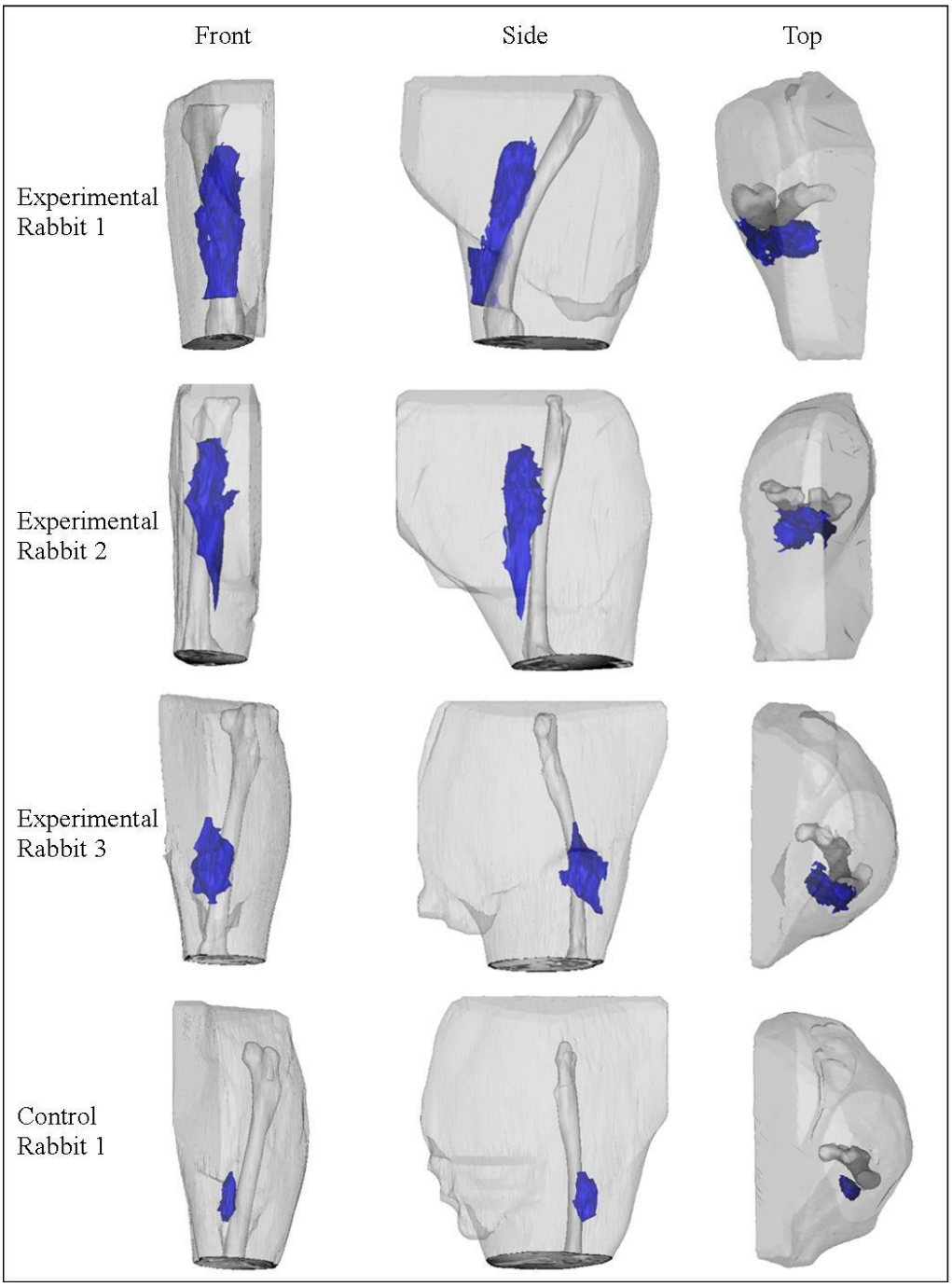

Figure 4.4: 3 angles of a Mimics® 3D reconstruction of a partial thickness muscle removal surgical model with contrast (experimental rabbits 1-3) and without contrast (control rabbit 1).

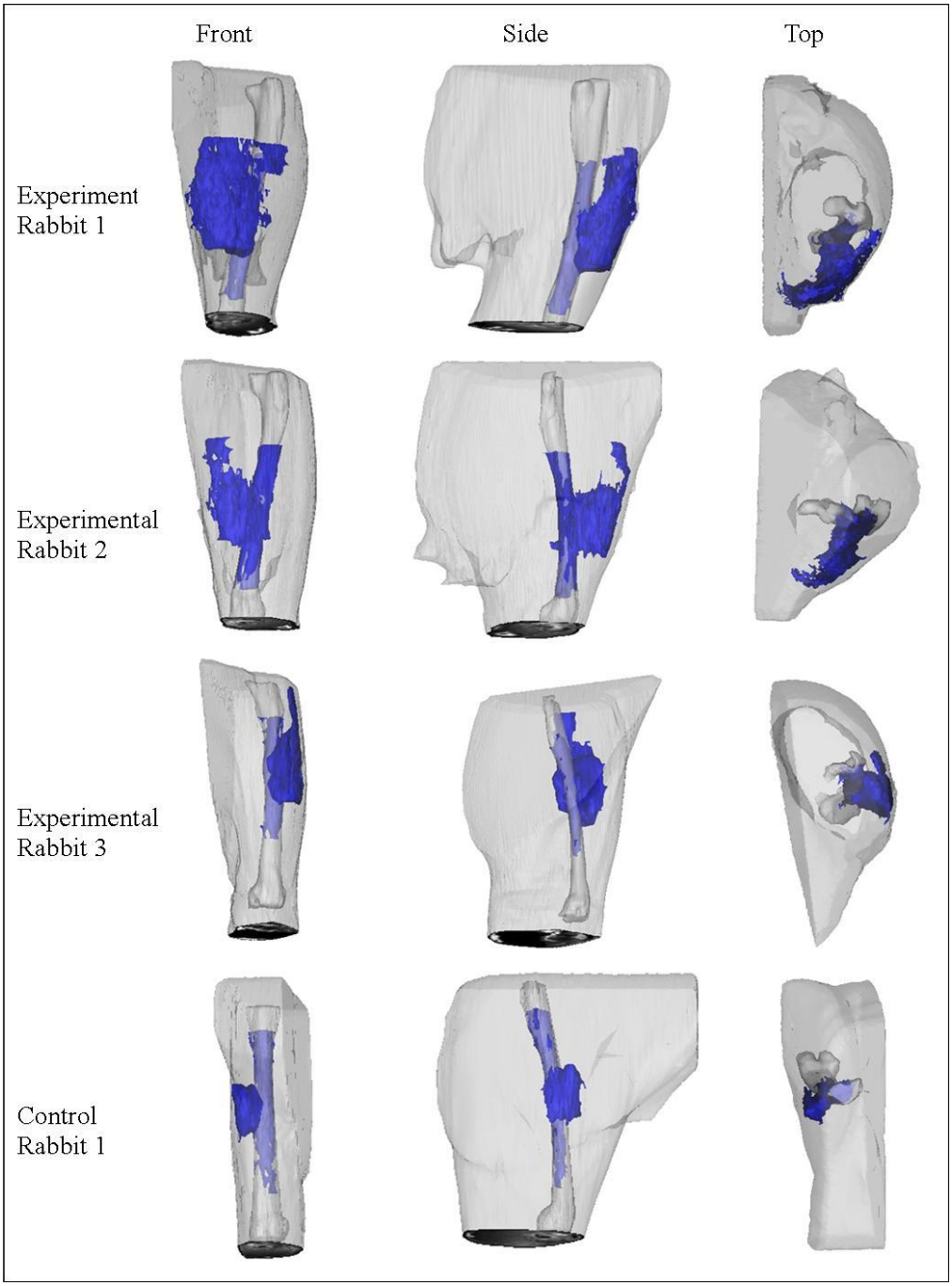

Figure 4.5: 3 angles of a Mimics® 3D reconstruction of a full thickness muscle and bone removal surgical model with contrast (experimental rabbits 1-3) and without contrast (control rabbit 1).

4.4 Discussion

Compared to previous methods[1,115] MRI visualization gives more detail and is less invasive to human patients. Since the images show an anisotropic distribution, using a biopsy or fluid collection method gives results dependent on the location the sample was collected from. For instance, in studies where wound fluid is collected [1], the concentrations might be higher than the concentrations achieved in nearby muscle. Visualizing drug distribution using MRI could be used in human patients, individually, in real time to observe if the treatment is likely to be effective.

There are several limitations of this study. The first limitation of this study was the short, 5.5 hour, period of time data was collected, compared to the ~28 days of expected delivery [2]. This experiment was meant to visualize the differences between wounds and not the time course of delivery. Second, rabbit anatomy is different from human anatomy. Rabbits have very loose connective tissue between muscle groups and they have a tendency to pull apart, creating a space between the muscles. Rabbits also lack the subcutaneous fat that most humans have. The difference in anatomy might result in exaggerated anisotropy of distribution of contrast in the rabbit model because of the extra space between muscles. Third, Gd-DTPA is not an active antimicrobial agent. Their transport properties based on solubility and diffusion coefficients are theoretically very similar in the tissue, but the antimicrobial could bind or get intracellularized while Gd-DTPA does not. Further work is needed to determine if any factors would cause Gd-DTPA and antimicrobials to distribute differently. Finally, the cut tissue from the surgery cause the presence of methemaglobin, which shows up bright in the T_1 weighted image

and is indistinguishable from the contrast agent [116]. The methemaglobin problem is mostly resolved in the T_1 map, where the methemaglobin is much less sensitive than the contrast agent.

Even with the limitation of this work there are clear differences between the distributions in images with contrast and images without contrast. The visible and statistical differences show that MRI is a reliable method for detecting distribution of contrast agents from local delivery depots.

While locally delivered Gd-DTPA concentrations can be quantified on MRI, there are several assumptions necessary to make this calculation. These assumptions can introduce error into the calculation. This group has estimated these errors and discussed them at length in a chapter 3 [105]. Briefly, $T_{1,0}$ was used in place of a perfectly registered pre-contrast image, so that a pre-contrast image is not necessary, hence making MRI visualization of drug distribution more clinically viable. The $T_{1,0}$ used here was a mean value from the histograms of 5 pre-contrast rabbits. The standard deviation of those histograms was used to determine a theoretical error in the concentrations calculated. The standard deviation was used instead of a confidence interval because the standard deviation was larger and hence a more conservative number. Using this technique the sensitivity limit was calculated as 14 µg/mL and produced concentration estimates of 0 to 26 µg/mL. The error decreases as the concentration increases. Overall, it was shown that the error was not so large that practical differences in animal experiments could not be seen. Clinically, therapeutic ranges for treatment of biofilm associated infections is 100-1000's of µg/mL [25]. Therefore, if antimicrobial surrogate is visible on the MRI it is likely

at a therapeutic level. If antimicrobial surrogate is present at a sub-visible concentration it is likely not at a therapeutic level and is irrelevant to the purpose of this experiment.

There are differences seen qualitatively in the distribution locations between the two types of wounds. Small closures in tissues such as fascia lata are a significant barrier to transport. These distributions, however, do not have statistically significant different volumes. Both wounds also have the commonality that contrast remains within a few centimeters of the wound site and does not cover the entire leg. Most of the contrast agent is seen in the wound site and intermuscular tissue planes. It is unknown if these differences will scale to human subjects or larger animals, based on the differences between human and rabbit anatomy. It is seen that there is a large variability between animals with the same wound type. The variability indicates that distributions clinically could vary widely between patients. MRI could potentially be used as a tool to assess the concentrations achieved in an individual patient after surgical intervention.

4.5 Conclusions

In conclusion, the use of MRI gives more information than previous methods to determine *in vivo* distributions of contrast from local delivery vehicles. This method is applicable to human patients and could potentially be used clinically to confirm it treatment was likely to work.

Chapter 5. DEVELOPMENT AND CHARACTERIZATION OF MRI VISIBLE ANTIMICROBIALS

5.1 Introduction

In chapters 2-4 a method was outlined for how MRI imaging of contrast agent distribution from bone cement can be used to acquire the spatiotemporal distribution of drugs *in vivo*. That work is performed to assess how antimicrobials might distribute in surgical wounds to treat orthopaedic infection. In order to further study this problem it is desirable to use a molecule that has therapeutic ability, but can be seen on MRI. Such a molecule would potentially serve as a better model for studying antimicrobial distributions in orthopaedic infections because if it maintained biological activity it would have the same binding properties of an antimicrobial, where Gd-DTPA alone does not. In this work conjugation of two different antimicrobials, gentamicin and vancomycin, to MRI contrast agents will be attempted. Both of these antibiotics are commonly used in orthopaedic surgery. Gentamicin is primarily used for gram-negative bacteria, but shows bactericidal effects for some gram-positive bacteria as well (Fig 5.1b). It acts by binding and repressing ribosomal activity. Vancomycin is only active against gram-positive bacteria (Fig 5.1c). It acts by binding the peptidoglycan layer of the cell wall and preventing transglycosylating crosslinking.

The antibiotics will be bound to 1,4,7,10-tetraazacyclododecane-1,4,7,10-tetraacetic acid (DOTA), a chelator, and then use the DOTA to chelate Gd^{3+} ions. In order to bind these antibiotics to DOTA an aqueous 1-Ethyl-3-(3-dimethylaminopropyl)carbodiimide (EDC) reaction will be used [117-121]. In an EDC

mediated reaction a molecule with a carboxylic acid, in this case DOTA has 4 carboxylic acids, binds with EDC to form an unstable O-acylisourea intermediate. When N-Hydroxysulfosuccinimide (Sulfo-NHS) is introduced it replaces the EDC and forms a semi-stable NHS-ester bond with DOTA. The Sulfo-NHS is then replaced by a molecule with a primary amine; gentamicin has 3 primary amines and vancomycin has 2. The replacement of Sulfo-NHS by an antibiotic forms an amide bond between the DOTA and antibiotic. The DOTA can be used to chelate free gadolinium ions, making the molecule potentially MR visible. M Lewis *et al.* successfully used EDC/Sulfo-NHS chemistry to conjugate proteins with primary amines and DOTA [118,119]. Prodhomme *et al.* successfully conjugated a poly glutamic acid polymer to vancomycin using an EDC mediated reaction and found it maintained bactericidal activity [122]. J Lewis *et al.* conjugated antibodies to gentamicin using an EDC reaction and found that gentamicin also maintained its biological activity when bound [123].

This research was conducted as a collaboration between Morgan Giers, Alex McLaren, Ryan McLemore, and Michael Caplan.

5.2 Methods:

5.2.1 Conjugate Preparation

Conjugation protocol is developed by Morgan Giers and Ryan McLemore with input from Veronica Clavijo Jordan and Derek Overstreet. Conjugates were prepared by Morgan Giers, Ethan Province, Adam Roussas, and Mathew McDermand. Conjugates are prepared using a two step Sulfo-NHS and EDC mediated primary amine to carboxylic

acid reaction. In the first step molar ratios of 1:4:4 of DOTA:EDC:Sulfo-NHS respectively are added to a 0.1 mM MES buffer at 4ºC and the pH is adjusted to 5.5. The reaction is allowed to stir for 30 minutes. After that initial 30 minutes gentamicin or vancomycin is added to the reaction in a 1:1 molar ratio with DOTA and the pH is adjusted to 7.4. The reaction was allowed to stir for 24 hours.

After the antimicrobial to DOTA conjugate is prepared it is used to chelate gadolinium. Chelation is done by adding 0.95:1 molar GdCl3 to DOTA and adjusting the pH to 6.5 using 0.1N HCl. The reaction is heated to 85-95ºC and stirred for 30 minutes. In both steps phosphate buffers are avoided because it can deactivate EDC [124] and bind with gadolinium ions forming insoluble precipitates [125].

5.2.2 High Pressure Liquid Chromatography

Analytical high pressure liquid chromatography (HPLC) is performed to separate the molecules and determine yield. The following procedures were developed and performed by Morgan Giers and Ethan Province. The mobile phase for the gentamicin conjugate is 30% methanol and 70% water. The column used is a 4mmx25 cm 5um normal phase column. The conjugate is run isocratically for 30 minutes. Elution was monitored with absorbance at 254 nm. The mobile phase for the vancomycin conjugate starts at 10% acetonitrile and 90% water, then, steadily over 15 minutes raises to 70% acetonitrile and 30% water. The column used is a 4mmx25 cm 5um Agilent C18 column. Elution is monitored with absorbance at 254 nm.

5.2.5 Mass Spectrometry

Matrix-assisted laser desorption/ionization-time of flight (MALDI-TOF) mass spectrometry is performed by Morgan Giers, Adam Roussas, and Mathew McDermand to determine molecular weights of the product. All mass spectrometry for the gentamicin conjugate is performed in a 4-Hydroxybenzylidenemalonitrile (4-OH) matrix. All mass spectrometry for the vancomycin conjugate is performed in a 2,5-Dihydroxybenzoic acid (DHB) matrix.

5.2.5 Xylenol Orange Assay

A xylenol orange assay is performed by Morgan Giers and Adam Roussas with input from Ryan McLemore to determine the amount of unchelated Gd^{3+} ions left after the chelation step. Xylenol orange is a colorimetric assay where the dye appears purple when bound with Gd^{3+} and yellow when unbound [126]. More specifically xylenol orange is a weak chelator with four carboxilic acid groups. When the molecule loses H molecules, such as in the chelation of a metal ion or alternatively when in a high pH solution, it turns from yellow to purple. The xylenol orange assay is performed by creating a standardized curve using molar ratios of xylenol orange to GdCl3 of 1, 0.5,0.1,0.05, and 0.01. The post chelation reaction with 0.00014 mmols of gadolinium is added to a 0.0001 mM solution of xylenol orange to get good sensitivity to unbound gadolinium. The absorbance for all samples are measured for wavelength of light between 400 and 700 nm. Then the 574 nm absorbance is divided by the 434 nm absorbance for each sample to obtain the yellow to purple ratio. All of these values were plotted vs. molar ratios of xylenol orange and GdCl3. The amount of unbound GdCl3 in the reaction sample was calculated by comparing it to the trend line from the standardized curve.

5.3 Results

5.3.1 Was the Conjugation of Antimicrobial to DOTA Successful?

Mass spectrometry of DOTA-gentamicin conjugate reveals a peak at 850.8 Da, which is the predicted molecular weight of the desired product plus a hydrogen adduct (Fig 1a). The 850.8 Da peak is not present in the gentamicin sample alone (Fig 5.1b) and therefore indicates a conjugation of gentamicin to DOTA. Mass spectrometry of the DOTA-vancomycin conjugate gives a peak at 1836.7 Da, the predicted molecular weight of the desired product plus a hydrogen adduct (Fig 5.2a). This peak is also absent in the vancomycin only sample (Fig 5.2b). In both the DOTA-gentamicin and DOTA-vancomycin conjugates the peak height in comparison to the gentamicin and vancomycin peaks in their respective samples indicates a relatively low but significant amount of conjugate is present, although mass spectrometry is not a quantitative method to determine precise yield.

In addition to mass spectrometry, HPLC is performed on each sample to determine if the conjugate can be separated from the rest of the reaction mixture. HPLC of the gentamicin conjugate does not show peaks for either the gentamicin or conjugate because the absorbance of those molecules is low (Fig 5.3). The absence of gentamicin or conjugate peaks on the HPLC indicates that it is unknown if the conjugate can be purified using HPLC. HPLC of the vancomycin conjugate however does give a new peak for the conjugate that is resolved from the other peaks, at ~18 minutes (Fig 5.4). The resolved peak indicates that DOTA- vancomycin can be purified using HPLC.

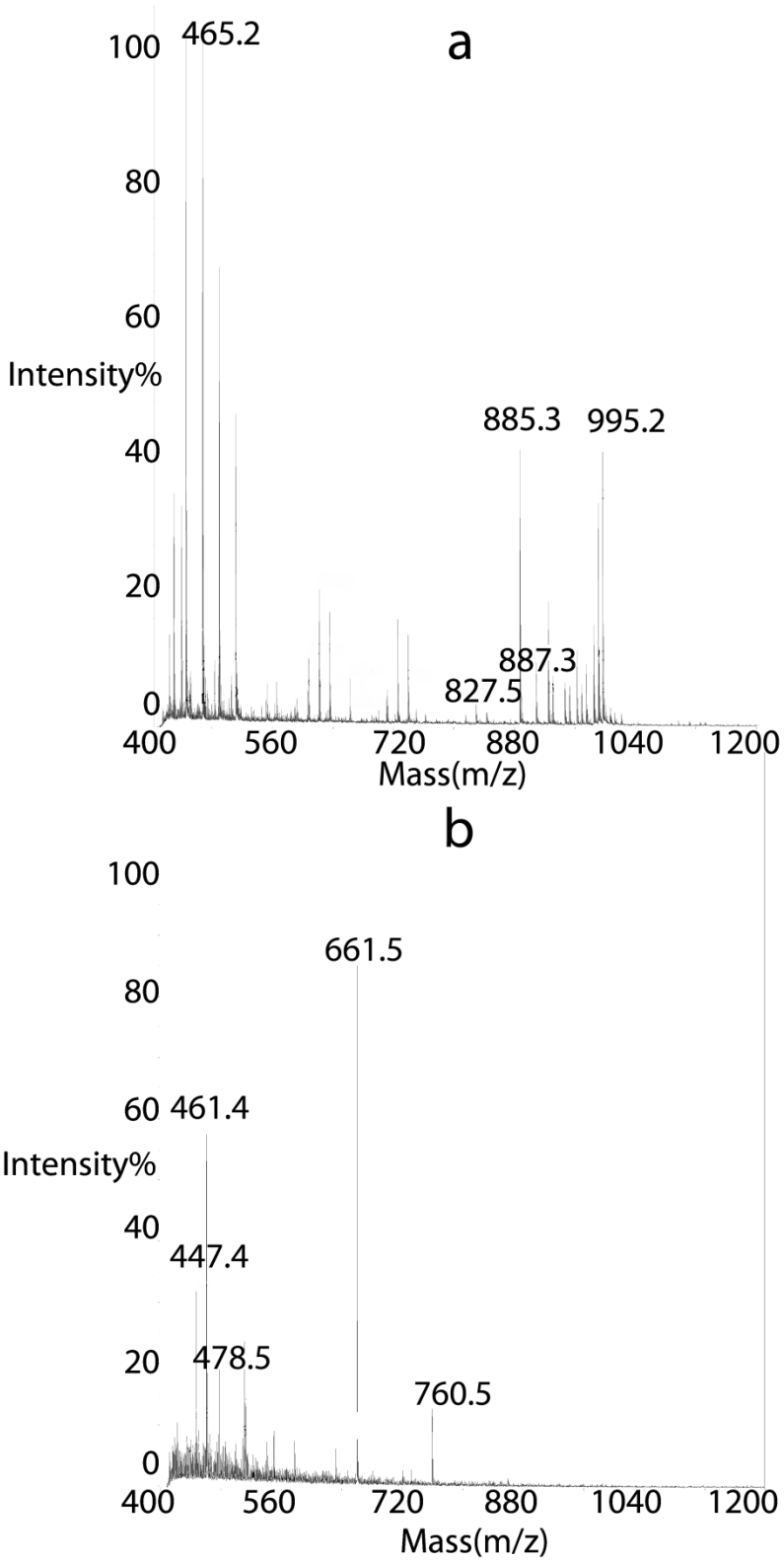

Figure 5.1: Mass spectrometry of (a) DOTA-gentamicin and (b) gentamicin only.

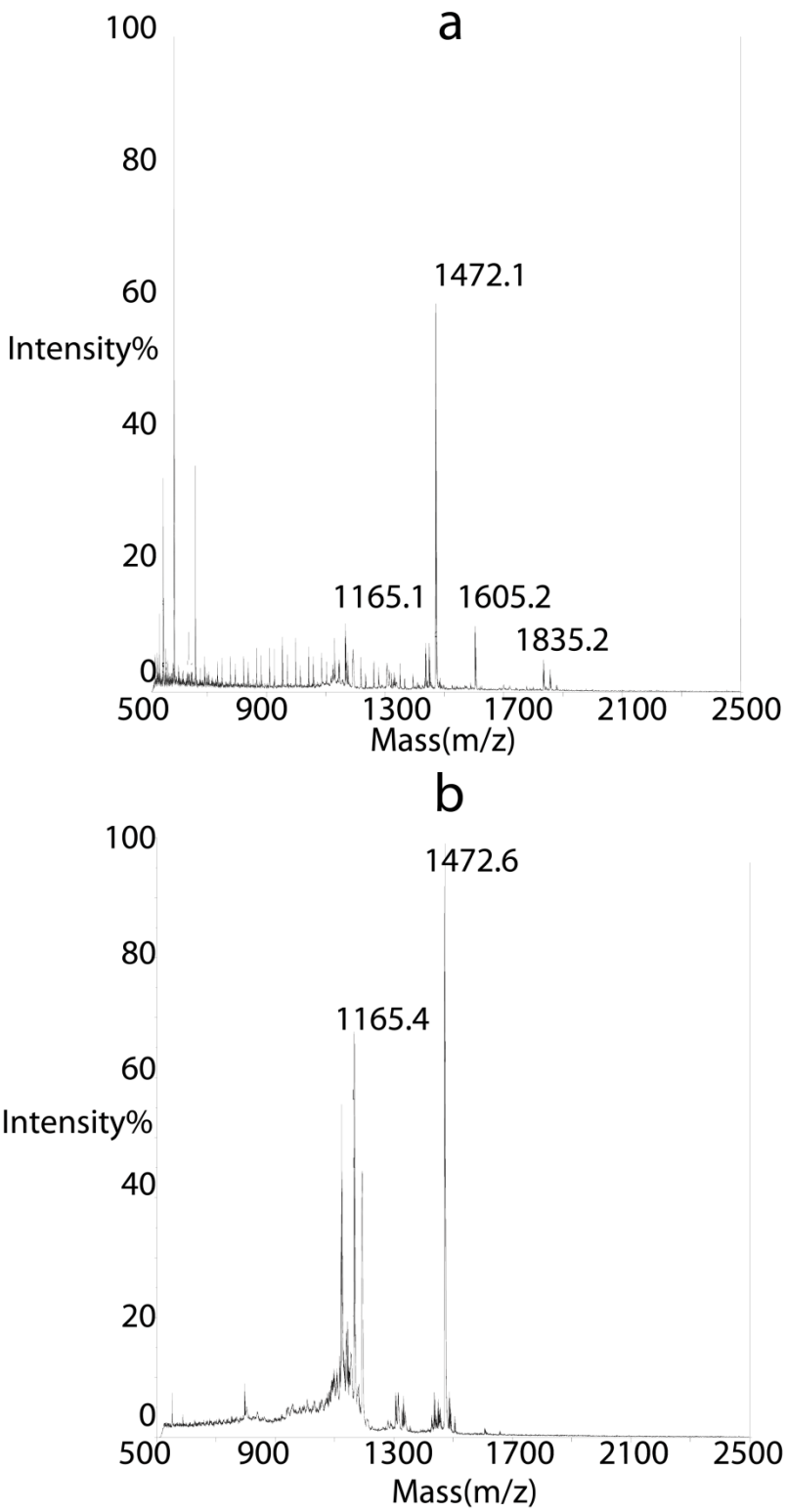

Figure 5.2: Mass spectrometry of (a) DOTA-vancomycin and (b) vancomycin only.

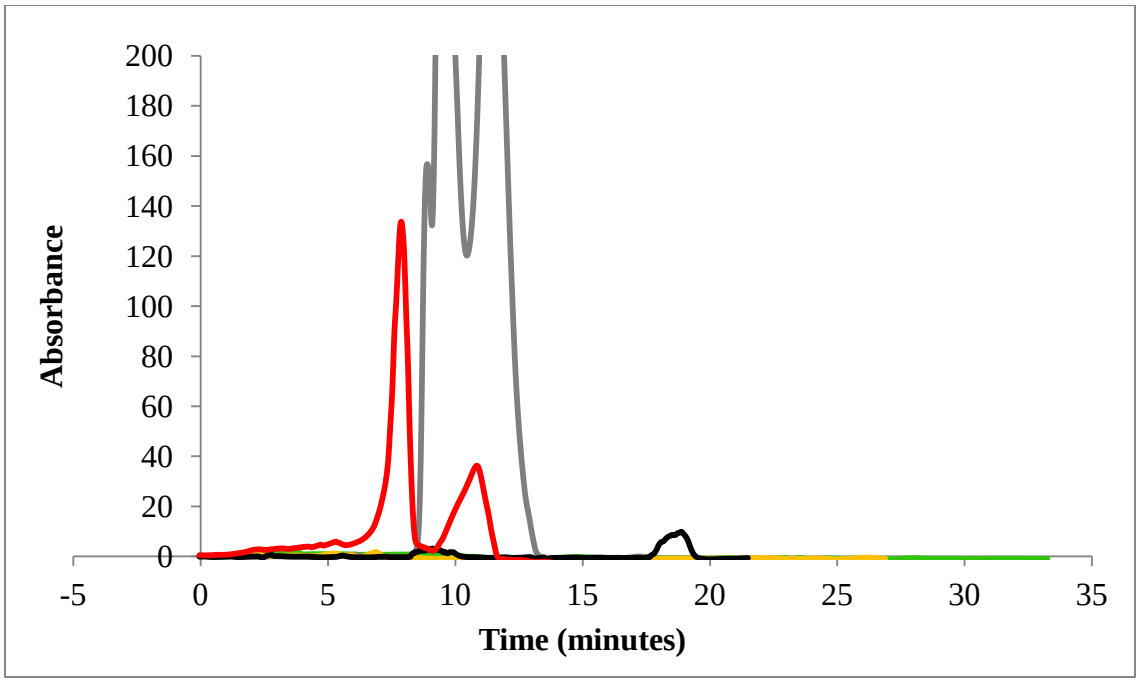

Figure 5.3: HPLC of DOTA-gentamicin (red) as well as all molecules used in the reaction including DOTA (green), sulfo-NHS (grey), EDC (yellow), and gentamicin (black).

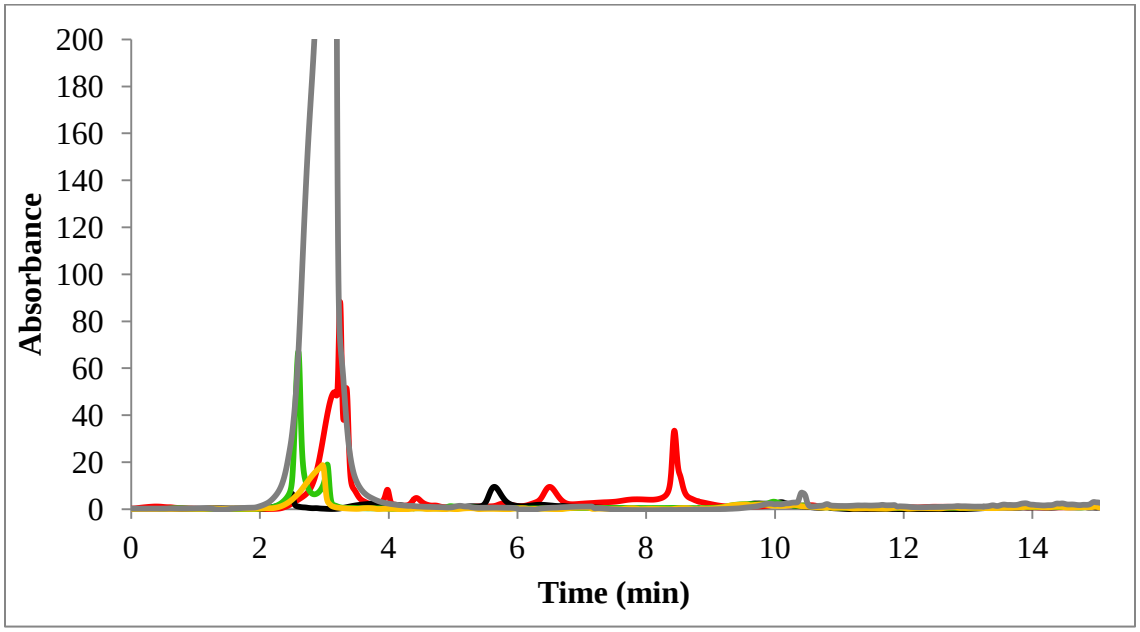

Figure 5.4: HPLC of DOTA-vancomycin (red) as well as all molecules used in the reaction including DOTA (green), sulfo-NHS (grey), EDC (yellow), and vancomycin (black).

5.3.2 Was the Chelation of Gadolinium Successful?

To determine if the chelation of gadolinium is successful, a xylenol orange assay is performed. When the chelated sample is compared to the standardized curve, it indicates that there is 6% unbound gadolinium in the Gd-DOTA-gentamicin sample and 1% unbound gadolinium in the Gd-DOTA-vancomycin sample (Fig 5.5). Therefore, most of the gadolinium was successfully chelated.

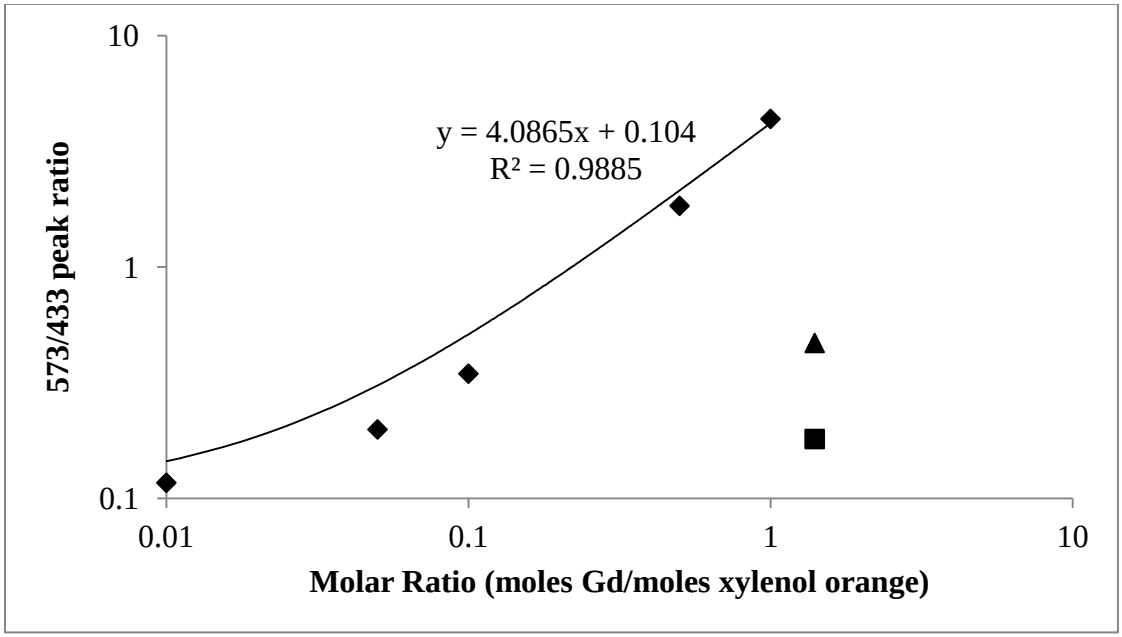

Figure 5.5: Graph of xylenol orange assay where the diamonds are a standardized curve of known concentrations, the triangle is for Gd-DOTA-gentamicin conjugate, and the square is for the Gd-DOTA-vancomycin conjugate.

5.4 Discussion

The results show that two different antimicrobials with primary amines, gentamicin and vancomycin, can be conjugated to DOTA and subsequently used to chelate gadolinium. It is expected that both vancomycin and gentamicin will retain their antimicrobial activity as in other studies where molecules where attached to the same location they maintained antimicrobial activity [122,123,127]. It is also expected that both of these conjugates will be MR visible. Gd-DOTA is a currently used MRI contrast agent. MRI contrast agents effect the relaxivity of the water molecules surrounding them. The relaxation of protons to concentration of contrast agent relationship can be quantified with the equation $\frac{1}{T_1} = \frac{1}{T_{1,0}} + r_1 C$ [68,80,81] where $T_{1,0}$ is a pre-contrast longitudinal relaxation time and T_1 is the post-contrast relaxation time, and r_1 is the longitudinal relaxivity constant of the contrast agent. The relaxivity of Gd-DOTA in saline is similar to the relaxivity of Gd-DTPA used in previous studies 3.8 $M^{-1}ms^{-1}$ [128]. The relaxivity of Gd^{3+} contrast agents tends to increase as the molecular weight of the complex increases [67]. It is hypothesized the relaxivity for both conjugates will exceed the relaxivity of Gd-DOTA alone becoming more MRI visible. In order to perform tests necessary to determine bactericidal and MRI activity, it is necessary to purify the conjugate. Purification can likely be done by scaling up the HPLC protocols using preparatory sized equipment. Scaling up would require a larger column, and larger injection assembly on the HPLC. When scaling up the velocity of the fluid through the column should be maintained, so the flow rate should be adjusted appropriately.

If the yield can accurately be determined and is reasonably high (~70%) it is unnecessary to separate all the reaction components. It is possible to account for unconjugated antimicrobial in tests for biological activity. Sulfo-NHS and EDC need to be removed because they could be toxic. Gd-DOTA however cannot be separated from a chelated antimicrobial in an MRI image, therefore it would be unknown if the signal was coming from Gd-DOTA or a chelated conjugate if delivered *in vivo*. Furthermore, if the two molecules had different relaxivities it would not be possible to calculate concentrations accurately. Therefore, it is necessary to separate Gd-DOTA, EDC, and Sulfo-NHS from the unchelated DOTA, chelated antimicrobial, unchelated and unconjugated antimicrobial before *in vivo* use. Since the HPLC shows good separation of DOTA-vancomycin it is thought that at least that conjugate can easily be separated from all of the other components

If tests show that antimicrobial and MRI activity are present this molecule could be used to visualize the time dependant distribution of these chelates in orthopaedic wounds using the methods shown in chapters 2-4. This would be beneficial because an active antimicrobial agent might have somewhat different properties from an inert MRI contrast agent. Using a conjugated antimicrobial and MRI contrast agent would lead to certainty in the location of antimicrobials being used to treat infections clinically. The limitation of using the conjugated antimicrobials shown here in a clinical setting would be the necessity to get FDA approval, whereas the methods shown in chapters 2-4 use FDA approved substances and devices off-label.

5.5 Conclusions

It is possible to link DOTA to antimicrobials using EDC chemistry and use the DOTA to chelate gadolinium. The separation of DOTA from the conjugate is necessary to accurately use this molecule to visualize local drug delivery.

Chapter 6: MATHEMATICAL MODELING OF LOCAL DRUG DELIVERY IN ORTHOPAEDIC WOUNDS

6.1 Introduction

Interest in local drug delivery is expanding both in research and industry. Local drug delivery vehicles can create a high concentration of drug in a specific region, while maintaining much lower levels of therapeutic in other areas of the body. This can focus treatment to an affected region, which is important in a variety of applications such as tumor treatment [3], pain management [4,5], tissue engineering [6], and infection management [7]. A common local drug delivery vehicles is polymethyl methacrylate (PMMA) bone cement, frequently used by surgeons to deliver antimicrobials to the site of orthopaedic infections.

Orthopaedic infection is a common affliction with 1-2% of joint replacement surgeries resulting in infection[11,12]. Once established there is a high rate of recurrence after surgical intervention, with 10-23% of patients requiring additional intervention [14,15]. Orthopaedic infection is complicated by the presence of biofilm. Microbes attach to the surface of an implant and form biofilm, which prevents the host defense system from eradicating the microbes [20,129]. Furthermore, the biofilm not only impedes the transport of antimicrobials to the microbes, but also induces phenotypic changes in the bacteria that make them more resistant to antimicrobials [19,22,130]. Biofilm bacteria require 100-1000 times the antimicrobial concentration required for planktonic bacteria [22]. Once a biofilm has reached maturity sections can fragment and move to other nearby locations. Biofilms

also spawn planktonic bacteria, which are small and can travel deeper into the surrounding tissue [19].

Orthopaedic infection is normally treated surgically by a two stage revision. In the first stage the implant is removed, a debridement of the biofilm and surrounding tissue is performed and the area is filled with antimicrobial loaded bone cement (ALBC). After the infection has been eradicated the second stage is performed where the implant is replaced [58]. The major concerns for re-infection are an incomplete debridement, biofilm debris in the wound and planktonic bacteria, which have not been eradicated by the ALBC, in the muscle. Therefore, the goal of antimicrobial treatment is to cover the entirety of the debridement surface as well as penetrate into the surrounding muscle with antimicrobials of sufficient concentration to kill the microbes.

In chapters 2-4 a method was outlined where contrast agent, antimicrobial surrogate, was imaged using magnetic resonance imaging (MRI) distributing from PMMA delivery vehicles placed *in vivo* in rabbit models. In those chapters antimicrobial surrogate delivery from PMMA rods placed in the quadriceps or intramedullary canal of the femur were studied. Also antimicrobial surrogate delivery was studied in orthopaedic wounds where either: (1) a piece of muscle tissue was removed and replaced with cement then the muscle tissue was closed over the top of the delivery vehicle or (2) a piece of muscle and cortex of the bone was removed and replaced with cement, but only the skin was closed. In these studies antimicrobial surrogate traveling along regions of high permeability such as intermuscular tissue planes and incision lines was repeatedly seen [99]. In order to determine the important transport factors involved in the drug distributions seen in the previous chapters, a mathematical model of the behavior will be developed.

A model of rabbit anatomy based on diffusion and convection of molecules through muscle, bone, intermuscular tissue planes, and wound spaces will be created. It will be assumed the major heterogeneous pressure source in this anatomy comes from capillary beds disrupted during surgery.

This research was conducted as a collaboration between Morgan Giers, Alex McLaren, Michael Caplan and Ryan McLemore. Morgan Giers and Michael Caplan design the models, following the guidance of Alex McLaren who provided several physiological phenomena that could be responsible for transport in that region. Morgan Giers was also responsible for execution of all models, analysis of all models, and writing this chapter.

6.2 Methods and Model Development

In this chapter Morgan Giers and Michael Caplan use COMSOL Multiphysics (COMSOL, Los Angeles, CA) numerical solver to model the transport of an antimicrobial *in vivo.* First a structure of the rabbit anatomy is drawn, then a mesh is created. Coefficients are input and COMSOL solves the model for each mesh point, first for fluid velocities in the Darcy's Law model, then for concentrations in the convection diffusion model (Fig 6.1).

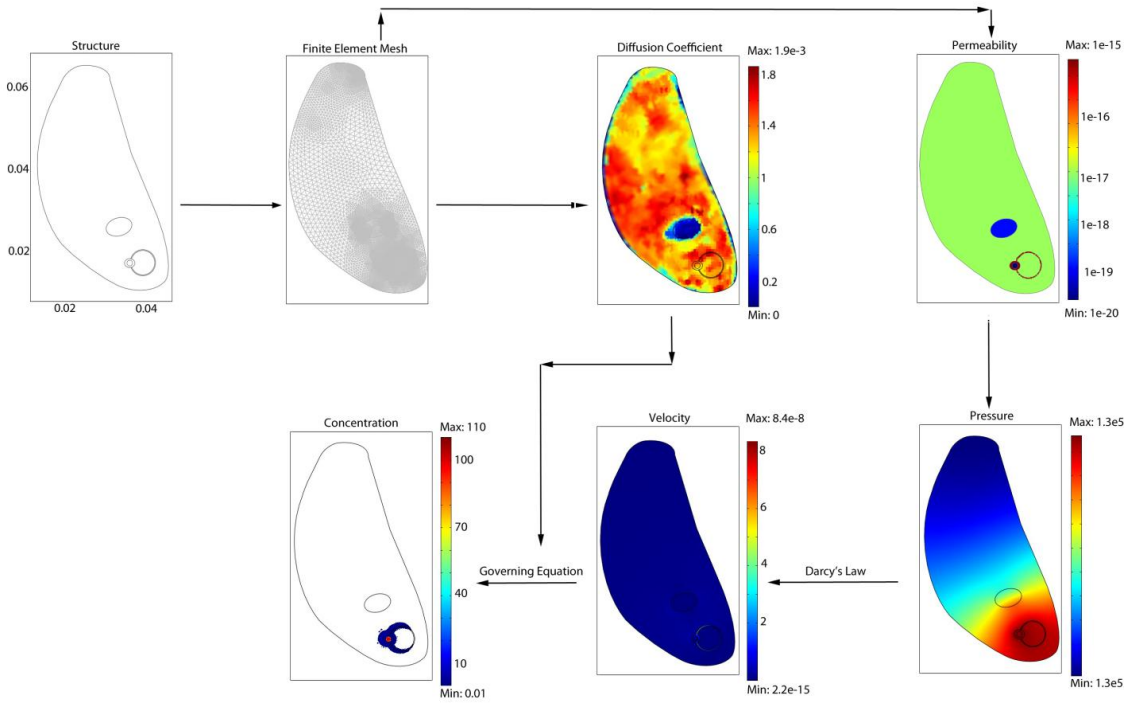

Figure 6.1: Schematic of steps in modeling. First a structure is drawn with different compartments, then a mesh is created, then the compartments are assigned coefficients such as diffusion coefficients. Furthermore, compartments are assigned initial conditions and boundary conditions. COMSOL then solves the model for each mesh point at each time point desired. First COMSOL will solve for pressure, from that it can use Darcy's Law to obtain fluid velocities. From the velocities and diffusion coefficients COMSOL can solve the governing equation for mass transport over time.

6.2.1 Governing Equation

The governing equation in transport phenomena describes three mechanisms involved in mass transport: diffusion, convection, and reaction. The equation states that the change in drug concentration over time equals the diffusion of the drug into or out of the system, the amount of drug leaving or entering the system due to bulk fluid flow and

the generation or consumption of the drug within the system. The governing equation is given mathematically in equation 6.1 [88]

$$\frac{\partial C}{\partial t} = D\nabla^2 C - fv\nabla C + R \qquad \text{(eq6.1)}$$

where C is the concentration, t is time, D is the diffusion coefficient, f is the filtration coefficient, v is the velocity of the fluid, and R is a reaction term. In this chapter Cartesian coordinates are used in a two dimensional model.

6.2.2 Drug Diffusion (ADC)

The diffusion coefficients needed to solve the first term of the governing equation can be estimated for specific locations within the tissue using an MRI obtained apparent diffusion coefficient (ADC) map. The ADC map approximates the diffusion coefficient of water in various tissues. In order to calculate ADC maps a series of diffusion weighted images (DWI) must be obtained. Diffusion weighted images were obtained in this experiment using TR=7.5s, with 30 slices collected. ADC maps can be calculated using a series of DWIs taken at different magnetic field strengths (B=0,200,700,1500 s/mm^2) using the following equation [63]

$$ADC = \ln\left(\frac{S_0}{S}\right)/B \qquad \text{(eq6.2)}$$

where ADC is the apparent diffusion coefficient of water in a voxel, S is signal intensity, S_0 is the signal intensity when B is zero, and B is the magnetic field strength. The ADC map used here was filtered using a median filter to reduce noise; The median filter replaces each pixel value with the median value of a group of pixels including itself and 4 nearest neighboring pixels. Since ADC map values are for water diffusion and not the

molecule of interest, the map values should be scaled to reflect the different molecule. The diffusion coefficient of the antimicrobial gentamicin in an aqueous buffer is $2x10^{-10}$ m^2/s and in alginate, similar to muscle tissue, is $6x10^{-12}$ m^2/s [23]. As such, the ADC map values were lowered by multiplying by $4.5x10^{-3}$ to make the average ADC value closer to the value of gentamicin in alginate.

6.2.3 Capillaries and Lymph

Arterial and lymphatic capillaries can be modeled using Starling's Law which states that the flow rate of fluid into and out of capillaries are proportional to the overall pressure difference between the inside of the capillary and the interstitium, considering both hydrostatic and osmotic pressures. Starling's Law is given in equation 6.3 [88]

$$Q = k((p_c - p_i) - (\pi_c - \pi_i))$$

(eq6.3)

where Q is the flow rate, k is the permeability, p is pressure, c stands for capillary, i stands for interstitial, and π is osmotic pressure. In this model Morgan Giers and Michael Caplan will make the assumption that all pressures inside the capillaries of both the lymphatic and arterial capillaries are constant. Morgan Giers and Michael Caplan will also assume that the osmotic pressure in the interstitial space is constant. Therefore, Starling's Law for both the lymphatic system and arterial reduces to a variable interstitial hydrostatic pressure term minus a constant value, an equation suggested by Michael Caplan. The two equations can be combined to form the equation

$$Q = -k(p_c - \rho_i)$$

(eq6.4)

where ρ is the constant pressure term. Morgan Giers and Michael Caplan assume that all fluid coming from the capillaries is evenly distributed and does not contribute to an overall directional flow. Therefore, equation 6.4 is used only as a sink term for any non-uniform pressure sources.

6.2.4 Flow from Edema

When capillaries are damaged due to surgery or some other cause they leak plasma and cause local edema. Alex McLaren hypothesized that the edema is the major source of flow in the anatomical location, muscle tissue, being modeled. In this chapter Michael Caplan and Morgan Giers will simplify this to a constant inflow of 1 μL/cm^{3}s. The pressure field was solved and subsequently used to calculate fluid velocity using Darcy's Law, which states that the fluid velocity through a porous medium is proportional to the pressure gradient, as shown in equation 6.5 [88]

$$\nabla \cdot \left(\rho \left(-\frac{k}{n \nabla p} \right) \right) = F$$

(eq6.5)

where ρ is density of the fluid, k is the permeability constant, n is viscosity of the fluid and F is a source. This model also assumes the fluid is incompressible and so continuity equation [88] is true.

$$\nabla \cdot v = 0 \qquad \text{(eq6.6)}$$

6.2.4 Peclet Number

The Peclet Number is a used to compare convection and diffusion within a tissue and assess the contributions of each mechanism to the transport of a molecule. The Peclet number can be calculated from equation 6.7 [88]

$$\mathrm{Pe} = \frac{\mathrm{Lv}}{\mathrm{D}} \qquad \text{(eq6.7)}$$

where Pe is the Peclet number, L is the characteristic length, v is the fluid velocity, and D is the diffusion coefficient. When the Peclet number is high (>10) the transport can be considered convection dominant. When the Peclet number is low (<1) the transport can be considered diffusion dominant. Regions with Peclet numbers in-between 1 and 10 are considered to have significant contributions from both convection and diffusion.

6.2.6 Boundary Conditions

The skin was treated as a no flux boundary and was modeled with equation 6.8 [88].

$$\nabla \mathrm{C} = 0 \qquad \text{(eq6.8)}$$

All interior boundaries were considered continuous to the next compartment and were modeled with the following equation:

$$\nabla \mathrm{C}_1 = \nabla \mathrm{C}_2 \qquad \text{(eq6.9)}$$

where C_1 is the concentration at the boundary in compartment 1 and C_2 is the concentration at the boundary in compartment 2.

6.2.7 Mesh Size

The effect of mesh size on result is analyzed for one model. The mesh is refined to three different sized. The concentration map plots are analyzed visually for the three mesh sizes at several time points to determine similarity between the results. The results

are presented in figure 6.2. Figure 6.2 is a model involving both convection and diffusion. The details of the model presented in figure 6.2 are discussed at length in 6.3.2 and this model is also shown in figure 6.5. There was very little change in the concentration map solution using three different mesh sizes. The edge of figure 6.5 a is not as smooth as figure 6.5 b-c, but the overall shape is similar. In order to get a more clearly defined edge without causing excessive computational time the mesh size shown in figure 6.5 b was used for all models.

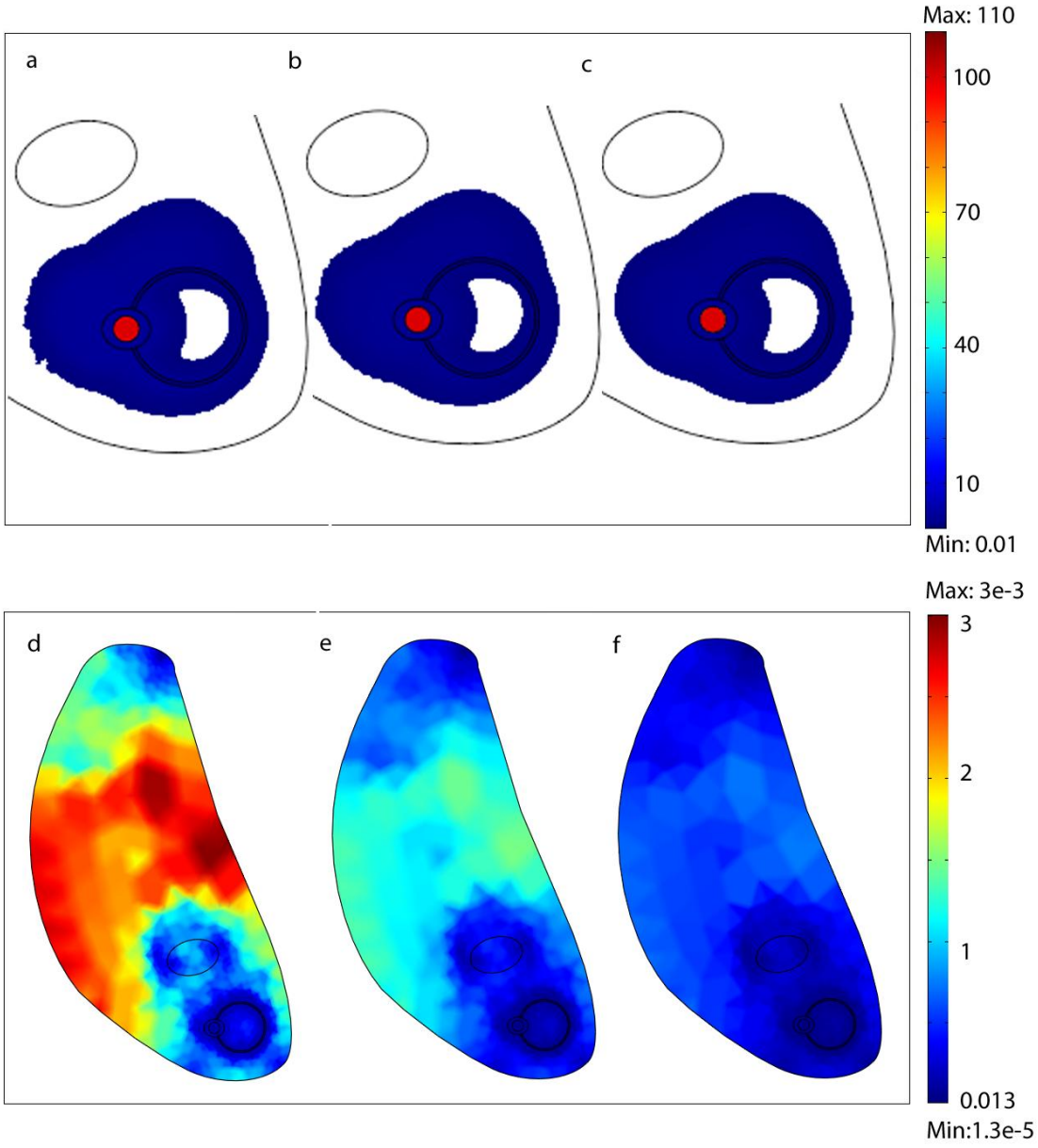

Figure 6.2: Convection and diffusion model concentration map in units of mM at five hours (a) using the mesh size presented in (d), (b) using the mesh size presented in (e), or (c) using the mesh size presented in figure (f). (d-f) are plots of the mesh element area used in (a-c). The scale bar for mesh element area is in m^2.

6.3 Results

6.3.1 Does the ADC Map Matter?

An apparent diffusion coefficient map is obtained using MRI. These map values can be imported into COMSOL to generate a discrete diffusion coefficient for every 0.6 mm^2 in the model structure. The histogram of the ADC map gives an average value of $1.2x10^{-9} \pm 0.4x10^{-9}$ m^2/s, which is less than the water self diffusion coefficient, $2.4x10^{-9}$ m^2/s [131]. Since the model is being created to describe the motion of a small molecule, gentamicin (in alginate $D=6x10^{-12}$ m^2/s [23]), the ADC map value diffusion coefficients are multiplied by $4.5x10^{-3}$ to make the average value closer to that of gentamicin in alginate while maintaining the spatial variation provided by the map. When a diffusion only model is run using MRI ADC map values it results in a small circular shaped distribution of contrast around a cement rod, as shown in figure 6.2a. Alternatively, a model can be run using values input by the user for each compartment, making the diffusion coefficients uniform within the compartment. Results from a model with a value of $6x10^{-12}$ m^2/s assigned to the muscle tissue and a value of $1x10^{-12}$ m^2/s assigned to the bone are shown in figure 6.2b. The diffusion coefficient for the bone is estimated from the adjusted diffusion coefficient of bone in the ADC map. The result from a model run with uniform diffusion coefficient (Fig 6.2b) is negligibly different from the model run with ADC map values (Fig 6.2a). An illustration of the diffusion coefficients given in each of these two models is shown in figures 6.2c-d.

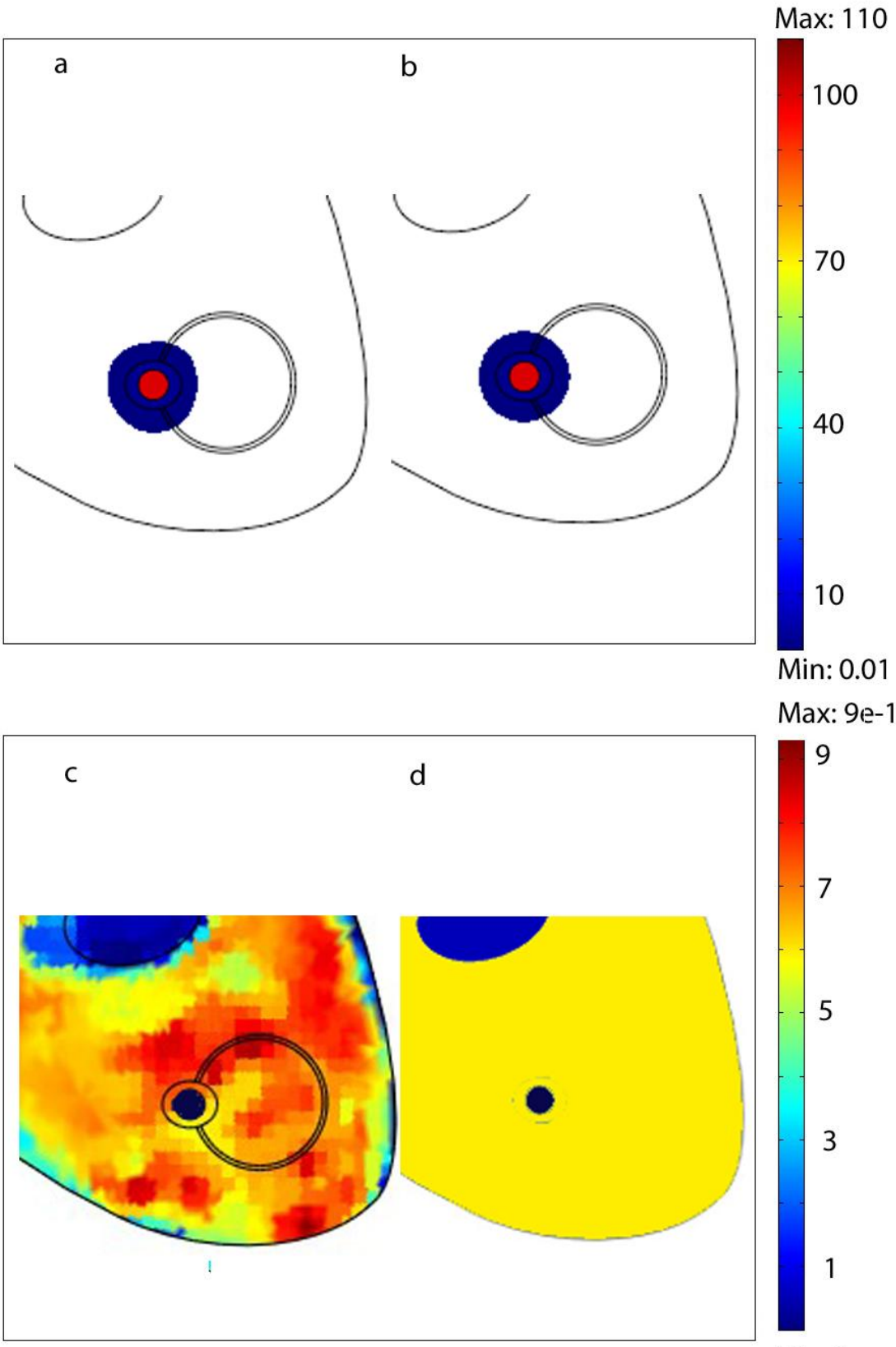
a
b
Max: 110
100
70
40
10
Min: 0.01
c
d
Max: 9e-12
9
7
5
3
1
Min: 0

Figure 6.3: Diffusion only model concentration map in units of mM at five hours (a) using ADC Map values as diffusion coefficients or (b) using constant values for diffusion coefficients. Model diffusion coefficients (c) using the ADC map or (d) using constant values in m^2/s.

6.3.2 Is Convection or Diffusion Dominant?

The ADC map overlooks some physiology because of its poor resolution, 0.6 mm^2. Features such as intermuscular tissue planes cannot be visualized in that modality, but are clearly visible in T_1 weighted images, whose resolution is 4 times as great. Intramuscular tissue planes are loose, largely acellular, connective tissue between muscle groups. In the experimental MRI contrast agent distribution images, shown in chapters 2-4, contrast agent was often seen preferentially traveling along tissue planes [99]. A compartment is created in the model structure to mimic this anatomical feature. The tissue plane compartment is given a diffusion coefficient of $2x10^{-10}$ m^2/s, equivalent to the gentamicin in an aqueous buffer [23], because it is assumed that the actual diffusion coefficient of gentamicin in an intermuscular tissue plane cannot exceed that of gentamicin in buffer. When a model is run under these conditions some gentamicin travels along the tissue plane, but substantially more travels into the tissue (Fig 6.3).

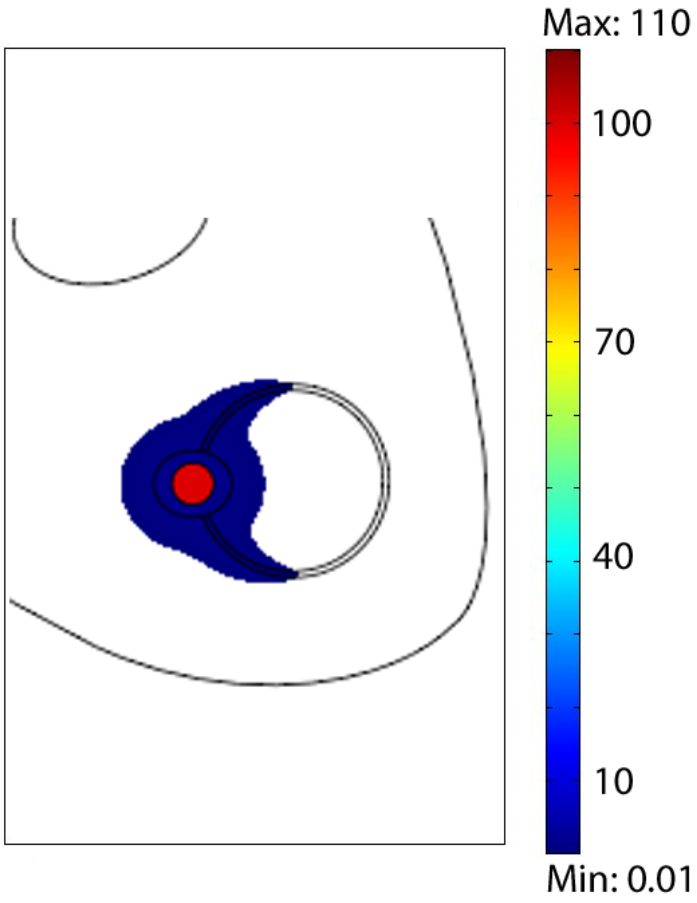

Figure 6.4: Model concentration map in units of mM at one hour in a diffusion only system, where the diffusion coefficients are increased in the intramuscular tissue plane.

In order to capture the preference seen for contrast agent traveling along tissue planes and incision tracks, as discussed and illustrated in chapters 2-4, convection is added to the model. A flow source with a constant value of 1 $\mu L/cm^3 s$ is added around the implant to model edema from damaged capillaries resulting from device implantation. A flow sink term of $-10^{-12}(p_i-101325)$ Pa is applied to all other compartments, meant to represent capillary and lymphatic uptake. The sources and sinks create a pressure gradient from the source compartment around the delivery vehicle to the surrounding

tissue and rest of the leg, as shown in figure 6.4a. Different permeabilities were applied to each tissue. The permeability of the muscle is lower than the tissue plane. Unless otherwise noted the diffusion coefficients and permeabilities for this and all subsequent models are given in table 6.1. The tissue plane is an area of low resistance to flow, high permeability, and has a higher fluid velocity than the surrounding tissues, as shown in figure 6.4b. When the resulting contrast distribution is plotted there is a large preference for contrast traveling in the tissue plane (Fig 6.4). The same model was run for a coronal view of a leg. In this model the diffusion coefficient in the vertical direction is $6x10^{-11}$ m^2/s and in the horizontal direction is $6x10^{-12}$ m^2/s because the diffusion coefficients along the direction of muscle fiber alignment is higher than perpendicular to them (Fig 6.5). In this model contrast agent also travels along the tissue plane.

Table 6.1: Model concentration map at one hour in a diffusion only system, where the diffusion coefficients are increased in the intramuscular tissue plane

	Diffusion Coefficient (m^2/s)	Permeability (m^2)
Muscle	$6x10^{-12}$	$2x10^{-17}$
Bone	$1x10^{-12}$	$1x10^{-19}$
Tissue Planes	$2x10^{-10}$	$2x10^{-15}$
Bone Cement	$1x10^{-14}$	$1x10^{-20}$
source	$2x10^{-10}$	$2x10^{-15}$
biofilm	$7x10^{-10}$	$2x10^{-17}$

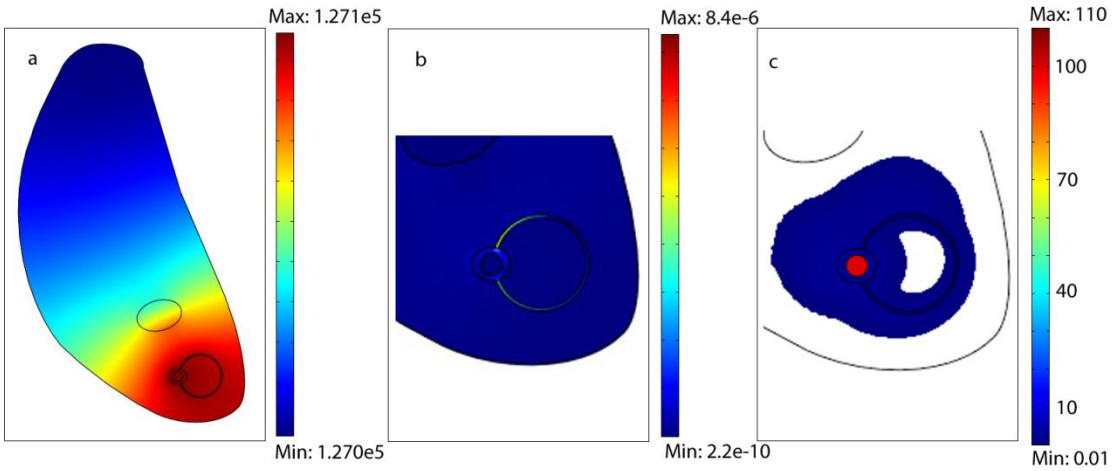

Figure 6.5: Solution to model with both convection and diffusion at five hours where (a) is the pressure field in Pascal (b) is the velocity solution in m/s and (c) is the concentration solution in mM.

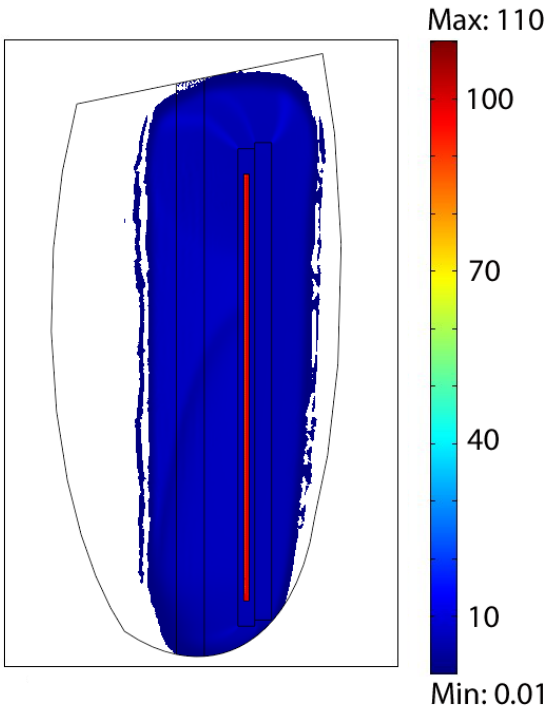

Figure 6.6: Solution to model with both convection and diffusion at five hours where (a) is the pressure field in Pascal (b) is the velocity solution in m/s and (c) is the concentration solution in mM.

In order to assess if the transport in the musculoskeletal system is primarily dominated by convection or diffusion, two models are created with a all diffusion coefficient decreased by an order of magnitude or increased by an order of magnitude. The resulting concentration distributions (Fig 6.6a-b) show more gentamicin penetrates muscle when the diffusion coefficients are high with respect to the permeability. A plot of the Peclet numbers for each of these models is given in figure 6.6c-d. When the Peclet number is high (>10) the transport can be considered convection dominant. When the Peclet number is low (<1) the transport can be considered diffusion dominant. Regions with Peclet numbers in-between 1 and 10 are considered to have significant contributions from both convection and diffusion. In the model with lowered diffusion coefficients there is a region in and near the tissue plane that is controlled by both convection and diffusion, but the majority of the transport in the leg is controlled by convection (Fig 6.6c). In the model with increased diffusion coefficients the region near the implant is controlled by diffusion, but there is a region in the middle of the leg where convection plays a role (Fig 6.6d). It seems that within a 2 order of magnitude range there is always some role played by both convection and diffusion in the transport of gentamicin. This indicates that both mechanisms of transport should be included in the model.

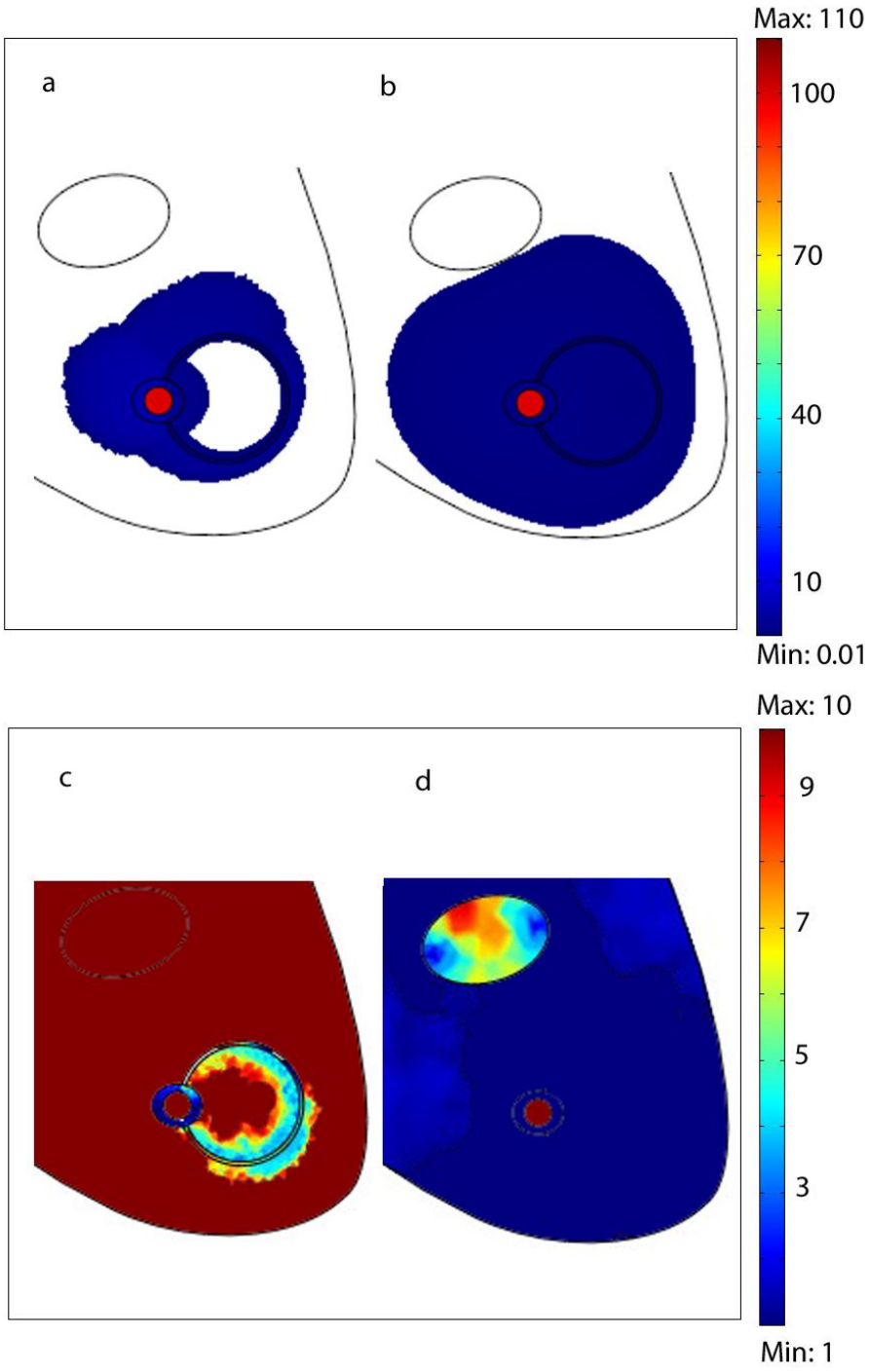

Figure 6.7: Concentration map (in mM) solutions for two models with the same permeabilities and different diffusion coefficients at five hours where model (a) has diffusion coefficients decreased by one order of magnitude from figure 6.4 and (b) has

diffusion coefficients increased by one order of magnitude from figure 6.4. (c) and (d) are the associated Peclet number plots for (a) and (b) respectively.

Since the tissue planes in rabbits are so loosely connected they can easily be separated during a surgical procedure. The variable separation between muscle groups could lead to a range of permeabilities in the tissue plane. Figure 6.7 shows models where the permeability of the tissue plane only has been decreased by an order of magnitude (Fig 6.5a) or increased by an order of magnitude (Fig 6.7b). The two models have negligibly different distributions.

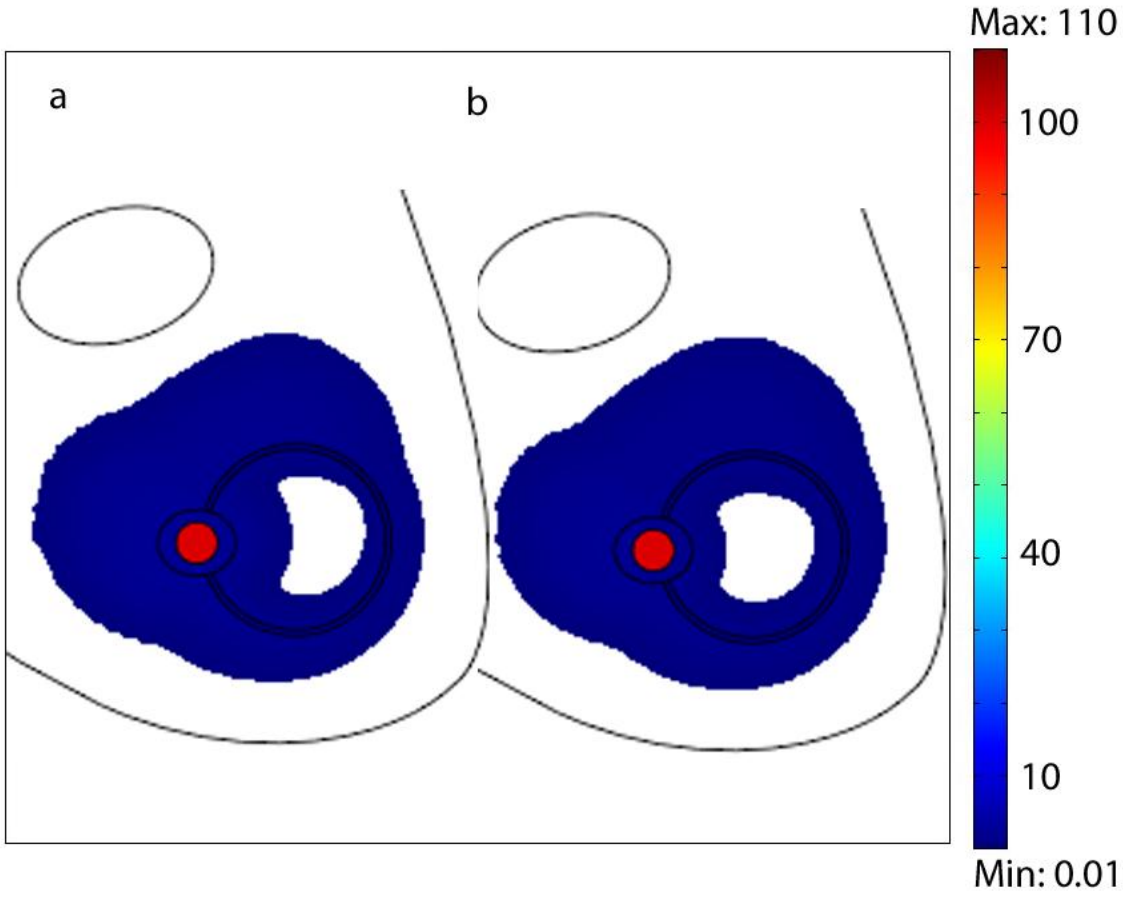

Figure 6.8: Model with increased permeability in intramuscular tissue plane at 1 hour where model (a) has $k=2x10^{-15}\ m^2$ and (b) has $k=2x10^{-13}\ m^2$.

6.3.3 What do Different Materials Look Like?

There is a large variety of materials that are explored as delivery vehicles in antimicrobial release as well as other applications. It is important to consider how changing material properties affect *in vivo* drug distribution. To explore changing material properties a model with lower diffusion coefficient ($D=1x10^{-16}\ m^2/s$) and permeability ($k=1x10^{-22}\ m^2$) is created. A model with higher diffusion coefficient ($D=1x10^{-12}\ m^2/s$), similar to the diffusion coefficient of biodegradable polyanhydride materials, and permeability ($k=1x10^{-18}\ m^2$) was also created. The spread on both models is similar, but the model with the faster releasing device has about 100 times higher concentration (Fig 6.8a-b). When the total molar mass left in the delivery vehicle is graphed over time the difference between these two vehicles is dramatic. The faster releasing vehicle releases over half its load in the first 19 hrs, while the slowly releasing vehicle retains almost all its load over that period of time (Fig 6.8c-d).

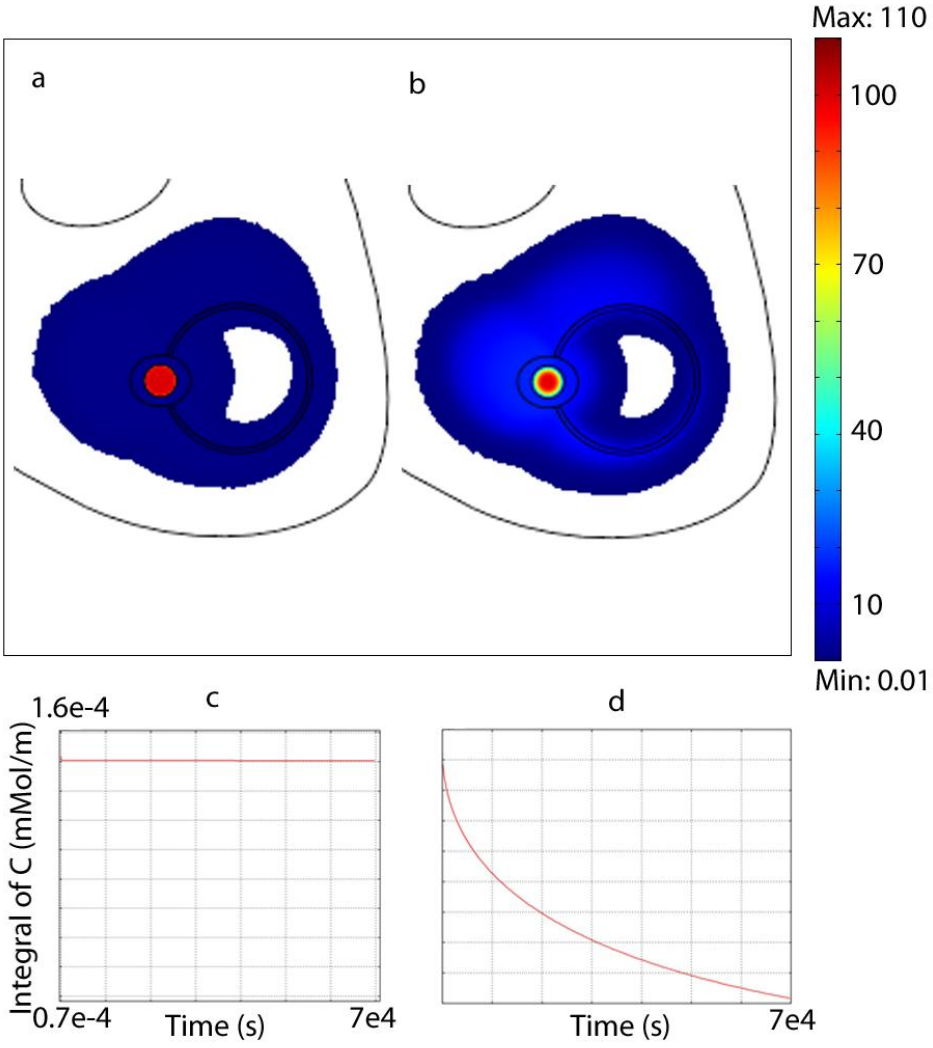

Figure 6.9: Model with (a) decreased diffusion coefficient ($D=1x10^{-16}$ m^2/s) and permeability ($k=1x10^{-22}$ m^2) of the drug delivery vehicle at five hours and (b) increased diffusion coefficient ($D=1x10^{-12}$ m^2/s) and permeability ($k=1x10^{-18}$ m^2) of the drug delivery vehicle at five hours. The concentration units are in mM. (c) and (d) are the total mass left in implants, from (a) and (b) respectively, as a function of time.

6.3.4 What do Different Wound Types Look Like?

In order to assess how universal the model is for different types of surgical procedures, models with different geometries are created and given the same parameters as the previous model (Fig 6.4). The models are compared to wounds created in chapters 2-4. Briefly, an intramuscular rod, an intrafemoral rod, a partial thickness muscle removal, and a full thickness muscle and bone removal model are shown. In each structure, figures 6.9 a, c, and d, there is a region surrounding the implant that is assumed to be damaged tissue and is given a source term. In figure 6.9d a region of less damaged tissue is modeled extending from the skin to the implant, representing an incision line that remains unclosed. It is assumed that the vasculature is less damaged by an incision than in the removed muscle section, so the incision compartment is assigned a flow source (10^{-5} kg/m^{3}s) two orders of magnitude less than the tissue adjacent to the implant (10^{-3} kg/m^{3}s). In the intramedullary model there is no region of damaged vasculature. The modeled distributions have similarities to their experimental counterparts. In figure 6.9c there is some contrast entering the tissue plane as seen in the experimental image in figure 6.9g, but the overall distribution is larger in the model than in the experimental image. In figure 6.9d the contrast travels around the tissue plane, but contrast in figure 6.9h is not seen in that region. Also in figure 6.9d more contrast travels towards the back of the leg than the front and in figure 6.9h the opposite occurs. Each of these have different surgeries with different degrees of tissue damage. This model is not entirely universal and there are aspects that are not captured by the current parameters.

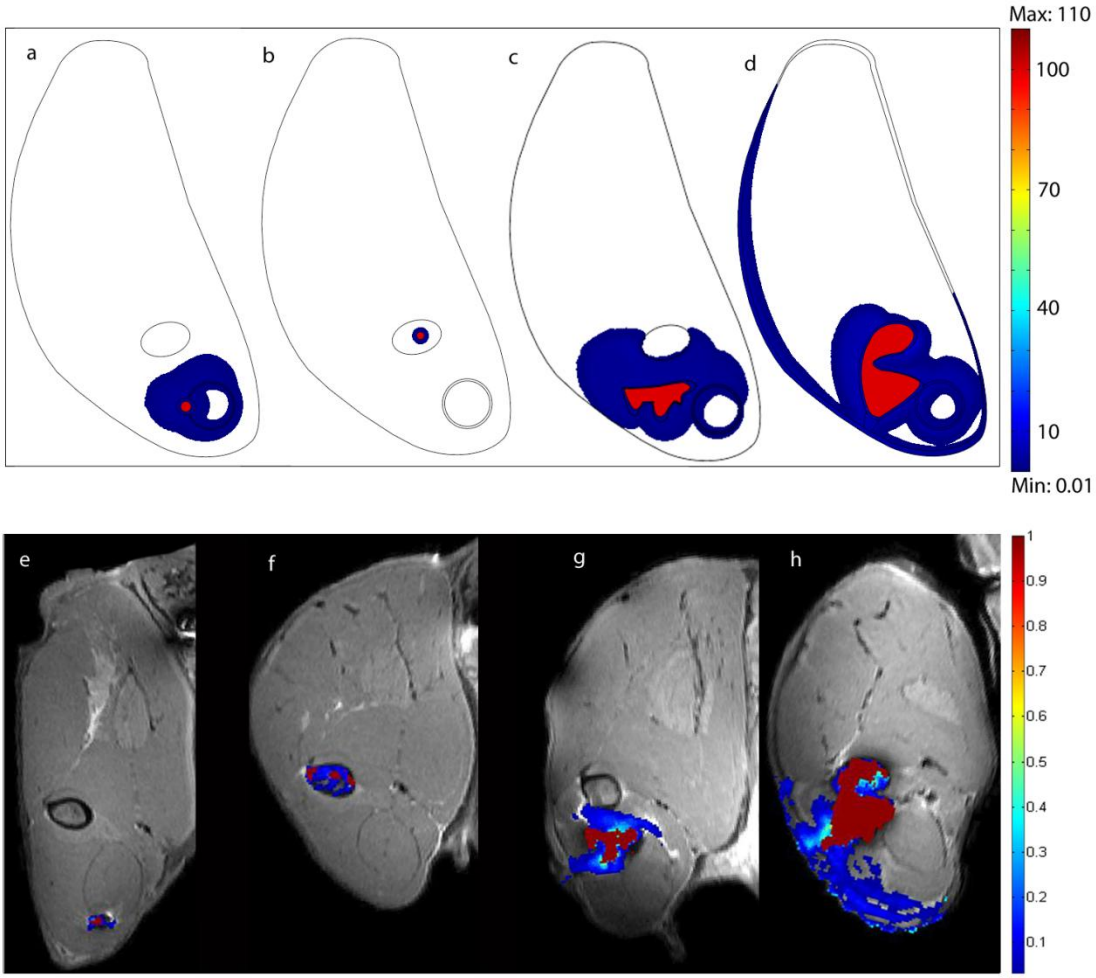

Figure 6.10: Model of 4 different wound types a five hours (a) intramuscular rod, (b) intrafemoral rod, (c) partial thickness muscle removal, and (d) full thickness muscle and bone removal model. Also shown in (e-h) is the MRI distribution images at 5.5 hours for model (a-d) respectively. All parameters are entered for each model as given in table 1. Model (d) has a lower pressure source term than the wound area included to model the open incision sight that has less damaged tissue than the wound. The incision area extends from the wound area to the subcutaneous tissue plane. Both scale bars are in mM.

6.4 Discussion

The model showed that ADC maps are not necessary to appropriately model diffusion in muscle tissue. ADC maps might be more practical and necessary in models of other anatomies, where the diffusion coefficients of the important features are captured by the ADC map and the structure is more difficult to draw. Obtaining and using an ADC map is difficult, time consuming, and costly, so if the results are not compromised there are many benefits to using a per compartment diffusion coefficient rather than an ADC map.

Diffusion only models did not capture all the mechanisms responsible for the distributions seen in experimental images so moderate levels of convection could easily be responsible as a transport mechanism for an antimicrobial in a wound. The convections is important to the anisotropy of distribution. Areas of high permeability offer low resistance to flow and easily carry drugs along those paths. Areas of high permeability in the rabbit included tissue planes which are more rigid in human patients and are unlikely to display the same behavior; however, these tissue planes can be generalized for any high permeability region, such as incision lines. Incisions are not generally left open in humans, but even closed incisions are likely to have a slightly greater permeability. Most importantly those high permeability features reveled the most about underlying transport mechanisms. Even if a surgeon normally closes a high permeability incision, that region could just be modeled with a smaller permeability and the other transport mechanisms should be otherwise the same.

COMSOL does not converge well when there are regions where the gradients are very steep. Regions with steep gradients include regions that are very small, but contain different transport properties from its neighbors. In this model the wound region was very

large so that COMSOL could more easily solve it. Realistically the region might be smaller and the effects less dramatic, particularly in the intermuscular rod model.

An *in vivo* model can be used to explore new material options. There are many mathematical models describing how drugs elute from local delivery vehicles, but few describing how drugs move *in vivo* from a local delivery source. There are some *in vivo* models of drug delivery to tumor sights [77,79,132-135]. Modeling the *in vivo* parameters can create a framework where a solution, such as different material parameters, can be engineered based on the desired result. For instance, if it was desired to cover a larger region of the leg for a specified period of time, different loading amounts and material parameters could be explored in the model before choosing a material to test in an experimental animal model.

Although a single model cannot be applied for all surgical situations, it can help in describing general behaviors. The experimental models from chapters 2-4 have shown a large animal to animal variability. The animal to animal variability could stem from parameters like different wound sizes, different placements of the implant, and different degrees of separation in the tissue planes. It is unlikely these models will be able to predict precise locations of antimicrobial distribution, but these models can help us explain the mechanisms seen in the MRI images and suggest how changing surgical or material parameters can effect distributions in a general way.

6.5 Conclusions

The model showed that ADC maps are not necessary to appropriately model diffusion in tissue. Diffusion only models do not capture all the mechanisms responsible

for the distributions seen in experimental images so moderate levels of convection could easily be responsible as a transport mechanism for gentamicin in a wound. An *in vivo* model can be used to explore new material options. Although a single model cannot be applied for all surgical situations, it can help in describing general behaviors.

Chapter 7: CONCLUSIONS AND FUTURE WORK

In this work Morgan Giers, Alex McLaren, Chris Estes, Kenneth Schmidt, Ryan McLemore, and Michael Caplan developed a new method for visualizing the distribution of antimicrobial surrogate from local delivery vehicles in orthopaedic wounds. This team found contrast agent distribution could be seen in near real time [99]. Also it was possible to perform quantitative analysis on those images. The strengths and weaknesses of the method and detailed the image processing required for quantification of drug distribution was shown[105]. The method was used in minimally invasive procedures, IMR and IOR, as well as complex wound environments, PTM and FTMB, and were able to see different behaviors based on the type of wound [106]. It was repeatedly seen that contrast agent remained mostly within the local wound space and traveled furthest down paths of least resistance to flow. A mathematical model was created of the hypothesized important factors affecting the drug distribution in tissue. Morgan Giers and Michael Caplan with input from Alex McLaren and Ryan McLemore were able to model similar behaviors to that seen *in vivo* by assuming there was edematous flow from the damaged tissue and using a combination of convection and diffusion transport mechanisms.

7.1 Spatiotemporal Distribution of Contrast Agents Delivered to Orthopaedic Wounds

In order to adequately treat an infection, high concentrations of antimicrobial must be both achieved and maintained. Bactericidal effect is a function of both concentration and time [136]. In the work outlined thus far significant differences in volume

or total mass of antimicrobial surrogate were not seen in the images as a function of time. The lack of significant change over time is likely due to the short period of time over which the images were acquired. Images were acquired over times less than 6 hours after implantation of the delivery vehicle when the expected length of treatment is several days to weeks long [2]. For this reason this group is interested in looking at the distribution at longer time points. The preliminary data from one rabbit shows nearly all the contrast in concentrations above the visible range is no longer present at ~3 days (Fig 7.1). More replicates of longer the longer study are currently underway. The data from this one animal, however, fits with the previous short time period values from previous animals (Fig 7.2). In figure 7.2 the total milligrams of contrast calculated in the control images are also provided to show that at ~3 days the image with contrast approaches the same mass as the control images.

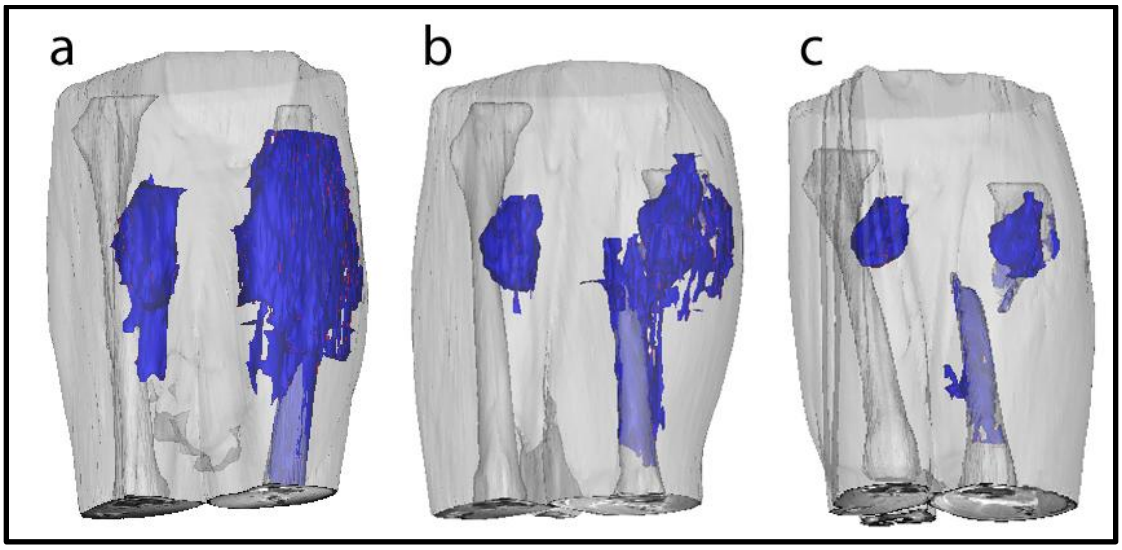

Figure 7.11: 3D reconstruction of Gd-DTPA distribution and bone cement with 2g of Gd-DTPA and 8 g xylitol porogen per 60 grams of PMMA at (a) 1hour (b) 1 day and (c) 5 days.

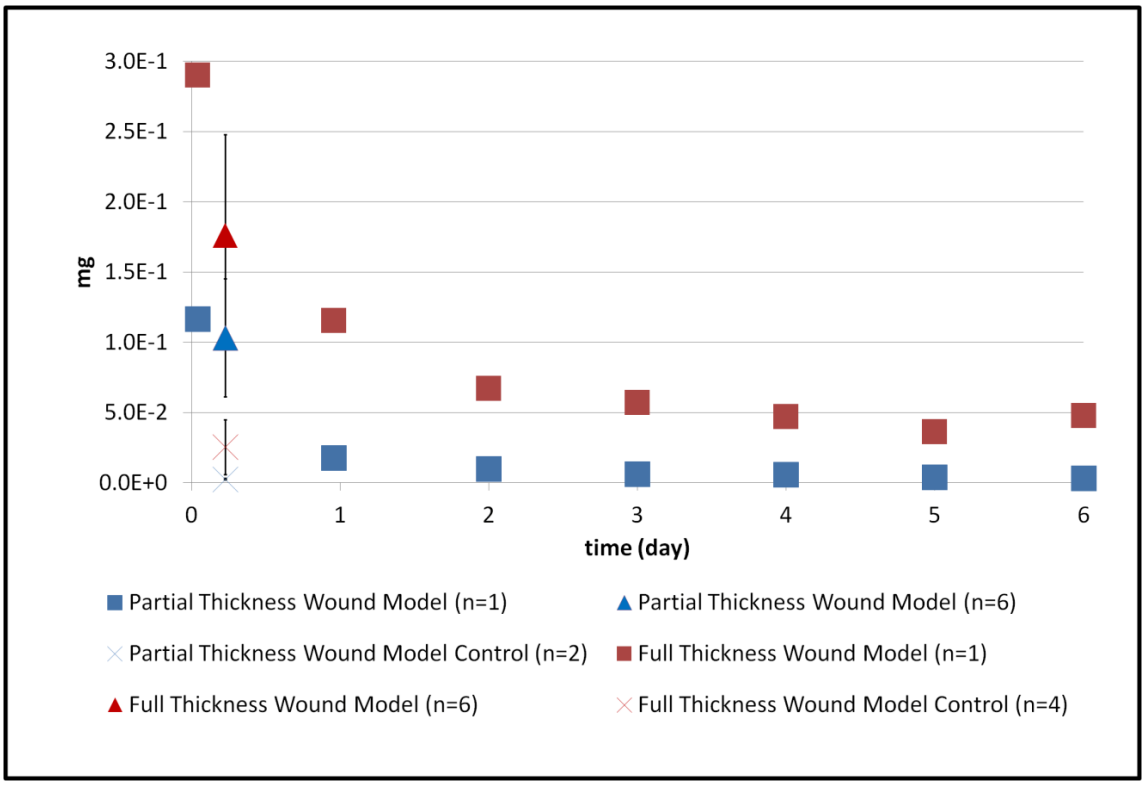

Figure 7.2: Graph of total milligrams of contrast in the image of an individual rabbit over time compared with average mass of contrast agents for the same wounds in multiple other animals at 5.5 hrs.

7.2 Quantification of Differences Between Active Therapeutic Agent and Inert Molecule Distributions

In order to use the methods outlined in chapters 2-4 as a clinical tool therapeutic agents would need to be present. These therapeutics could be present as conjugated antimicrobials and MRI contrast agents, as outlined in chapter 5, or simply co-delivered with Gd-DTPA. Co-delivery of antimicrobials and Gd-DTPA would be a more versatile method since co-delivery would avoid complex chemical synthesis of new molecules and could simply utilize currently available pharmaceuticals. Ideally any combination of

antimicrobials to be co-delivered with Gd-DTPA in order to treat a specific infection on a patient specific basis. A patient could then receive an MRI within the first 24 hours to confirm if the surgical intervention is likely working. The major assumption of a co-delivery procedure would be that an inert contrast agent and active antimicrobial have the same transport and one is analogous for the other. So by visualizing the Gd-DTPA with MRI it could be assumed that the therapeutic was in the same locations. Theoretically the transport of most antimicrobial molecules should be similar to Gd-DTPA since they are all low molecular weight, hydrophilic compounds; however, providing evidence that the contrast agents and antimicrobials behave the same would validate the method. Arguments as to why they would not behave the same are discussed later in this section. The behavior of the two different types of molecules can be compared both in their delivery from the delivery vehicle and their distribution in actual tissue.

In order to determine if an antimicrobial and Gd-DTPA deliver the same from the bone cement a simple *in vitro* elusion profile could be obtained. The elusion profile can be measured by placing a sample of the cement containing both MR and antimicrobial agents in a relatively large volume of phosphate buffered saline. The fluid can be replace at certain intervals and the concentrations of each agent in that fluid measured. If they are the same this would indicate that the two types of molecules deliver similarly from the vehicle. For the antibiotic vancomycin the concentrations can be determined using HPLC. A standardized curve can be obtained for the area under the absorbance curve (AUC) for a series of known concentrations (Fig 7.3). An equation can then be obtained describing that relationship and applied to unknown concentrations of samples from the *in vitro* elution study. A plot of total mass released over time can be constructed (Fig

7.4). The vancomycin elution profile can be compared to the elution profile of Gd-DTPA. Gd-DTPA has a much lower absorbance than vancomycin and is difficult to obtain concentrations using HPLC; however the concentrations of Gd-DTPA can be obtained from relaxivity measurements of the fluid using NMR.

In addition to delivering the same from the cement the MR and antimicrobial agents must also distribute the same in the tissue. It is possible that one agent could bind to macromolecules in the body, such as those present in serum, or bacteria, where the other agent does not. Differences in binding could mean that even if the agents would distribute similarly based on diffusion and convection, their distribution might differ because of preferential binding. To demonstrate potential differences in distribution due to binding a model was created where a low flow rate source was placed in the center of a circle and two different diffusion coefficients were given to two molecules within that space. All other parameters of the model are the same as the parameters demonstrated in chapter 6. One molecule was given a diffusion coefficient of $6x10^{-12}$ m^2/s (the diffusion coefficient of gentamicin in alginate)[23] and the other a diffusion coefficient of $12x10^{-12}$ m^2/s (twice as high as gentamicin ~Gd-DTPA). When the simulation is run with both convection and diffusion there is very little difference in the concentration distributions (Fig 7.5a,b); however, when a small section near the source is modeled as reacting with one of the molecules, such as the molecules binding to bacteria, the distribution of one of the molecules is different from the other (Fig 7.5c,d). This is model is not based on realistic parameters, it is simply meant to demonstrate a potential reason for the distribution of antimicrobials and Gd-DPTA to differ significantly. To obtain realistic parameters *in vitro* agar gels could be used to image the distribution of a fluorescent

antimicrobial, such a tetracycline [137], and Gd-DTPA over time with and without the presence of bacteria.

For a more complex but clinically relevant model, Gd-DTPA and a fluorescent antimicrobial could be co-delivered in a rabbit model using the same surgical procedures described in chapters 2-4. Then one of two procedures could be used to determine if the antimicrobial is in the same location as the Gd-DTPA seen in the MR images. First a series of biopsies could be taken near the implant the and the concentrations of antimicrobials in those biopsies could be determined. This method is limited in spatial resolution to the number of biopsies taken and is very time consuming, however is comparable to the methods used to obtain antimicrobial distributions *in vivo* prior to the development of the imaging method. Alternatively, the animal could be euthanized and perfused with fixative. Then the tissue could be embedded in resin and tissue slices could be obtained. The slices could be imaged to determine the distribution of the fluorescent antimicrobial. Histological slices are limited in temporal resolution as the animal must be euthanized.

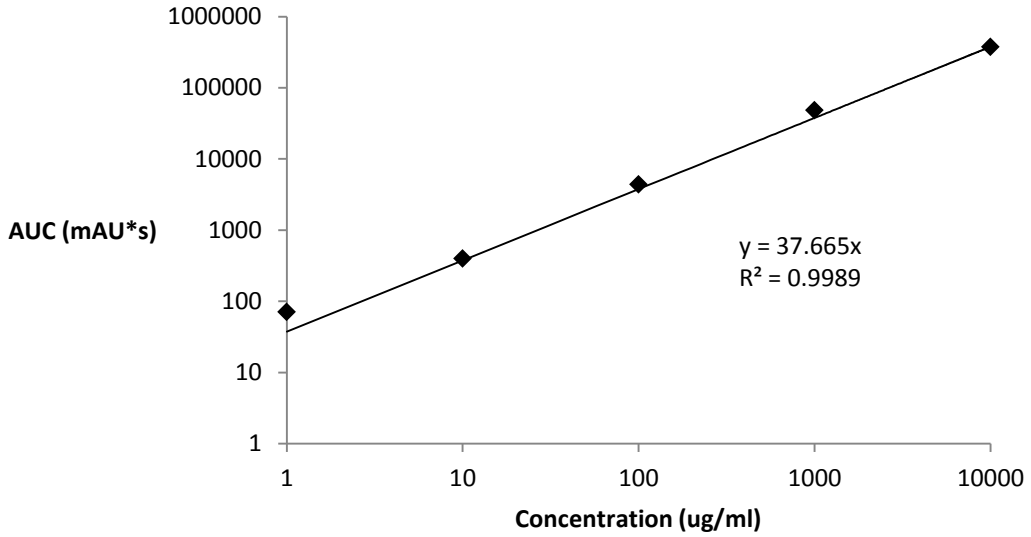

Figure 7.3: Concentration vs. area under the absorbance curve for vancomycin run on an HPLC.

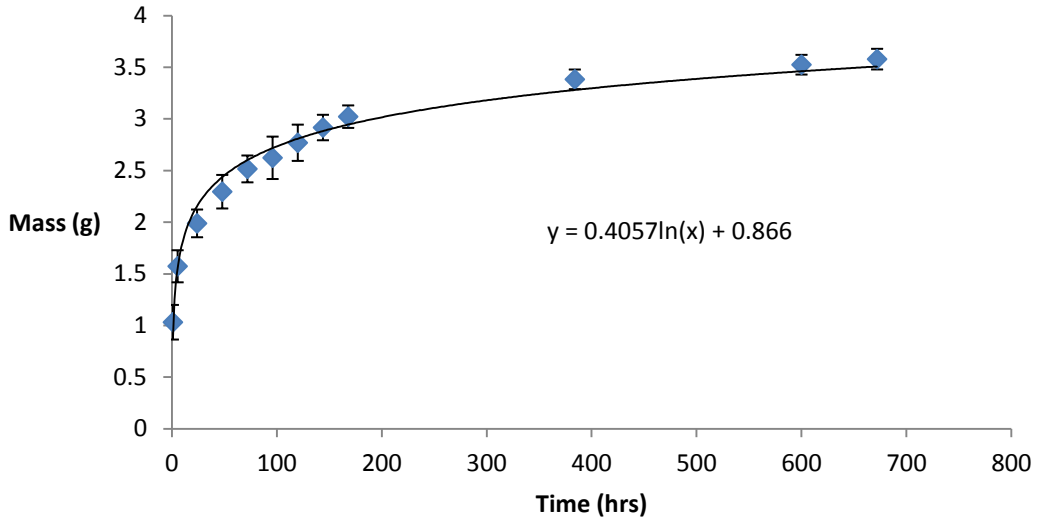

Figure 7.4: Elution profile of vancomycin from bone cement.

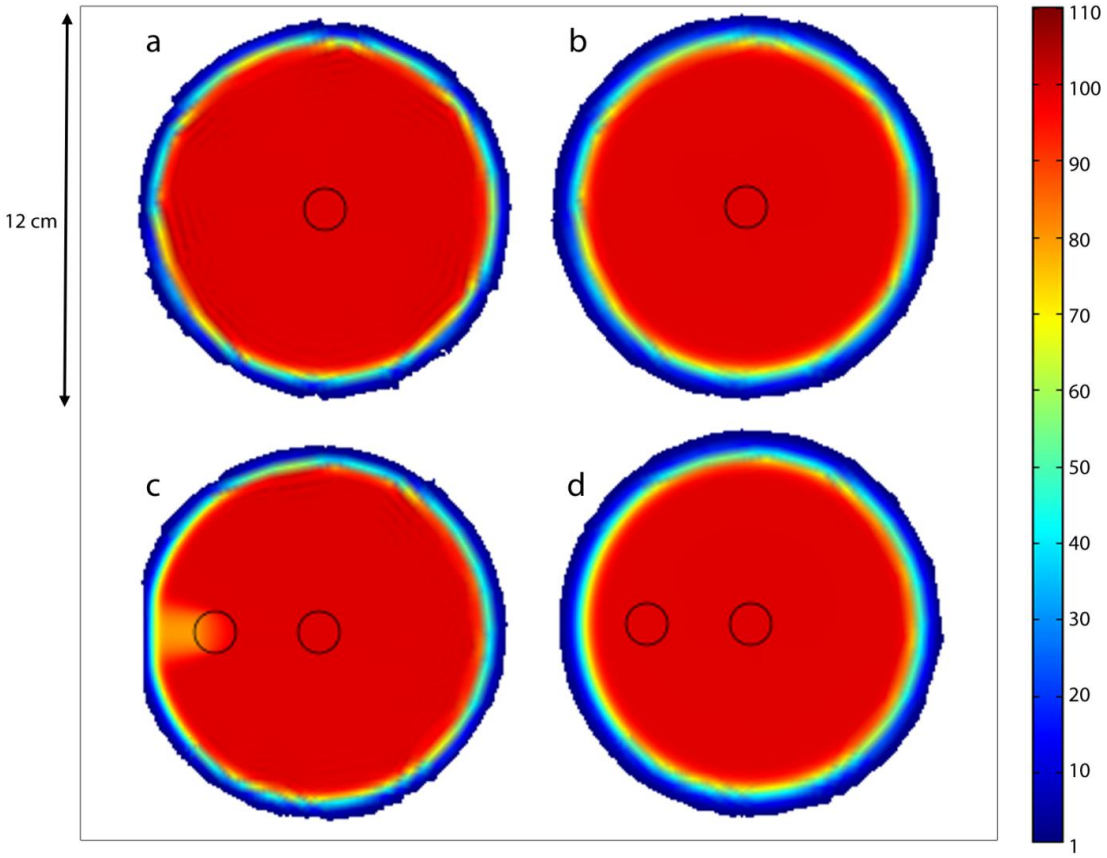

Figure 7.5: COMSOL model at 19 hours of (a) gentamicin distribution (b) Gd-DTPA distribution (c) gentamicin distribution in the presence of a region where gentamicin is bound and (d) Gd-DTPA distribution in the presence of a region where gentamicin is bound.

7.3 Imaging an Active Antimicrobial Agent

In order to visualize an active antimicrobial agent and not a surrogate one of the conjugates shown in chapter 5 could be used. Before using this agent the chelated conjugate would need to be purified and several other tests performed. I would need to test for biological and MRI activity. It is hypothesized that both the biological activity and MRI activity would be maintained because of previous studies by other groups

[67,122,123,127]. If a completely pure conjugate cannot be obtained this team could use a high yield mixture of the product as long as the yield is sufficient (~70) and little to no Gd-DOTA is present in the sample. It would also still be possible to determine the biological and MR activity using that unpurified sample. The same methods used in chapter 2-4 could be applied using a conjugated antimicrobial in place of an MRI contrast agent alone. The concentration calculation would be modified to use a relaxivity constant unique to the chelated antimicrobial.

7.4 Imaging Drug Distribution in the Presence of an Active Infection

Previously drugs distributing into orthopaedic wounds were imaged, but drug distribution in the presence of an active infection where biofilm was present has not been investigated. Biofilm has transport properties unique from normal tissue. The different transport properties could affect the distribution of antimicrobials. To study the changes in distribution when biofilm is present bone cement seeded with bacteria could be implanted into one of the previously used surgical wound models in a rabbit, partial thickness muscle removal model or full thickness muscle and bone removal model. Once an infection has been established a surgery could be performed to replace the bone cement with ABLC containing either the conjugated antimicrobial or a mixture of Gd-DTPA and antimicrobial. If a fluorescent antimicrobial were used histology could be performed similar to what was described in section 7.2. Additional histology could be performed to stain for biofilm as well, which would allow for visualization of the antimicrobial within the biofilm. Alternatively, predictions of prognosis could be made based on the MR images, the ABLC could be allowed to treat the infection, and the actual

recovery rate could be determined similar to other clinical outcome studies. A prediction study could be used to evaluate the usefulness of the method as a clinical diagnostic tool. Such a study would, however, require a large number of replicates.

In order to determine the transport properties within biofilm, several simple in vitro experiments could be performed. A fluorescent antimicrobial, such as tetracycline, could be applied to a well in the center of a biofilm and the distance of the antimicrobial from the well over time could be measured using simple fluorescent microscopy or possibly photography. The distance traveled over time would yield a diffusion coefficient of that antimicrobial in the biofilm. Similar experiments have been performed using more expensive MRI images for a phototropic biofilm [138]. Those authors posited that the diffusion coefficient they obtained, which was unrealistically fast, also incorporated convection. In order to obtain a permeability constant back pressure could be applied to the central well and images could be taken to track the progress of the antimicrobial. These data could be fit with an equation that included convection and diffusion in order to obtain the permeability constant.

The realistic transport parameters obtained from the in vitro experiments could be used as parameters in mathematical models of antimicrobial distribution in an infected animal. The models could be compared to the MR images of contrast distribution in an infected.

7.5 Mathematical Modeling of Local Drug Delivery Vehicles

It is also of interest to model drug release kinetics from PMMA bone cement. PMMA itself is not permeable to water. So three steps are involved in the delivery of

drugs from a PMMA delivery vehicle. Water must hydrate the pores near the antimicrobial or other porogen. Then the solute must dissolve. Finally, the solute must leave the cement. Modeling of these parameters could help to determine what the rate limiting steps in the elution process are and guide methods of tailoring cement compositions to obtain the desired release characteristics based on interconnectivity or pores, pore size, and solute loading. The modeled data could be compared to elution profiles obtained under near infinite sink conditions.

7.6 Conclusion

This dissertation represents a body of work that establishes a new method for characterization local drug delivery depots and quantification of distributions *in vivo*. This work demonstrates a synergy between drug delivery, imaging, and modeling that produces a comprehensive method for studying drug delivery problems *in vivo.*

In this work local drug delivery was visualized in minimally wounded tissue as well as large orthopaedic surgical wounds using MRI. It was found that it was possible to visualize contrast agent distribution in near real time using a non invasive technique that is translatable to human patients. It was possible to quantify the distribution and use it to draw conclusions about local drug delivery in musculoskeletal sites. It was found that the antimicrobial surrogate did not distribute far from the local delivery vehicle, but remained mostly within the wound space. Antimicrobial were repeatedly visualized distributing down paths of least resistance to fluid flow. A mathematical modeled of this behavior found that fluid flowing from the wound site, such as edema, could be responsible for the distributions seen in the images. It was also found that drug

distribution is likely a convective and diffusive process. These methods could be used as a clinical tool to evaluate patient treatment on a patient specific basis.

REFERENCES

1.Sterling GJ, Crawford S, Potter JH, Koerbin G, Crawford R. The pharmacokinetics of Simplex-tobramycin bone cement. J Bone Joint Surg Br 2003;85:646-9.

2.Adams K, Couch L, Cierny G, Calhoun J, Mader JT. In vitro and in vivo evaluation of antibiotic diffusion from antibiotic-impregnated polymethylmethacrylate beads. Clinical Orthopaedics and Related Research 1992;278:244-52.

3.Wolinsky JB, Colson YL, Grinstaff MW. Local drug delivery strategies for cancer treatment: Gels, nanoparticles, polymeric films, rods, and wafers. Journal of Controlled Release 2012;159:14-26.

4.Coluzzi F, Mattia C. OROS hydromorphone in chronic pain management: when drug delivery technology matches clinical needs. Minerva Anestesiol 2010;76:1072-84.

5.Hurlbert R, Theodore N, Drabier J, Magwood A, Sonntag V. A prospective randomized double-blind controlled trial to evaluate the efficacy of an analgesic epidural paste following lumbar decompressive surgery. J Neurosurg 1999;90:191-7.

6. Ladewig K. Drug delivery in soft tissue engineering. Expert Opin Drug Deliv 2011;8:1175-88.

7. Dunbar MJ. Antibiotic bone cements: their use in routine primary total joint arthroplasty is justified. Orthopedics 2009;32.

8.Jorgensen LG, Sorensen TS, Lorentzen JE. Clinical and pharmacokinetic evaluation of gentamycin containing collagen in groin wound infections after vascular reconstruction. Eur J Vasc Surg 1991;5:87-91.

9.Zilberman M, Elsner JJ. Antibiotic-eluting medical devices for various applications. Journal of Controlled Release 2008;130:202-15.

10.Penner MJ, Duncan CP, Masri BA. The in vitro elution characteristics of antibiotic-loaded CMW and Palacos-R bone cements. J Arthroplasty 1999;14:209-14.

11.Anagnostakos K, Fürst O, Kelm J. Antibiotic-impregnated PMMA hip spacers: Current status. Acta Orthop 2006;77:628-37.

12.The Diagnosis of Periprosthetic Joint Infection of the Hip and Knee: Guideline and Evidence Report. Rosemont, IL: American Academy of Orthopaedic Surgeons; 2010.

13.Blam OG, Vaccaro AR, Vanichkachorn JS, et al. Risk Factors for Surgical Site Infection in the Patient With Spinal Injury. Surgery 2003;28:1475-80.

14.Buchholz HW, Elson RA, Engelbrecht E, Lodenkämper H, Röttger J, Siegel A. Management of Deep Infection of Total Hip Replacement. Journal of Bone and Joint Surgery 1981;63-B:342-53.

15.Hsu CS, Hsu CC, Wang JW, Lin PC. Two-stage revision of infected total knee arthroplasty using an antibiotic-impregnated static cement-spacer. Chang Gung Med J 2008;31:583-91.

16.Darouiche RO. Treatment of Infections Associated with Surgical Implants. New England Journal of Medicine 2004;350:1422-9.

17.Parvizi J, Pawasarat IM, Azzam KA, Joshi A, Hansen EN, Bozic KJ. Periprosthetic Joint Infection: The Economic Impact of Methicillin-Resistant Infections. Journal of Arthroplasty 2010;25:103-7.

18.Kurtz S, Ong K, Lau E, Mowat F, Halpern M. Projections of Primary and Revision Hip and Knee Arthroplasty in the United States from 2005 to 2030. Journal of Bone and Joint Surgery 2007;89:780-5.

19.Kolter T, Greenberg EP. Microbial sciences: the superficial life of microbes. Nature 2006;441:300-2.

20. Jesaitis AJ, Franklin MJ, Berglund D, et al. Comprimised host defense on *Pseudomonas aeruginosa* biofilms: characterization of neutrophil and biofilm interactions. The journal of Immunology 2003;171:4329-39.

21.Otto M. Bacterial sensing of antimicrobial peptides. Contrib Microbiol 2009;16:136-49.

22.Stewart PS, Costerton JW. Antibiotic resistance of bacteria in biofilms. The Lancet 2001;358:135-8.

23.Gordon CA. Use of Slime Dispersants To Promote Antibiotic Penetration through the Extracellular Polysaccharide of Mucoid *Pseudomonas aeruginosa*. Antimicrobial Agents and Chemotherapy 1991;35:1258-60.

24.Nichols WW, Dorrington SM, Slack MP, Walmsley HL. Inhibition of tobramycin diffusion by binding to alginate. Antimicrobial Agents and Chemotherapy 1988;32:518-23.

25.Ceri H, Olson ME, Stremick C, Read RR, Morck D, Buret A. The Calgary Biofilm Device: New Technology for Rapid Determination of Antibiotic Susceptibilities of Bacterial Biofilms. Journal of Clinical Microbiology 1999;37:1771-6.

26.Diefenbeck M, Mückley T, Hofmann GO. Prophylaxis and treatment of implant related infections by local application of antibiotics. Injury 2006;37:S95-S104.

27.Anwar H, Biesen Tv, Dasgupta M, Lam K, Costerton JW. Interaction of biofilm bacteria with antibiotics in a novel in vitro chemostat system. Antimicrobial Agents and Chemotherapy 1989;33:1824-6.

28.Williams I, Venables WA, Lloyd D, Paul F, Critchley I. The effects of adherence to silicone surfaces on antibiotic susceptibility in Staphylococcus aureus. Microbiology 1997;143:2407-13.

29.Raad I, Hanna H, Jiang Y, et al. Low concentrations of vancomycin stimulate biofilm formation in some clinical isolates of Staphylococcus epidermidis. Antimicrobial Agents and Chemotherapy 2007;51:1656-60.

30.Kaplan JB. Antibiotic-induced biofilm formation. Int J Artif Organs 2011;34:737-51.

31.Jiranek WA, Hanssen AD, Greenwald AS. Antibiotic-Loaded Bone Cement for Infection Prophylaxis in Total Joint Replacement. The Journal of Bone and Joint Surgery 2006;88:2487-500.

32.Sanchez-Sotelo J, Berry DJ, Hanssen AD, Cabanela ME. Midterm to long-term followup of staged reimplantation for infected hip arthroplasty. Clinical Orthopaedics and Related Research 2009;467:219-24.

33.Shen H, Wang QJ, Zhang XL, et al. Cementless two-staged total hip arthroplasty for chronic periprosthetic infection. Zhonghua Wai Ke Za Zhi 2012;50:402-6.

34.Tigani D, Trisolino G, Fosco M, Avad RB, Costigliola P. Two-stage reimplantation fo periprosthetic knee infection: Influence of host health status and infecting microorganisms. Knee 2013;20:9-18.

35.Moyad TF, Thornhill T, Estok D. Evaluation and management of the infected total hip and knee. Orthopaedics 2008;31:581-8.

36.Gristina AG, Costerton JW. Bacterial Adherence to Biomaterials and Tissue. The Journal of Bone and Joint Surgery 1985;67-A:264-73.

37.Orthopaedics S. OR Handbook for Simplex P Bone Cement. In: Orthopaedics S, ed. Mahwah, NJ: Stryker Orthopaedics; 2007.

38.Nussbaum DA, Gailloud P, Murphy K. The chemistry of acrylic bone cements and implications for clinical use in image-guided therapy. Journal of vascular and interventional radiology 2004;15:121-6.

39.Schnieders J. Controlled release of gentamicin from calcium phosphatepoly(lactic acid-co-glycolic acid) composite bone cement. Biomaterials 2006;27:4239-49.

40.Armstrong MS. Mechanical characteristics of antibiotic-laden bone cement. Acta Orthop Scand 2002;73:688-90.

41.Diez-Pena E. Gentamicin sulphate release from a modified commercial acrylic surgical radiopaque bone cement. chem Pharm Bull 2002;50:1201-8.

42.Levin PD. The effectiveness of various antibiotics in methyl methacrylate. Joint Surgery 1975;57:234-7.

43.Miclau T, Dahners LE, Lindsey RW, JOR. In vitro pharmacokinetics of antibiotic release from locally implantable materials. Journal of Orthopaedic Research 1993;11:627-32.

44. DiMaio FR, O'Halloran JJ, Quale J. In vitro elution of ciprofloxacin from polymethylmethacrylate cement beads. Journal of Orthopaedic Research 1994;12:79-82.

45.Bunetel L. Release of gentamicin from acrylic bone cement. Clinical Pharmacology 1989;17:291-7.

46.McLaren AC, Nugent M, Economopoulos K, Kaul H, Vernon BL, McLemore R. Hand-mixed and Premixed Antibiotic-loaded Bone Cement Have Similar Homogeneity. Clinical Orthopaedics and Related Research 2009;467:1693–8.

47.Klekamp J, Dawson JM, Haas DW, DeBoer D, Christie M. The Use of Vancomycin and Tobramycin in Acrylic Bone Cement: Biomechanical Effects and Elution Kinetics for Use in Joint Arthroplasty. The Journal of Arthroplasty 1999;14:339-46.

48.Lewis G, Janna S. Estimation of the optimum loading of an antibiotic powder in an acrylic bone cement. Acta Orthop 2006;77:622-7.

49.Rasyid HN, van der Mei HC, Frijink HW, et al. Concepts for increasing gentamicin release from handmade bone cement beads. Acta Orthopaedica 2009;80:508-13.

50.Buchholz HW, Engelbrecht H. Uber die Depotwirkung einiger Antibiotica bei Vermischung mit dem Kunstharz Palacos. Chirurg 1970;41:511-5.

51.Fernández-Seara MA, Wehrli SL, Wehrli FW. Diffusion of Exchangeable Water in Cortical Bone Studied by Nuclear Magnetic Resonance. Biophysical Journal 2002;82:522-9.

52.Cleveland GG, Chang DC, Hazlewood CF, Rorschach HE. Nuclear magnetic resonance measurement of skeletal muscle: anisotrophy of the diffusion coefficient of the intracellular water. Biophysical Journal 1976;16:1043-53.

53.Nijhof MW, Dhert WJA, Tilman PBJ, Verbout AJ. Release of tobramycin from tobramycin-containing bone cement in bone and serum of rabbits. Journal of Materials Science: Materials in Medicine 1997;8:799-802.

54.Masri BA, Duncan CP, Beauchamp CP. Long-term elution of antibiotics from bone-cement: an in vivo study using the prosthesis of antibiotic-loaded acrylic cement (PROSTALAC) system. Journal of Arthroplasty 1998;13:331-8.

55.Brien WW, Salvati EA, Klein R, Brause B, Stern S. Antibiotic Impregnated bone cement in total hip arthroplasty. Clinical Orthopaedics and Related Research 1993;298:242-8.

56.Marks KE, Nelson CL, Lautenschlager EP. Antibiotic-impregnated acrylic bone cement. Journal of Bone and Joint Surgery 1976;58:358-64.

57.Smilack JD, Flittie WH, Willliams TW. Bone concentrations of antimicrobial agents after parenteral administration. Antimicrobial Agents and Chemotherapy 1976;9:169-71.

58. Cierny G, III, , DiPasquale D. Periprosthetic Total Joint Infections. Clinical Orthopaedics and Related Research 2002;403:23-8.

59.Walenkamp GH, Kleijin LL, Leeuw Md. Osteomyelitis treated with gentamicin-PMMA beads: 100 patients followed for 1–12 years. Acta Orthop Scand 1998;69:518-22.

60.Hendriks JGE, Horn JRv, Mei HCvd, Busscher HJ. Backgrounds of antibiotic-loaded bone cement and prosthesis-related infection. Biomaterials 2004;25:545-56.

61.Buchholz HW, Elson RA, Heinert K. Antibiotic-loaded acrylic cementcurrent concepts. Clinical Orthopaedics 1984;190:96-180.

62.Springer BD, Lee G-C, Osmon D, Haidukewych GJ, Hanssen AD, Jocofsky D. Systemic safety of high-dose antibiotic-loaded cement spacers after resection of an infected total knee arthroplasty. Clinical Orthopaedics and Related Research 2004;427:47-51.

63.Haacke EM, Brown RW, Thompson MR, Venkatesan R. Magnetic Resonance Imaging: Physical Principles and Sequence Design. 1st ed. ed: Wiley-Liss; 1999.

64.Smith RC, Lange RC. Understanding Magnetic Resonance Imaging. Boca Raton, FL: CRC Press LLC; 1998.

65.Frakes DH, Dasi LP, Pekkan K, et al. A New Method for Registration-Based Medical Image Interpolation. IEEE Transactions on Medical Imaging 2008;27:370-7.

66.Spencer AJ, Wilson SA, Batchelor J, Reid A, Rees J, Harpur E. Gadolinium Chloride Toxicity in the Rat. Toxicologic Pathology 1997;25:245-55.

67.Caravan P, Ellison JJ, McMurry TJ, Lauffer RB. Gadolinium (III) chelates as MRI contrast agents: Structure, dynamics, and applications. Chemical Reviews 1999;99:2293-352.

68.Stanisz GJ, Henkelman RM. Gd-DTPA Relaxivity Depends on Macromolecular Content. Magnetic Resonance in Medicine 2000;44:665-7.

69.Noordin S, Winalski CS, Shortkroff S, Mulkern RV. Factors affecting paramagnetic contrast enhancement in synovial fluid: effects of electrolytes, protein concentrations, and temperature on water proton relaxivities from Mn ions and Gd chelated contrast agents. Osteoarthritis and Cartilage 2010;18:964-70.

70.Rohrer M, Bauer H, Mintorovitch J, Requardt M, Weinmann H-J. Comparison of Magnetic Properties of MRI Contrast Media Solutions at Different Magnetic Field Strengths. Investigative Radiology 2005;40:715-24.

71.Fleckenstein JL, Canby RC, Parkey RW, Peshock RM. Acute Effects of Exercise on MR Imaging of Skeletal Muscle in Normal Volunteers. AJIR 1988;151:231-7.

72. Prantner AM, Sharma V, Garbow JR, Piwnica-Worms D. Synthesis and characterization of a Gd-DOTA-D-permeation peptide for magnetic resonance relaxation enhancement of intracellular targets. Mol Imaging 2003;2:333-41.

73.Donahue KM, Burstein D, Manning WJ, Gray ML. Studies of Gd-DTPA relaxivity and proton exchange rates in tissue. Magnetic Resonance in Medicine 2005;32:66-76.

74.Strich G, Hagan PL, Gerber KH, Slutsky RA. Tissue distribution and magnetic resonance spin lattice relaxation effects of gadolinium-DTPA. Radiology 1985;154:723-6.

75.Astary GW, Kantorovich S, Carney PR, Mareci TH, Sarntinoranont M. Regional convection-enhanced delivery of gadolinium-labeled albumin in the rat hippocampus in vivo. Journal of Neuroscience Methods 2010;187:129-37.

76.Raghavan R, Brady ML, Rodríguez-Ponce MI, Hartlep A, Pedain C, Sampson JH. Convection-enhanced delivery of therapeutics for brain disease, and its optimization. Neurosurg Focus 2006;20:1-13.

77.Sampson JH, Raghavan R, Brady ML, et al. Clinical utility of a patient-specific algorithm for simulating intracerebral drug infusions. Neuro-oncology 2007;9:343-53.

78.Krauze MT, Forsayeth J, Park JW, Bankiewicz KS. Successful and safe perfusion of the primate brainstem: in vivo magnetic resonance imaging of macromolecular distribution during infusion. Pharmaceutical Research 2006;23:2493-504.

79.Magdoom KN, Pishko GL, Kim JH, Sarntinoranont M. Evaluation of a Voxelized Model Based on DCE-MRI for Tracer Transport in Tumor. Journal of Biomechanical Engineering 2012;134.

80.Chen X, Astary GW, Sepulveda H, Mareci TH, Sarntinoranont M. Quantitative assessment of macromolecular concentration during direct infusion into an agarose hydrogel phantom using contrast-enhanced MRI. Magnetic Resonance Imaging 2008;26:1433-41.

81.Xu F, Han H, Zhang H, Pi J, Fu Y. Quantification of Gd-DTPA concentration in neuroimaging using T1 3D MP-RAGE sequence at 3.0 T. Magnetic Resonance Imaging 2011;29:827-34.

82.Hittmair K, Gomiscek G, Langenberger K, Recht M, Imhof H, Kramer J. Method for the quantitative assessment of contrast agent uptake in dynamic contrast-enhanced MRI. Magnetic Resonance in Medicine 2005;31:567-71.

83.Bokacheva L, Rusinek H, Chen Q, et al. Quantitative Determination of Gd-DTPA Concentration in T1-Weighted MR Renography Studies. Magnetic Resonance in Medicine 2007;57:1012-8.

84.Morkenborg J, Pedersen M, Jensen FT, Stodkilde-Jorgensen H, Djurhuus JC, Frokiaer J. Quantitative assessment of Gd-DTPA contrast agent from signal enhancement an in-vitro study. Magnetic Resonance Imaging 2003;21:637-43.

85. Port RE, Schuster C, Port CR, Bachert P. Simultaneous sustained release of fludarabine monophosphate and Gd-DTPA from an interstitial liposome depot in rats: potential for indirect monitoring of drug release by magnetic resonance imaging. Cancer Chemother Pharmacol 2006;58:607-17.

86.Fritz-Hansen T, Rostrup E, Larsson HB, Sandergaard L, Ring P, Henriksen O. Measurement of the Arterial Concentration of Gd-DTPA Using MRI: A Step Toward Quantitative Perfusion Imaging. Magnetic Resonance in Medicine 2005;36:225-31.

87.Kim H, Robinson MR, Lizak MJ, et al. Controlled Drug Release from an Ocular Implant: An Evaluation Using Dynamic Three-Dimensional Magnetic Resonance Imaging. Investigative Ophthalmology & Visual Science 2004;45:2722-31.

88.Truskey GA, Yuan F, Katz DF. Transport Phenomena in Biological Systems. Upper Saddle River, New Jersey: Pearson Education, Inc.; 2004.

89.Foy BD, Blake J. Diffusion of Paramagnetically Labeled Proteins in Cartilage: Enhancement of the 1-D NMR Imaging Technique. Journal of Magnetic Resonance Imaging 2001;148:126-34.

90.Bleicher K, Lin M, Shapiro MJ, Wareing JR. Diffusion Edited NMR: Screening Compound Mixtures by Affinity NMR to Detect Binding Ligands to Vancomycin. J Org Chem 1998;63:8486-90.

91.Khaled ARA, Vafai K. The role of porous media in modeling flow and heat transfer in biological tissues. International Journal of Heat and Mass Transfer 2003;46:4989-5003.

92.Levick JR. Flow through interstitium and other fibrous matrices. Quarterly Journal of Experimental Physiology 1987;72:409-38.

93.Murata T. Theoretical analysis of transcapillary fluid exchange: the effects of filtration coefficient and lymph flow on fluid exchange. Microvascular research 1978;16:237-62.

94.Monaco JL, Lawrence T. Acute wound healing: an overview. Clinical Plastic Surgery 2003;30:1-12.

95.Hanssen AD, Spangehl MJ. Practical applications of antibiotic-loaded bone cement for treatment of infected joint replacements. Clinical Orthopaedics and Related Research 2004;427:79-85.

96.Saginur R, St. Denis M, Ferris W, et al. Multiple combination bactericidal testing of staphylococcal biofilms from implant-associated infections. Antimicrobial Agents and Chemotherapy 2006;50:55-61.

97.Hanssen AD. Local antibiotic delivery vehicles in the treatment of musculoskeletal infection. Clinical Orthopaedics and Related Research 2005;437:91-6.

98.Nugent M, McLaren A, Vernon B, McLemore R. Strength of Antimicrobial Bone Cement Decreases with Increased Poragen Fraction. Clinical Orthopaedics and Related Research 2010;468:2101-6.

99.Giers MB, Estes CS, McLaren AC, Caplan MR, McLemore RL. Jeannette Wilkins Award: Can Locally Delivered Gadolinium Be Visualized on MRI? A Pilot Study. Clinical Orthopaedics and Related Research 2012;470:2654-62.

100.Lin L-K. Assay validation using the concordance correlation coefficient. Biometrics 1992;48:599-604.

101.Armitage P, Berry G, Matthews J. Statistical Methods in Medical Research. Hoboken, NJ, USA: Wiley-Blackwell; 2001.

102.Bland J, Altman D. Statitical methods for assessing agreement between two methods of clinical measurement. Lancet 1986;1:307-10.

103.Owen K, Nicholas R, Hickmon S, Skinner R, Stewart C, Nelson C. Antibiotic penetration of avascular bone. Orthopaedic Transactions 1994;18.

104.Nelson CL, Hickmon SG, Skinner RA. Treatment of Experimental Osteomyelitis by Surgical Debridement and the Implantation of Bioerodable, Polyanhydride-Gentamicin Beads. Journal of Orthopaedic Research 1997;15:249-55.

105.Giers MB, McLaren AC, Plasencia JD, Frakes D, McLemore R, Caplan MR. Spatiotemporal Quantification of Local Drug Delivery Using MRI. Computational and Mathmatical Methods in Medicine 2013;Accepted.

106.Giers MB, McLaren AC, Caplan MR, McLemore R. Magnetic Resonance Imaging of the Distribution Patterns of Locally Delivered Gadolinium in Orthopaedic Wounds. Submitted 2013.

107.Karasev P, Kolesov I, Chudy K, Tannenbaum A, Muller G, Xerogeanes J. Interactive MRI Segmentation with Controlled Active Vision. 50th IEEE Conference on Decision and Control and European Control Conference 2011.

108.Eggert DW, Lorusso A, Fisher RB. Estimating 3-D rigid body transformations: a comparison of four major algorithms. Machine Vision and Applications 1997;9:272-90.

109.Zhuang X, Arridge S, Hawkes DJ, Ourselin S. A Nonrigid Registration Framework Using Spatially Encoded Mutual Information and Free-Form Deformations. IEEE Transactions on Medical Imaging 2011;30:1819 - 28.

110.Boehler T, Zoehrer F, Harz M, Hahn HK. Breast image registration and deformation modeling. In: Crit Rev Biomed Eng; 2012:235-58.

111.Loeckx D, Slagmolen P, Maes F, Vandermeulen D, Suetens P. Nonrigid Image Registration Using Conditional Mutual Information. IEEE Transactions on Medical Imaging 2010;29:19-29.

112.Rueckert D, Sonoda LI, Hayes C, Hill DLG, Leach MO, Hawkes DJ. Nonrigid Registration Using Free-Form Deformations: Application to Breast MR Images. IEEE Transactions on Medical Imaging 1999;18:712-21.

113.Zhe L, Deng D, Guang-Zhi W. Accuracy validation for medical image registration algorithms: a review. Chin Med Sci J 2012;27:176-81.

114.Gordon MJ, Chu KC, Margaritis A, Martin AJ, Ethier CR, Rutt BK. Measurement of Gd-DTPA Diffusion Though PVA Hydrogel using a Novel Magnetic Resonance Imaging Method. Biotechnology and Bioengineering 1999;65:459-67.

115.Boselli E, Breih D, Djabarouti S, Bel JC, Saux MC, Allaouchiche B. Diffusion of ertapenem into bone and synovial tissues. Journal of Antimicrobial Cheotherapy 2007;60:893-6.

116.Napier N, Shortt C, Eustace S. Muscle Edema: Classification , Mechanisms, and Interpretation. Seminars in Musculoskeletal Radiology 2006;10:258-67.

117.De León-Rodríguez LM, Ortiz A, Weiner AL, et al. Magnetic resonance imaging detects a specific peptide-protein binding event. J Am Chem Soc 2002;124:3514-5.

118.Lewis MR, Raubitschek A, Shively JE. A Facile, Water-Soluble Method for Modification of Proteins with DOTA. Use of Elevated Temperature and Optimized pH To Achieve High Specific Activity and High Chelate Stability in Radiolabeled Immunoconjugates. Bioconjugate Chemistry 1994;5:565-76.

119.Lewis MR, Kao JY, Anderson A-LJ, Shively JE, Raubitschek A. An Improved Method for Conjugating Monoclonal Antibodies with N-Hydroxysulfosuccinimidyl DOTA. Bioconjugate Chemistry 2001;12:320-4.

120.Nakajima N, Ikada Y. Mechanism of Amide Formation by Carbodiimide for Bioconjugation in Aqueous Media. Bioconjugate Chemistry 1995;6:123-30.

121.Stile RA, Healy KE. Thermo-Responsive Peptide-Modified Hydrogels for Tissue Regeneration. Biomacromolecules 2001;2:185-94.

122.Prodhomme EJG, Tutt AL, Glennie MJ, Bugg TDH. Multivalent Conjugates of Poly-ç-D-glutamic Acid from Bacillus licheniformis with Antibody F(ab¢) and Glycopeptide Ligands. Bioconjugate Chemistry 2003;14:1148-55.

123.Lewis JE, Nelson JC, Elder HA. Radioimmunoassay of an Antibiotic: Gentamicin. Nature New Biology 1972;239:214-6.

124.Gilles MA, Hudson AQ, Borders CL. Stability of water-soluble carbodiimides in aquesous solution. Anal Biochem 1990;184:244-8.

125.Dumont MF, Baligand C, Li Y, et al. DNA Surface Modified Gadolinium Phosphate Nanoparticles as MRI Contrast Agents. Bioconjugate Chemistry 2012;23:951-7.

126.Barge A, Cravotto G, Gianolio E, Fedeli F. How to determine free Gd and free ligand in solution

of Gd chelates. A technical note. Contrast media & Molecular Imaging 2006;1:184-8.

127.Kadurugamuwa JL, Clarke AJ, Beveridge TJ. Surface action of gentamicin on Pseudomonas aeruginosa. Journal of Bacteriology 1993;175:5798-805.

128.Bousquet JC, Saini S, Stark DD, et al. Gd-DOTA: characterization of a new paramagnetic complex. Radiology 1988;166:693-8.

129.Costerton JW, Stewart PS, Greenberg EP. Bacterial biofilms: a common cause of persistent infections. Science 1999;284:1318-22.

130.Otto M. Bacterial evasion of antimicrobial peptides by biofilm formation. Antimicrobial Peptides and Human Disease 2006;206:251-8.

131.Mills R. Self-Diffusion in Normal and Heavy Water in the Range 1-45^{o}. The Journal of Physical Chemistry 1973;77:685-8.

132.Kim JH, Astary GW, Kantorovich S, Mareci TH, Carney PR, Sarntinoranont M. Voxelized Computational Model for Convection-Enhanced Delivery in the Rat Ventral Hippocampus: Comparison with In Vivo MR Experimental Studies. Annals of Biomedical Engineering 2012;40:2043-58.

133.Kim JH, Mareci TH, Sarntinoranont M. A voxelized model of direct infusion into the corpus callosum and hippocampus of the rat brain: model development and parameter analysis. Med Biol Eng Comput 2010;48:203-14.

134.Lee SJ, Pishko GL, Astary GW, Mareci TH, Sarntinoranont M. Sensitivity Analysis of an Image-Based Solid Tumor Computational Model with Heterogeneous Vasculature and Porosity. J Appl Polym Sci Symp 2009;114:1992-2002.

135.Pishko GL, Astary GW, Mareci TH, Sarntinoranont M. Sensitivity Analysis of an Image-Based Solid Tumor Computational Model with Heterogeneous Vasculature and Porosity. Annals of Biomedical Engineering 2011;39:2360-73.

136.Vogelman B, Craig WA. Kinetics of antimicrobial activity. Journal of Pediatrics 1986;108:835-40.

137. Schneider S, Schmitt MO, Brehm G, Reiher M, Matousek P, Towrie M. Fluorescence kinetics of aqueous solutions of tetracycline and itscomplexes with Mg2+ and Ca2+. Photochem Photobiol Sci 2003;2.

138.Ramanan B, Holmes WM, Sloan WT, Phoenix VR. Magnetic Resonance Imaging of Mass Transport and Structure Inside a Phototrophic Biofilm. Current Microbiology 2013;Published Online.

APPENDIX A

MATLAB CODE

A.1 UnstacktifT1wandT1

```
%This is an IO file that reads in a stack of T1 maps and T1 weighted images
%as an hdr and exports unstacked tif images and saves them.
%Prior to exporting the images it processes them to remove noise.
originalimage=readdata3d;                                   %GUI to import hdr
downloadable from the MATLAB website.
originalimaget1w=readdata3d;
originalimage=double(originalimage);                        %Changes matrix type to
double.
[xo yo zo]=size(originalimage);                             %Finds the size of the matrix
timepoint=input('input the timepoint chosen: ')             %Choose what the timepoint
was so that it is entered into the filename
originalimage=originalimage(:,:,3:5:end-2);                 %Indexes out all the extra
slices containing standard deviation, etc. to leave only the actual map slices
[x y z]=size(originalimage);
[x1 y1 z1]=size(originalimaget1w);
originalimaget1w=originalimaget1w(:,:,1:z);                 %Shortens matrix to only
include the first set of images taken at the same TR value
top=6000;                                                   %A cut off point where
above that value in the map images most pixels are noise
topw=1500000;                                               %A cut off point where
above that value in the weighted images most pixels are noise
[originalimagecutt1w]=cutoff(originalimaget1w,topw);
```

```
[originalimagecut]=cutoff(originalimage,top);                %Cuts off above the value
chosen in top.  Anything above top is made equal to top.
disp('I am restoring now')
[filteredlinear]=medianfilter(originalimagecut,5);           %Cleans some noise from the
image using a median filter
[filteredlineart1w]=medianfilter(originalimaget1w,9);        %Prepares image for
masking program
disp('I am masking now')
[mask]=masking(filteredlineart1w);                           %Creates binary mask of
where there are legs
cleaned=double(filteredlinear.*mask);                        %Removes all noise from
outside of the legs in the map image
cleanedt1w=double(originalimagecutt1w.*mask);                %Removes all noise from
outside of the legs in the weighted image
cleanedt1w=cleanedt1w*65536/1500000;                         %Adjusts scale to a value of
65536/2^16 (bitdepth of 16) which is what a tif is out of.  If you do not do this it will turn
all pixels above 2^16 into 2^16.
cleaned=uint16(cleaned);                                     %Makes sure the matrix is
recognized as uint16
cleanedt1w=uint16(cleanedt1w);
for k=1:z1
filenamet1w = sprintf('w_%d_%d.tif',timepoint,k);            %Creates a filename based
on the timepoint and the slice number
```

```
imwrite(cleanedt1w(:,:,k),filenamet1w);                    %Exports images to the
current directory folder
end
```

A.2 Cutoff

```
function [Topcleaned]=cutoff(image,cutoffpoint)
%This program turns any value in a matrix above the specified "cutoffpoint"
%into the value of the cutoff point.
[x y numslice]=size(image);                                %Determines the size of the
matrix imported
Topcleaned=zeros(x,y,numslice);                            %Creates a matrix of zeros
with the dimensions of the imported matrix
image(isnan(image))=0;                                     %Replaces any non real
numbers in the imported matrix with a value of zero
for i=1:x
   for j=1:y
      for k=1:numslice
         if image(i,j,k)>cutoffpoint
            Topcleaned(i,j,k)=cutoffpoint;                 %Replaces any values above
the cutoff point with the value of the cutoff point in the new matrix Topcleaned
         else
            Topcleaned(i,j,k)=image(i,j,k);                %Any other values remain
the same as their original value in the imported matrix
```

```
            end
        end
    end
end
```

A.3 Medianfilter

```
function [filteredlinear]=medianfilter(originalimage,degree)
%This program uses a median filter of the specified degree to remove noise
%in an image.  A median filter takes the median value from a certain number
%of surrounding pixels and itself.  The degree specifies the number of
%surounding pixels you want included (the default is 5).  A degree of 5
%will take the 4 nearest neighbor pixels and itself.
while nargin==1                                          %If no degree is specified use
a degree of 5
   degree=5;
end
[ x y z]=size(originalimage);                            %Find the dimensions of the
imported matrix
filteredlinear=zeros(x,y,z);                             %Specifies a matrix of zeros
the size of the imported matrix
for k=1:z                                                %Indexes through each slice
of the image stack and filters.  The filtered image is stored in the new matrix
filteredlinear.
```

```
    filteredlinear(:,:,k)=ordfilt2(originalimage(:,:,k),degree,ones(3,3));
end
```

A.4 Masking

```
function [mask]=masking(originalimage)
%This program turns an image binary and makes a mask.
[x y numslice]=size(originalimage);                    %Finds dimension of the
imported matrix
normalized=originalimage./max(max(max(originalimage)));%Adjusts matrix to be out of
a value of 1
Opened=zeros(x,y,numslice);                            %Creates matrix of zeros
Closed=zeros(x,y,numslice);
mask=zeros(x,y,numslice);
Binary=zeros(x,y,numslice);
SE=strel('disk',3);                                    %Creates a structure element
that is a disk shape with a radius of 3.  This is used in the following convolution
functions.
SE2=strel('disk',3);
for k=1:numslice                                       %Indexes through each slice
for the following functions that are meant for 2D images
    Opened(:,:,k)=imopen(normalized(:,:,k),SE);        %Morphologically opens the
image.
    Closed(:,:,k)=imclose(Opened(:,:,k),SE2);
```

```
   Binary(:,:,k)=im2bw(Closed(:,:,k),0.02);                    %Turns the image binary
around a certain value.  Values above change to a 1, values bellow change to a 0.
   mask(:,:,k)=imfill(Binary(:,:,k),'holes') ;                 %Fills holes in the image.  If
there are a group of 0's surrounded by 1's it will fill the 0 spots with 1's.
   mask(:,:,k)=bwareaopen(mask(:,:,k),100);                    %This removes 1's from the
binary image if they are not connected a minimum of 100 pixels.
end
```

A.5 T10estimatorwithimport

```
%This program works with the program T10estimator to import an image,
%process the image, and find the average and standard deviation of the
%histogram of that image, where the cement and contrast pixels have been
%removed. This can be correlated to the pre-contrast T1 value.
clear all
originalimage=readdata3d;                                      %GUI to import hdr
originalimaget1w=readdata3d;
originalimage=double(originalimage);
[xo yo zo]=size(originalimage);
originalimage=originalimage(:,:,3:5:end-2);                    %Indexes out all the extra
slices containing standard deviation, etc. to leave only the actual map slices
[x y z]=size(originalimage);
originalimaget1w=originalimaget1w(:,:,1:z);                    %Shortens matrix to only
include the first set of TR values
```

```
top=6000;                                                    %A cut off point where
above that value most T1 map pixels are noise
topw=1500000;                                                %A cut off point where
above that value most T1 weighted pixels are noise
[originalimagecutt1w]=cutoff(originalimaget1w,topw);
[originalimagecut]=cutoff(originalimage,top);                %Cuts off above the value
chosen in top.  Anything above top is made equal to top.
disp('I am restoring now')
[filteredlinear]=medianfilter(originalimagecut,5);           %Cleans some noise from the
image
[filteredlineart1w]=medianfilter(originalimaget1w,9);        %Prepares image for
masking program
disp('I am masking now')
[mask]=masking(filteredlineart1w);                           %Creates binary mask of
where there are legs
cleaned=double(filteredlinear.*mask);                        %Removes all noise from
outside of the legs
[frequencyalldim,Intensity,mean,standarddev]=T10estimator(cleaned,100);    %Creates a
symmetrical histogram of the image based on the top half of the histogram to remove
contrast and cement pixels, then finds the average and standard deviation of the
histogram.
disp('mean= ')
disp(mean)
```

```
disp('standard deviation= ')
disp(standarddev)
```

A.6 T10estimator

```
function [frequencyalldim,Intensity,mean,standarddev]=T10estimator(matrixname,b)
%Creates a symmetrical histogram of the image based on the top half of the
%histogram to remove contrast and cement pixels, then finds the average and
%standard deviation of the histogram.
%b is the number of bins desired
[x y numslice]=size(matrixname);
matrixname=cutoff(matrixname,6000);                    %Cuts off all matrix values
above 6000.
top=max(max(max(matrixname)));                         %Finds the maximum value
in the matrix
Intens1=zeros(b);
frequency=zeros(b,numslice);
for l=1:numslice
   [frequency(:,l) Intens1]=imhist(matrixname(:,:,l)./top,b); %Calculates a histogram for
each image slice. The scale must be from 0 to 1 so all matrix values are divided by the
top matrix value.
end
```

```
frequencyalldim=sum(frequency,2);                    %Sums the histograms for all
slices to get the 3D image histogram
frequencyalldim(1,1)=0;
frequencyalldim(b,1)=0;
Intensity=Intens1.*top;                              %Finds the intensity values
of the original image scale.
maximumfrequency=max(max(frequencyalldim));          %Finds peak histogram value
[N,M]=find(frequencyalldim==maximumfrequency);       %Finds location of peak
histogram value
frequencybackward=flipud(frequencyalldim);           %Mirrors histogram about
the peak histogram value
if N<b/2                                             %If the peak is in the first
half of the histogram copies the last part of the histogram to make symmetric and cuts off
last part of histogram
  frequencyalldim(1:N,1)=frequencybackward((b-2*N+2):(b-N+1),1);
  frequencyalldim((2*N):end)=0;
elseif N>b/2                                         %If the peak is in the second
half of the histogram copies the last part of the histogram to make symmetric then adds
zeros to any value before the histogram starts
   frequencyalldim((2*N-b):(N-1),1)=frequencybackward(1:(b-N),1);
   frequencyalldim(1:(2*N-b-1))=0;
else
   frequencyalldim(1:(N-1),1)=frequencybackward(1:(b-N-1),1);
```

```
end
mean=Intensity(N,1);                                    %Finds the mean of the
symmetric histogram, which is the peak value
SS=frequencyalldim.*(Intensity-mean).^2;                %Sum of Squares
standarddev=sqrt((1/sum(sum(frequencyalldim)))*sum(sum(SS))); %Finds the standard
deviation of the histogram
```

A.7 Mimicsimportandmapmaker

```
%This program imports a segmented contrast area mask from mimics, makes a
%concentration map and a movie.  Before running change the filename, move
%the mask images into the directory folder, and remove 0z from before single
%digit numbers.  Afterword save maskdrug,
%maskdrugrecuded Cpicture, C,
%Cement, M, and the movie in the directory.
filename='3_30_12_time31_w_left contrast tres 2145+0000'; %Enter the filenames for
the mask you are importing.
T10estimate=2788;                                       %Enter value of T10
calculated from T10estimator or use an average value from several animals, such as 2817
ms.
originalimage=readdata3d;                               %Import T1 map using GUI
originalimaget1w=readdata3d;                            %Import T1 weighted image
using GUI
```

originalimage=originalimage(:,:,3:5:(end-2)); %This indexes out the extra slices containing standard deviation, etc. and leaves only the actual map slices.

[x y z]=size(originalimage); %Finds the dimensions of the T1 map after removing extra slices.

originalimaget1w=originalimaget1w(:,:,1:z); %The T1 weighted hdr comes as a series of T1 weighted scans with different TR values. This takes only the set from the first TR value. This should match the dimensions of the T1 map.

disp('I am restoring now') %Displays the single quoted words in the command window.

[filteredlinear]=medianfilter(originalimage,5); %Runs the noise reducing filtering program medianfilter on the T1 map.

[filteredlineart1w]=medianfilter(originalimaget1w,9); %Runs the noise reducing filtering program medianfilter on the T1 weighted. This is meant to prepare this image for transform into a mask.

disp('I am masking now')

[mask]=masking(filteredlineart1w); %This runs the program masking that creates a binary mask on the legs. 1's indicate that it is a point inside the legs, 0's indicate it is a point outside the legs.

cleaned=double(filteredlinear.*mask); %multiplying the reduced noise T1 map by the binary mask removes all noise outside the legs.

cleanedt1w=originalimaget1w.*mask;

```
[maskdrug]=restack(filename,originalimaget1w);              %This runs a program that
imports a stack of masked images from mimics.  You must put the images in the
directory folder.
reducedmask=reducemask(mask,3);                             %Reduces the outside of the
mask of the leg by 3 pixels.
maskdrugreduced=maskdrug.*reducedmask;                      %Gets rid of an edge effect
on the segmented region.
[Cpicture,C,Cement]=concentration(maskdrugreduced,1,cleaned,cleanedt1w,T10estimate
);          %This creates a concentration map of the image
[M]=movierabbitconcentration(maskdrug,maskbone,1,cleanedt1w,cleaned,Cpicture);
%This creates a movie of the concentration map slices
total=sum(sum(sum(C)))*.3*.3*2/1000000;                     %This calculates the total
mmols of contrast in the image and displays it in the command window
disp('The total amount of mmols in image= ')
disp(total)
volumedrug=sum(sum(sum(maskdrugreduced)))*.3*.3*2;   %Finds the total amount of
volume of tissue with contrast above some minimum (below the threshold) level.
disp('The total volume of contrast in mm3= ')
disp(volumedrug)
volumecement=sum(sum(sum(Cement)))*.3*.3*2;                 %Finds the total amount of
volume of tissue with contrast above some minimum level.
disp('The total volume of cement in mm3= ')
disp(volumecement)
```

A.8 Restack

```
function [maskimport]=restack(filename, originalimaget1w)
%this function is meant to import a stack of bmp images from mimics, find
%the segmented mask region, and export a binary matrix of the mask.  The
%mask must be in color (not black and white).  To import the mask put the
%mask images in the directory folder.  The images before 10 must have a 0
%removed before the unique number.
[x,y,z]=size(originalimaget1w);
[filteredlineart1w]=medianfilter(originalimaget1w,9);          %Runs the noise reducing
filtering program medianfilter on the T1 weighted.  This is meant to prepare this image
for transform into a mask.
[mask]=masking(filteredlineart1w);                              %This runs the program
masking that creates a binary mask on the legs.  1's indicate that it is a point inside the
legs, 0's indicate it is a point outside the legs.
mask(206:256,230:256,:)=0;                                      %This removes the red
labels.
mask(231:256,1:25,:)=0;
imageimport=uint8(zeros(x,y,3,z));                              %If this in not turned into a
uint8 the images import binary and black/white
for k=0:(z-1)
   filenamemask = sprintf('%s%d-000.bmp',filename,k*2);   %Must be in same folder as
the m files.
```

```
  imageimport(:,:,:,k+1) = imread(filenamemask);              %Reads in image files and
stacks them into 3D matrix
end
maskimport=zeros(x,y,z);
for k=1:z
   for i=1:x
      for j=1:y
         if imageimport(i,j,1,k)==imageimport(i,j,2,k) &&
imageimport(i,j,1,k)==imageimport(i,j,3,k)                %This makes anything that is
greyscale a value of 0.
            maskimport(i,j,k)=0;
         else
            maskimport(i,j,k)=1;                          %This makes anything of
any color a value of 1.
         end
      end
   end
 maskimport(:,:,k)=rot90(maskimport(:,:,k));
end
maskimport=maskimport.*mask;                              %This removes the right and
left labels from the images.
```

A.9 Reducemask

```
function [newmask]=reducemask(mask,diskradius)
%This program reads in a binary mask image and reduces its size by a value
%specified by the disk radius.
if nargin==1
   diskradius=4;                                    %If a diskradius is not
specified use a value of 4
end
[x,y,z]=size(mask);
SE=strel('disk',diskradius);                        %Creates a structural
element with a disk shape and a radius specified by diskradius
newmask=zeros(x,y,z);
for k=1:z
   newmask(:,:,k)=imerode(mask(:,:,k),SE);          %Reduces the size of a mask
in each slice.
end
```

A.10 Concentration

```
function
[Cpicture,C,Cement]=concentration(maskdrug,imageforbackground,cleaned,cleanedt1w,
T10estimate)
%This program calculates a concentration map and a concentration map picture
%from a segmented mask.  Imageforbackground can be either a T1 map (0) or a
%T1 weighted image(1)
```

```
[x y z]=size(maskdrug);
R=.00381;                                   %The relaxivity for Gd-
DTPA in mmol-1*ms-1
C=zeros(x,y,z);
[T1]=maskdrug.*cleaned;                     %This turns the binary
segmentation to a segmentation that has the T1 values.
[T10]=zeros(x,y,z);
T10=(T10+1)*T10estimate;                    %Creates a matrix entirely of
the value T10estimate.
T10=axials;
Cement=zeros(x,y,z);
for k=1:z
   for j=1:y
      for i=1:x
         if T1(i,j,k)~=0 && T10(i,j,k)~=0    %Uses the equation bellow
when the segmented region does not equal 0
         C(i,j,k) = (1/R)*(1/T1(i,j,k) - 1/T10(i,j,k));    %This equation translates the
T1 values to concentrations.
         elseif T1(i,j,k)==0 && T10(i,j,k)~=0    %Uses the bellow condition
if the segmented region equals 0.
         Cement(i,j,k)=1;
```

```
        elseif T1(i,j,k)~=0 && T10(i,j,k)==0                    %If the segmented region
has a T1 value of 0 the signal is saturated or there is bone cement (something with no
water) present.
            C(i,j,k)=0;
            else
               C(i,j,k)=0;
            end
        end
    end
end
cleanedadj=cleaned./7000;                                       %This adjusts the scale to 1
so that the Cpicture images plot well.
[cleanedadj]=cutoff(cleanedadj,1);                              %This cuts off any value
above 1 (or above 7000 in the T1 map).
cleanedadjt1w=cleanedt1w./1700000;                              %This adjusts the T1
weighted image scale to 1.
cleanedadjt1w=cutoff(cleanedadjt1w,1);
C=cutoff(C,5);                                                  %This cuts off any value
above 5 mM
Cind=zeros(x,y,z);
Cpicture=zeros(x,y,3,z);
if imageforbackground==0                                        %This loop is for making
concentration map pictures with a t1 map as the background
```

```
for k=1:z
   Cind(:,:,k)=gray2ind(C(:,:,k));                    %This makes C and indexed
matrix, instead of a grayscale
   map=colormap(jet);
   Cpicture(:,:,:,k)=ind2rgb(Cind(:,:,k),map);        %This switches C from
indexed to rgb.
   for i=1:x
      for j=1:y
         if Cement(i,j,k)==1
            Cpicture(i,j,:,k)=[0.56 0 0];            %Change this to change color
of cement. If it is [0.56 0 0} cement it will plot red, like the top concentration.
         elseif maskdrug(i,j,k)==0
            Cpicture(i,j,:,k)=cleanedadj(i,j,k);     %If there is no contrast plot
the t1 map.
         end
      end
   end
end
end
if imageforbackground==1                             %This loop is for making
concentration map pictures with a t1 weighted image as the background
for k=1:z
```

```
   Cind(:,:,k)=gray2ind(C(:,:,k));                    %This makes C and indexed
matrix, instead of a grayscale
   map=colormap(jet);
   Cpicture(:,:,:,k)=ind2rgb(Cind(:,:,k),map);        %This switches C from
indexed to rgb.
   for i=1:x
      for j=1:y
         if Cement(i,j,k)==1
            Cpicture(i,j,:,k)=[0.56 0 0];%           %Change this to change
color of cement. If it is [0.56 0 0} cement it will plot red, like the top concentration.
         elseif maskdrug(i,j,k)==0
         Cpicture(i,j,:,k)=cleanedadjt1w(i,j,k);     %If there is no contrast plot
the t1 weighted image.
         end
      end
   end
end
end
```

A.11 Movierabbitconcentration

```
function
[M]=movierabbitconcentration(maskdrug,maskbone,movietype,cleanedt1w,cleaned,Cpict
ure)
```

```
% This function will take a 3d image and make a movie of the view from the
% bottom to the top of the stack.  First you must import maskdrug and
% maskbone for that image set. Movietype is either a T1 map (0) or a
% T1 weighted image(1) as the background.  You can either import a t1 map,
% t1 weighted image, and concentration map picture or you will be prompted
% to import the map and weighted image and a concentration map picture can be
% created.
[x,y,z]=size(maskdrug);
startmovie=1;                                   %To cut down slices enter
other values here.
endmovie=z;


xcut=1:x;                                       %To zoom in on the area of
interest enter other values here.
ycut=1:y;
% % % If running as a program not a function comment out this if loop.
if nargin==3                                    %If you don't include a T1
map and T1 weighted image it will prompt you to enter those here.  Then it will clean
those up and below it will make the concentration map.
originalimage=readdata3d;                       %GUI for importing HDR
(and other) files.  This requires downloading the readdata3d function files from the
matlab website.  First import a T1 map.
```

originalimaget1w=readdata3d; %Then import a T1 weighted image

originalimage=originalimage(:,:,3:5:(end-2)); %This indexes out the extra slices containing standard deviation, etc. and leaves only the actual map slices.

[x y z]=size(originalimage); %Finds the dimensions of the T1 map after removing extra slices.

originalimaget1w=originalimaget1w(:,:,1:z); %The T1 weighted hdr comes as a series of T1 weighted scans with different B values. This takes only the set from the first B value. This should match the dimensions of the T1 map.

[filteredlinear]=medianfilter(originalimage,5); %Runs the noise removing filtering program medianfilter on the T1 map.

[filteredlineart1w]=medianfilter(originalimaget1w,9); %Runs the noise removing filtering program medianfilter on the T1 weighted. This is meant to prepare this image for transform into a mask.

[mask]=masking(filteredlineart1w); %This runs the program masking that creates a binary mask on the legs. 1's indicate that it is a point inside the legs, 0's indicate it is a point outside the legs.

cleaned=double(filteredlinear.*mask); %multiplying the reduced noise T1 map by the binary mask removes all noise outside the legs.

cleanedt1w=double(originalimaget1w.*mask);

end

maskbonep=permute(maskbone,[3 2 1]); %In order for the 3D image to pop up in the correct direction you have to switch axis.

```
maskdrugp=permute(maskdrug,[3 2 1]);
X=0:(x-1);                                  %These are the axis for the
3D image.  They must have the same size as the matrix.
Y=0:(y-1);
Z=0:(z-1);
line=zeros(z,y,x);
k=startmovie:endmovie;
[x1 y1]=size(k);
M=moviein(y1);                              %This creates a matrix of the
correct movie form to put frames in.  To make the movie slower increase this length and
fill multiple slices with the same frame.  Keep in mind that a longer movie is a larger file.
counter=1;
if nargin==5
  [Cpicture,C,Cement]=concentration(maskdrug,movietype,cleaned,originalimaget1w);
%This makes a concentration map if one is not entered
end
for k=startmovie:endmovie
close all
line=zeros(z,y,x);
line(k,ycut,30:240)=1;                      %This is a line (actually a
plane) that moves up the 3D image in the plot to show what slice your on.
h=figure;                                   %This creates a handle for
the figure that is used when you want to retrieve the frame later.
```

```
subplot(2,2,3)                                          %This is a plot of the
concentration map.
imshow(Cpicture(xcut,ycut,:,k),[0 1]);
title('Concentration Map')
subplot(2,2,1)                                          %This is a plot of the 3D
masks
hold on
l=patch(isosurface(Y,Z,X,maskdrugp,.5));
set(l,'FaceColor','blue','EdgeColor','blue');
q = patch(isosurface(Y,Z,X,maskbonep,.3));
set(q,'FaceColor','red','EdgeColor','red');

t = patch(isosurface(Y,Z,X,line,.8));
set(t,'FaceColor','black','EdgeColor','black');
axis([1 250 1 42 1 250])                                %This holds the axis on the
3d image so it doesn't stretch undesirably.  Here the form is [bottom up back]
hold off
title('3-D Drug Mask')
subplot(2,2,2)                                          %This is a plot of the cleaned
T1 map.
imshow(cleaned(xcut,ycut,k),[0 5500])
title('T1 Map')
```

```
subplot(2,2,4)                                  %This is a plot of the cleaned
T1 weighted image
imshow(cleanedt1w(xcut,ycut,k),[0 1700000])
title('T1 Weighted Image')
M(counter)=getframe(h);                         %This grabs the current plot
and makes it a frame in the movie file.  It is important not to open other windows on top
of the plot because this function is screen capturing the plot area and will capture
whatever the top image is in that area.
counter=counter+1;
end
movie2avi(M,'movieconcentration.avi');          %This exports the movie as
an avi to your directory folder
```

APPENDIX B

PROTOCOL FOR IMAGE PROCESSING USING MATLAB AND MIMICS

1. Run the program UnstacktifT1wandT1.m (which runs a median filter, masks, and exports a stack of TIFF files).

2. Run the program T10estimatorwithimport.m to obtain the mean symmetrical histogram value and the standard deviation of the histogram.

3. Sign on to the computer with mimics in Dr. Frakes' lab.

4. Transfer the TIFF images from the directory to the computer with mimics using flash.

5. Open Mimics x64 14.12.

6. Go to File--> "new project wizard" to import pictures into mimics.

7. Use the file browser in import wizard to find your file (mine shows up as Computer-->Removable Disk K:).

8. Highlight the folder that has all your images in it and click next. Open the T_1 map images first.

9. On the "image properties" page, change "Sorting order" to "numeric ascending", change the scan resolution to be the dimensions of one pixel (0.3x0.3x2 mm).

10. On "Edit images" do not change anything just click next.

11. In "check orientation" click the red letters to change the orientation, then click ok. This should take you out of the wizard.

Tips on program: In quadrant 4 when the cursor is a + you can scroll to change the slice you are on. You can also scroll when you select any of the other windows.

12. Create a new mask with a threshold of 0 to T10estimate-standard deviation.

13. Duplicate the first mask.

14. Use the slice editor to delete portion of contrast from the first mask. It is easiest and most reproducible to delete all parts of the mask within the muscle and bone.

15. Use the Boolean operator to subtract the first mask from the duplicate second mask. This should leave just the portions erased.

16. Use the "region grow" function to select all pixels interconnected with the cement from the mask in step 15.

17. Create a 3D object of the mask and export as an STL file. Also export the image slices of the mask as bmp images.

18. Use the "new project wizard" to import the TIFF files of the T_1 weighted image.

19. Create a new mask with a threshold from 0 to 0.

20. Duplicate the mask in 19.

21. Use the slice editor with the livewire function to draw around the outside of the femur or inside of femur.

22. Use Boolean operators to obtain the either the Cortex of the femur or intramedullary canal.

23. Create a new mask with a threshold that includes everything except 0, then use the slice editor to draw or erase sections to obtain a clear outline of the legs.

24. Create 3D objects of the legs and femurs.

25. Import the STL file of the contrast agent.

26. Plot the femurs, legs, and contrast agents in the 3D plot section. Go to file->screenshot to obtain images of the 3D plot.

27. Import the mask file images into MATLAB using the mimicsimportandmapmaker.m program to obtain concentration maps.